Title
Functional Studies of the TMEM16B Calcium-activated Chloride Channel in the Lateral Septum

Permalink
https://escholarship.org/uc/item/9tp5r4tm

Author
Wang, Lynn

Publication Date
2018

Peer reviewed|Thesis/dissertation

**Functional Studies of the TMEM16B Calcium-activated
Chloride Channel in the Lateral Septum**

by

Lynn Wang

DISSERTATION

Submitted in partial satisfaction of the requirements for the degree of
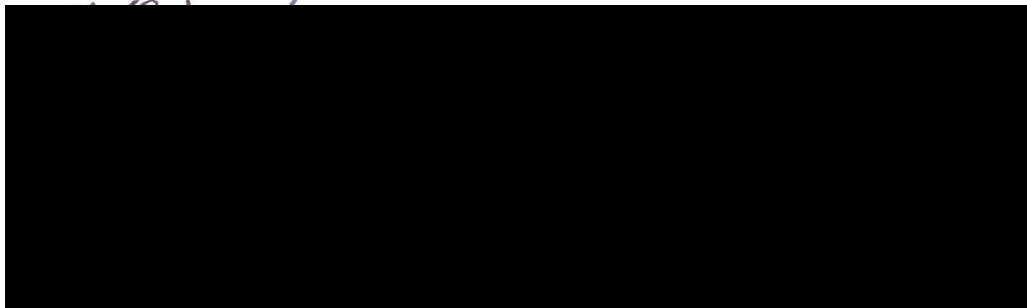
DOCTOR OF PHILOSOPHY

in

Neuroscience

in the

GRADUATE DIVISION

of the

UNIVERSITY OF CALIFORNIA, SAN FRANCISCO

Approved:

Committee in Charge

DEDICATION AND ACKNOWLEDGEMENTS

First and foremost, I am incredibly grateful to my thesis advisor, Dr. Lily Jan, and Dr. Yuh Nung Jan for their support during my graduate school years. They have provided me with a rich, learning environment to become an independent thinker and scientist. While I found it overwhelming at first, it ultimately proved to be invaluable for my own intellect and self-confidence. Lily has always treated me with patience, warmth, and kindness. I've appreciated the fact that Lily always makes herself available to speak when she is in her office, enabling me to stop by without advanced notice. Her encouragement to pursue my career goals has been reassuring as a graduate student.

I would like to acknowledge the members of my thesis committee, including my chair, Dr. Alexandra Nelson, Dr. Robert Edwards, and Dr. Vikaas Sohal. They have always provided valuable feedback about my thesis project, and have also been supportive of my career endeavors.

I would like to recognize many of the postdoctoral fellows in the Jan lab, who have not only treated me as an equal, but taken the time to mentor me as well. First, I would like to thank Dr. Christian J. Peters, my postdoctoral mentor in the Jan lab, for his fantastic mentorship and guidance. Chris was always more than willing to sit down with me to talk through project ideas and troubleshoot experiments, despite his busy schedule. Becoming adept at patch clamp physiology requires climbing a huge learning curve; Chris was always there to offer his expertise when things went awry. His friendliness and gregarious personality made for a positive experience in the lab. Dr. Chin Fen Teo has been like a big sister to me: showing me the ropes of many research techniques, giving me scientific and career advice, possessing encyclopedia-level knowledge of where everything in the lab is located, taking me to Paint Nite events, discussing

the various bike routes in San Francisco, and being such a great friend to confide in. I would also like to thank Dr. Tina Han for her friendship and guidance throughout the years. Tina is very personable and I always found her very approachable, whether it was to discuss the big picture implications of my thesis project or our latest knitting projects. Finally, I would like to acknowledge Dr. Shi-Bing Yang for teaching me how to patch during my rotation in the lab and Dr. Tongfei (Alex) Wang for sharing his electrophysiology expertise with me.

I am grateful to my fellow Jan lab graduate school buddies, Mario Zubia, Hung Lin, and Laura Devault, with whom I have shared the unique experience of receiving our PhD training in the Jan lab. Mario and I joined the lab roughly around the same time. Graduate school is challenging, and it meant a lot to have an equal I could commiserate with about failed experiments and cannibalized mouse pups. Thanks to Mario's marvelous baking skills, I was introduced to the French macaron and gifted with a regular supply of baked goods during my time in the lab. With Hung, I am fortunate to have been her roommate, lab mate, and friend in graduate school. Hung is a very dedicated friend who has always been there for me, and I am immensely grateful to have her in my life. Laura was so welcoming when I first joined the lab. I've enjoyed getting to know her throughout the years with our shared interests in baking, cooking, and all things Ottolenghi-related.

My work in the Jan lab would not have been possible without the fantastic administrative staff, including Sandra Barbel, Monika Avdeef, Marena Tynan-La Fontaine, Eirish Sison. To Sandy, our lab manager, many of my experiments could not have been possible without her help. To Monika, whose impeccable organizational skills were invaluable to everyday lab function. To Marena, who helped me with all of my stereotaxic surgeries. I would not have been able to collect any of that data without her help. To Eirish, who helped me genotype all my mice during

her tenure in the lab, and was a wonderful friend in the lab. I would also like to thank the LARC technician who has taken care of my mice during graduate school, Kevin Rebadulla. I enjoyed getting to know Kevin throughout the years and appreciated his thorough attention to caring for my mice.

I am fortunate to have formed a close community of friends since moving to SF. To my fellow neuroscience classmates, Faten Sayed, John King, Yelena Kulik, Jermyn See, Ling Guo, I am grateful for your friendship throughout the years. To my musician friends, Lay Kodama, Will Berdanier, Nicole Romano, Bianca Lee, Jennifer Chang, and Albert Wu, I cherish all the fun times we had during our chamber music jam sessions and epic outdoor adventures. To my Bay Area Music Circle Meetup friends: Lily Hsu-Storaker, David Anderson, Nina Labrador, Brian Tang, and Kevin Liu, you all gave me the sense of community I earnestly sought when I first moved to SF, and I have had many fun times playing music at the potluck gatherings while appreciating your enthusiasm for obscure classical music composers. To Brooke Babineau and Aditi Narayan, I'm grateful for our years of friendship and our mutual love of all things related to the Food Lab.

I am grateful for my friends from my pre-SF days, despite being spread all across the country. To my high school friends Amy Riggins and Nicole Wanlass, may the Friendship Club live on forever. To my CBS buddies, Eddie Stronge, Carley Karsten, George Chao, Aparna Ramen, Donna Coetzee, and Tarini Goyal, it's been amazing to see where we've all ended up since our college days. To Rheanne and David Maravelas, Emilie Sieker, and Tobias Gulden, thank you for some truly unforgettable camping adventures through the Yellowstone wilderness. To Ysa and Ara Tan, words can't express how great it is to have you two as cousins.

life and his ability to go all-in for his passions are uplifting and contagious. His self-confidence has changed the way I approach conflict and resolution in my professional life, realizing that my actions don't have to be defined by the stereotypes set for my gender or race. I'm eternally grateful for Eitan's support and all the love I have received from his large, extended family. Eitan often joked that our first child would be "my PhD"; I'm happy to say that after five years and three months, this is finally coming to fruition.

FUNCTIONAL STUDIES OF THE TMEM16B CALCIUM-ACTIVATED CHLORIDE CHANNEL IN THE LATERAL SEPTUM

By Lynn Wang

ABSTRACT

The lateral septum (LS) plays an important role in regulating aggression. It is well recognized that LS lesions lead to a dramatic increase in aggressive behaviors. A better understanding of LS neurophysiology and its functional output is therefore important to assess LS involvement in regulating aggression. The LS is a heterogeneous structure that maintains inputs and outputs with multiple brain regions, and is also divided into subregions that innervate one another. Thus, it is challenging to identify the exact cell type and projections for characterization. In this study, we determined the expression pattern of the Calcium-activated Chloride Channel (CaCC), TMEM16B, in the LS of both male and female mice. We then investigated the physiological contribution of CaCC to LS neuronal signaling. By performing whole cell patch clamp recording, we showed that TMEM16B regulates spike frequency and spike frequency adaptation in subpopulations of LS neurons. We further demonstrated that loss of TMEM16B function leads to lengthened displays of aggressive behaviors by male mice during the resident intruder paradigm. In conclusion, our findings suggest that TMEM16B function contributes to neuronal excitability in subpopulations of LS neurons and the regulation of aggression in male mice.

TABLE OF CONTENTS

LIST OF FIGURES

LIST OF TABLES

CHAPTER 1: INTRODUCTION

Ion channels are pore-forming structures that reside in the cell membrane, and play a fundamental role in regulating physiological functions in the nervous system (Hille, 2001). Ion channels are selectively permeable to specific cations or anions, and are categorized based on their modes of activation and preferred conducted ionic species. Voltage-gated ion channels are activated by changes in membrane potential (Jan and Jan, 1989). Mechanosensitive channels are activated by force and are found in epithelial tissue, auditory cells, and muscle spindle fibers (Sackin, 1995). Ligand-gated channels or ionotropic receptors, such as AMPA receptors, open in response to the binding of specific ligands, such as neurotransmitters and odorant molecules. In the following chapters, I will delineate my thesis work understanding a specific ion channel, the calcium-activated chloride channel TMEM16B, and its function in the mouse lateral septum.

The Calcium-activated chloride channel, TMEM16B

Molecular identification of the calcium-activated chloride channel

For decades, calcium-activated chloride currents were known to be important for a variety of physiological functions, including photoreceptor transduction, smooth muscle contraction, and airway epithelial fluid secretion (Hartzell et al., 2005). However, the molecular identity of the responsible channel remained elusive until recently. During the search for CaCC, Bestrophins and Chloride channel accessory proteins (CLCA) were also considered candidates, but both were eventually ruled out based on lack thereof and contradicting physiological evidence (Huang et al., 2012a). Finally, three independent research groups identified the calcium-activated chloride channel (CaCC) responsible for this current to be TransMEMbrane

1

protein of unknown function 16A (TMEM16A), also known as Anoctamin 1 (gene name: *Ano1*) (Caputo et al., 2008; Schroeder et al., 2008; Yang et al., 2008). Members of the Jan laboratory confirmed TMEM16A to be the molecular identity of CaCC using the axolotl oocyte as a heterologous expression system for CaCC from *Xenopus* oocytes (Schroeder et al., 2008), which are well known for their endogenous expression of CaCC for polyspermia prevention (Barish, 1983). They also identified the closely related TransMEMbrane protein of unknown function 16B (TMEM16B) as a CaCC by expressing mouse TMEM16B in Axolotl oocytes and HEK293 cells to test its functionality. Following this major breakthrough, the study of TMEM16A and TMEM16B function progressed significantly to investigate their biophysical properties (Cenedese et al., 2012; Betto et al., 2014; Tien et al., 2014; Peters et al., 2015, 2018), the electron cryo-microscopy (cryo-EM) structures of TMEM16A (Dang et al., 2017; Paulino et al., 2017), and CaCC function in multiple tissue types and organ systems.

The TMEM16 protein family

The identification of TMEM16A and TMEM16B as CaCCs also led to the characterization of other TMEM16 protein family members. This ten member protein family (TMEM16A-K, excluding I) encompasses a wide range of physiological functions, including phospholipid scrambling and ion transport (Pedemonte and Galietta, 2014). TMEM16A and TMEM16B, along with the *Drosophila* homologue, Subdued (Wong et al., 2013), are the only known CaCCs thus far in the family. TMEM16E, TMEM16F, and the fungal homologues nhTMEM16 (Lee et al., 2016) and afTMEM16 (Malvezzi et al., 2013) function as dual channels and scramblases (Falzone et al., 2018). TMEM16F specifically is a phospholipid scramblase important for blood coagulation (Suzuki et al., 2010; Yang et al., 2012; Fujii et al., 2015;

2

Watanabe et al., 2018). TMEM16F is also expressed in microglia and involved in regulating neuropathic pain (Batti et al., 2016). TMEM16C, TMEM16D, TMEM16J, and TMEM16G are associated with scramblase activity, but whether these proteins also possess channel functionality remains an open question (Suzuki et al., 2013). TMEM16C, in particular, has been shown to interact with the sodium-activated potassium channel, Slack, in regulating pain processing in rat dorsal root ganglion neurons (Huang et al., 2013). Finally, the functionality of TMEM16K and its *Drosophila* homologue, AXS, remain uncharacterized, but deletion of TMEM16K is associated with autosomal recessive cerebellar ataxia (Chamova et al., 2012) while AXS is known to be localized to the endoplasmic reticulum (Kramer and Hawley, 2003).

Biophysical properties of TMEM16B

Following the molecular identification for CaCCs, subsequent studies demonstrate that recordings of HEK293 cells with heterologous expression of TMEM16B show calcium-activated chloride currents (Schroeder et al., 2008; Pifferi et al., 2009; Stephan et al., 2009; Stöhr et al., 2009). By elevating the intracellular calcium concentration and excluding the involvement of calmodulin, these groups show that TMEM16B is directly gated by calcium to mediate chloride conductance (Pifferi et al., 2009). TMEM16B is characterized by rundown of current after repeated stimulation, which is similar to the rundown seen in native olfactory CaCC (Stephan et al., 2009). The reversal potential of TMEM16B corresponds to the chloride equilibrium potential as expected for a chloride channel. Overall, these findings suggest that TMEM16B is characteristic of a calcium-activated chloride channel.

Investigation of TMEM16B gating and permeation reveal the following permeability ratio sequence for the channel: $SCN^- > I^- > NO_3^- > Br^- > Cl^- > F^- > gluconate$ (Betto et al., 2014). These

experiments demonstrate that anions that are more permeable reduce the rate of channel activation and deactivation to a greater extent, and increase the calcium sensitivity to a greater extent as well. In a separate study, site-directed mutagenesis of TMEM16B shows that the following residues located in the first intracellular loop, glutamates E367 and $_{386}$EEEEE$_{390}$, regulate voltage dependency in TMEM16B (Cenedese et al., 2012).

Compared to TMEM16A, TMEM16B has a calcium sensitivity that is ten-fold lower at +60 mV and two-fold lower at -60mV (Yang et al., 2008; Pifferi et al., 2009). These findings suggest that TMEM16A and TMEM16B each possess unique gating properties downstream of calcium binding.

Structure of calcium-activated chloride channels

Although high-resolution structural data for TMEM16B does not yet exist, structures for related family members have been reported. The X-ray structure of the TMEM16 fungal species family member, *Nectria haematococca* (nhTMEM16), was the first structure paper to reveal the conserved calcium binding sites necessary for lipid scrambling (Brunner et al., 2014). While nhTMEM16 functions as a calcium-activated lipid scramblase, the residues that take part in calcium coordination correspond to those residues involved in TMEM16A binding to calcium ions (Tien et al., 2014). The cryo-EM structure for mammalian TMEM16A has been identified by two independent groups (Dang et al., 2017; Paulino et al., 2017). TMEM16A is made up of two subunits that form a dimer, and each subunit of the dimer functions independently from each other (Jeng et al., 2016; Lim et al., 2016);. Each subunit is made up of ten transmembrane domains. Each subunit has two calcium binding sites formed by five acidic residues and one asparagine (Dang et al., 2017). Based on a comparison of mouse protein sequences from UCSC

Genome Browser, TMEM16B shares ~56% sequence identify with TMEM16A. Thus, it is likely that the structure of TMEM16B is quite similar to that of TMEM16A.

Calcium-activated chloride channel function in the central nervous system

Both TMEM16A and TMEM16B are expressed in multiple brain regions in the central nervous system (CNS). TMEM16A expression and function has been reported in the trigeminal ganglion (Kanazawa and Matsumoto, 2014), brain stem (Cho et al., 2014), retina (Jeon et al., 2013), vomeronasal organ (Dibattista et al., 2012; Münch et al., 2018a), and cerebellar cortex (Zhang et al., 2015). TMEM16B function has been identified in the hippocampus (Huang et al., 2012b), inferior olive (Zhang et al., 2017) , thalamus (Ha et al., 2016), retina (Stöhr et al., 2009), olfactory bulb (Billig et al., 2011; Pietra et al., 2016), vomeronasal organ (Münch et al., 2018b), and cerebellar cortex (Zhang et al., 2015). Since neurons require calcium influx for neuronal excitability and synaptic transmission, CaCC could assist in maintaining the membrane potential below threshold to prevent neurons from becoming hyperexcitable, or in returning the membrane to rest following periods of activity. In addition, CaCC function would help amplify signaling in neurons with a high internal chloride concentration, as in the case of odorant neuronal cilia. In the following section, we will describe the function of TMEM16B in specific brain regions.

Calcium activated chloride channels in photoreceptor cells

Photoreceptor cells reside in the retina and are essential for visual transduction and our perception of the visual world. When depolarized, these cell types depend on Ca^{2+} influx from L-type calcium channels to maintain a constant release of glutamate (Nachman-Clewner et al., 1972). Calcium-activated chloride currents were first identified in the salamander retina to be

important for regulating the calcium concentration present in the photoreceptor synaptic terminal, also called the photoreceptor ribbon synapse (Bader et al., 1982). Subsequent studies also reported the presence of a calcium-activated chloride current at the ribbon synapse (Maricq and Korenbrot, 1988; Thoreson et al., 2003; Cia et al., 2005). Soon after the advent of the molecular identification of CaCC, TMEM16B was identified to be the channel responsible for the endogenous calcium-activated chloride current at the ribbon synapse for negative feedback regulation (Stöhr et al., 2009). TMEM16B colocalizes specifically with adaptor proteins PSD95, VELI3, and MPP4 to form the presynaptic protein complex responsible for maintaining Ca^{2+} homeostasis at the ribbon synapse. TMEM16B has a C-terminal PDZ binding motif that interacts with the PDZ domain of PSD95, for its anchoring at the ribbon synapse.

TMEM16B function in mouse olfaction

The presence of calcium-activated chloride current in olfactory sensory neurons (OSN) was well established before the functional identification of TMEM16B as the CaCC (Kleene and Gesteland, 1991; Firestein, 2001). During odorant sensory transduction, odorant molecules bind to olfactory receptors in OSNs, triggering a GPCR signaling cascade leading to activation of cyclic nucleotide-gated channels. These channels allow calcium influx, which causes TMEM16B activation and chloride efflux (Kleene, 1993; Reisert et al., 2003). Unlike most neurons, OSNs contain a high concentration of intracellular chloride, thus chloride would leave the cell following CaCC activation. This chloride efflux promotes olfactory signal amplification and subsequent olfactory sensation.

TMEM16B was first identified as the responsible CaCC in OSNs using proteomic screens of the olfactory epithelium (Stephan et al., 2009; Rasche et al., 2010).

6

Immunohistochemistry analysis shows TMEM16B expression in the cilia membrane of OSNs. Furthermore, patch clamp recordings of HEK293 cells expressing TMEM16B show a chloride conductance following calcium activation (Stephan et al., 2009; Stöhr et al., 2009).

Subsequent studies investigating the behavioral implications of TMEM16B function have yielded conflicting results. One group detects TMEM16B function at the neuronal level, but claims that TMEM16B is dispensable for olfaction in mice (Billig et al., 2011). Using a TMEM16B KO mouse line they generated, they show loss of TMEM16B expression in the olfactory epithelium and loss of calcium-activated chloride currents in OSNs. However, TMEM16B KO mice display no deficits in discrimination tasks for different scents, prompting the conclusion that TMEM16B is not essential for olfaction.

In a recent study, another group examines the same mutant mice while using a different olfaction behavioral paradigm, to demonstrate that TMEM16B contributes to the sense of smell (Pietra et al., 2016). During an odor-guided food-seeking task, mice are required to locate an Oreo cookie hidden in the bedding of a mouse cage. The task is repeated once a day across five days and the latency for locating the cookie is measured each day. Mice are returned to a normal chow diet for a week, and then exposed to a multitude of odors that included known odors and unknown odors. During this assay, TMEM16B KO mice show longer latency for locating the cookie during Days 1 and 3 of the first part of the task compared to WT littermates. When exposed to the variety of different odors, TMEM16B KO mice take significantly longer time than WT littermates to locate odors they were unfamiliar with (peanuts and cheese) but not odors they were familiar with (chow and cookies). In addition, patch clamp recordings demonstrate that OSNs with current injections show increased spike firing in TMEM16B KO neurons compared to WT neurons.

In summary, the present literature on TMEM16B function in OSNs suggests that the channel contributes to both the firing activity of OSNs and olfactory sensation in mice. While the two research groups present contradictory results regarding TMEM16B function in olfaction (Billig et al., 2011; Pietra et al., 2016), the chosen behavioral task conducted may have affected the outcome. Whereas Billig and colleagues chose an operant conditioning test that tested the ability to differentiate between monomolecular odors, Pietra and colleagues chose a task that simultaneously exposed mice to multiple odors, thereby activating a larger glomerular response (Vincis et al., 2012), and tested for the odor sensitivity without requiring repeated exposures. Thus it is possible that the ability of TMEM16 KO mice to learn and master ready detection of familiar odors may have obscured their sensory deficiency when they are tested with discrimination paradigms that involve repeated exposures during training.

TMEM16B function in the vomeronasal organ

The vomeronasal organ (VNO) makes up the accessory olfactory system, and primarily responds to pheromones and some odorant molecules (Chamero et al., 2012). Although the human VNO is considered a vestigial structure, the rodent VNO plays a critical role in innate behaviors. Mice exposed to pheromones from the same species or scents from predators respond by engaging in sexual behavior, aggression, or flight, respectively. The VNO is made up of vomeronasal sensory neurons (VSNs), characterized as bipolar neurons in the sensory epithelium of the VNO. Following activation by pheromones or odorants, VSNs become depolarized and generate action potentials that propagate along their axons that innervate the olfactory bulb. In VSNs, the chloride co-transporter, sodium-potassium-chloride-cotransporter 1 (NKCC1) contributes to their high intracellular chloride concentration (Yang and Delay, 2010). Typically,

immature central neurons undergo a transition from high to low intracellular chloride concentration during development following the onset of K^+-Cl^- cotransporter (KCC2) expression, which mediates the transport of chloride extracellularly (Luhmann and Prince, 1991; Zhang et al., 1991; Rivera et al., 2005). A small population of mature neurons, including VSNs, OSNs, and medial habenular neurons (Kim and Chung, 2007), does not express KCC2, thereby maintaining the high intracellular chloride concentration and distinguishing them from most central neurons in this respect.

TMEM16B expression has been reported in VSNs (Yang and Delay, 2010; Billig et al., 2011; Münch et al., 2018b). In addition, inside out patch recordings of VSN dendritic tips detect CaCC activity (Yang and Delay, 2010). TMEM16B appears to play only a minor role in regulating VSN spike firing (Münch et al., 2018b). In fact, TMEM16A is also expressed in VSNs and deletion of TMEM16A has a more significant effect on VSN spike firing (Amjad et al., 2015; Münch et al., 2018a). Moreover,TMEM16A/TMEM16B double knockout mice do not display deficits in aggressive behaviors compared to control littermates. These results seem to suggest that while CaCC may contribute to VSN excitability, there is modest CaCC contribution to VSN relevant behaviors, such as aggression. It remains to be determined as to the extent of CaCC contribution to other VSN associated behaviors.

TMEM16B function in hippocampal neurons

The hippocampus is an essential component of learning and memory (Jarrard, 1993). Extensive research has been conducted on hippocampal neurophysiology to better understand its molecular machinery. The distinct morphology and organization of hippocampal pyramidal neurons has also provided neurophysiologists with an accessible system for understanding

central neuron physiology. In rat hippocampal neurons, calcium-activated potassium channels are well known to be involved in regulating neuronal signaling through multiple means. Big-conductance calcium-activated potassium channels (BK) regulate action potential waveform following influx from voltage-gated calcium channels (Lancaster, B., Nicoll, 1987; Storm, 1987a, 1987b) and neurotransmitter release at the axon terminal (Hu et al., 2001). Small-conductance calcium-activated potassium channels (SK) regulate synaptic plasticity at the post-synaptic side due to their activation by NMDAR-mediated calcium influx (Stackman et al., 2002; Ngo-Anh et al., 2005).

More recently, TMEM16B has also been identified as a novel contributor to the regulation of hippocampal neuronal signaling (Huang et al., 2012b). As a CaCC, TMEM16B has been shown to modulate action potential halfwidth in CA1 and CA3 neurons. However, evidence so far suggests that TMEM16B is not involved in regulation of neurotransmitter release at the axon terminal of the Schaffer collateral (CA3-CA1 synapse). TMEM16B also resides in the calcium nanodomain with close proximity of NMDA receptors in the dendritic region of CA1 neurons, where the CaCC regulates EPSP amplitude, EPSP temporal summation, and EPSP spike coupling (Huang et al., 2012b). Given the functional similarities seen between TMEM16B and BK/SK channels, it will be of interest to determine whether TMEM16B also contributes to the regulation of long-term synaptic plasticity in the hippocampus.

TMEM16B function in thalamocortical neurons

The thalamus is comprised of multiple nuclei that make up the major sensory relay center of the brain. This brain region relays input from subcortical structures to various neocortical areas responsible for sensory information processing. Since the thalamus passes on this information via thalamocortical projections that innervate the cortex, the firing properties of thalamocortical neurons have been of great interest in research endeavors to better understand sensory processing in the brain (McCormick and von Krosigk, 1992; Le Masson et al., 2002). Thalamocortical neurons regulate their firing patterns via spike frequency adaptation (Landisman and Connors, 2007). TMEM16B expression in thalamocortical neurons is involved in regulating spike frequency adaptation and medium afterhyperpolarization (mAHP) currents (Ha et al., 2016). TMEM16B activation occurs due to calcium influx from T-type calcium channels expressed in thalamocortical neurons. Furthermore, shRNA knockdown of TMEM16B in thalamocortical neurons leads to an increase in spike number, decrease in spike frequency adaptation, and decrease in the length of mAHP currents. TMEM16B knockdown in the thalamus results in enhanced visceral pain response in mice, suggesting that reducing TMEM16B function in thalamocortical neurons could result in behavioral deficits.

TMEM16B regulation of inferior olivary neuronal function

The inferior olivary nucleus (IO) is situated in the medulla oblongata and plays an essential role in motor coordination and learning (Schweighofer et al., 2013). IO neurons innervate Purkinje cells in the cerebellar cortex via climbing fibers. Dendritic voltage-gated calcium channels contribute to the firing characteristics of IO neurons, and these channels are in turn regulated by SK channels (Llinás and Yarom, 1981a, 1981b). Dendritic voltage-gated

calcium channels contribute to the afterdepolarization (ADP) seen during IO neuron action potential firing while SK channels contribute to the mAHP that follows during repolarization.

Recently, calcium-activated chloride currents were identified in IO neurons to be an additional contributor to neuronal repolarization (Zhang et al., 2017). Using a TMEM16B KO mouse model, where a farnesylated mCherry protein followed by a stop codon replaced exon 3 of the *TMEM16B* gene, IO neurons show high expression of TMEM16B, but not TMEM16A. TMEM16B KO IO neurons display loss of the calcium-activated chloride tail current. In terms of their spike firing properties, TMEM16B KO IO neurons display longer ADPs and AHPs compared to WT IO neurons. This loss of regulation in the dendritic region carries over to the ability of KO IO neurons to fire action potentials; KO IO neurons show reduced frequency of spike firing, suggesting that KO IO neurons spend more time in an excitable state and reach a repolarized state less frequently. In addition, TMEM16B KO mice demonstrate deficits in cerebellar motor learning (Zhang et al., 2017), suggesting that TMEM16B function in IO neurons has behavioral relevance as well.

TMEM16B cerebellar cortex function

CaCCs have also been identified in Purkinje cells in the cerebellar cortex (Satoh et al., 2013; Zhang et al., 2015). TMEM16A is expressed in the cell body of Purkinje cells and inhibitory interneurons of the cerebellar cortex while TMEM16B is expressed in the dendritic field of Purkinje cells (Zhang et al., 2015). The authors demonstrate that functionally, TMEM16B regulates the number of inhibitory postsynaptic currents (IPSCs) in Purkinje cells. TMEM16B KO Purkinje cells display no differences in IPSC frequency before and after climbing fibers are activated, while TMEM16B WT Purkinje cells show a significant decrease in

IPSC frequency after climbing fiber activation. It remains to be determined as to whether loss of TMEM16B function in the cerebellar cortex may also contribute to cerebellar motor learning, as seen in the study investigating TMEM16B function in IO neurons (Zhang et al., 2017).

TMEM16B relevance in human disease

TMEM16B has been reported to be involved in various types of human disease, including von Willibrand's disease (VWD), an autosomal recessive disease involving the mutation of the von Willibrand factor (VWF) gene, a protein important for blood coagulation. In 2007, a study found that patients with severe Type 3 von Willibrand's disease (VWD) possessed a large 253 kb deletion of the VWF gene and part of the TMEM16B gene, both of which are located on the same locus of chromosome 12 (Schneppenheim et al., 2007). This sort of deletion has only been identified in Italian and German families. This study did not look into how TMEM16B function is affected by this deletion of VWF because this was before the identification of TMEM16A and B as CaCCs. However, a subsequent report in 2015 detailed the investigation of an Italian family of eight members, four of whom possessed the homozygous 253 kb deletion (Cenedese et al., 2015). These four family members showed significant decrease in olfactory function compared to control unrelated Italian people of similar sex, age, and education as these family members. However, the other four members of the family, 3 of whom were heterozygous for the 253 kb deletion and 1 who had the wile type gene, did not show significant differences in olfactory function compared to their homozygous family members. The authors speculate that other factors, such as social cultural differences, could have contributed to this family's decrease in olfactory function. In addition, they suggest that loss of TMEM16B function in these family members could have led to channel compensation as well. Since no other studies have been

published regarding this disease relevance, it remains to be seen whether these findings with a small sample size can be reproduced.

In a genome-wide association study that sampled a population of 200 Japanese patients with panic disorders and 200 control patients, TMEM16B was identified as the location of a single nucleotide polymorphism (SNP) significantly associated with panic disorders (Otowa et al., 2009). Patients with panic disorders experience panic attacks and anxiety over the thought of having future panic attacks. This finding provides intriguing implications into the role of TMEM16B in regulating anxiety-related behaviors. Given that TMEM16B is expressed in areas of the brain implicated in anxiety-like behaviors, understanding how TMEM16B contributes to this behavioral output may shed light for future panic disorder treatments. Currently, no studies have been published thus far investigating the role of TMEM16B in anxiety-related behaviors.

Finally, perhaps most intriguing is the identification of TMEM16B as an autoimmune target of multiple sclerosis (MS) (Ayoglu et al., 2016). In this study, plasma samples from over 2000 MS patients and controls were screened and compared for autoantigens that elicit autoantibody responses. Immunohistochemistry conducted on human brain tissue samples show increased fluorescent intensity of TMEM16B in samples with MS lesions compared to control samples and TMEM16B protein aggregates were observed as well. MS is an autoimmune disease that causes inflammation of the CNS and subsequent damage and destruction of myelin sheaths. In 2012, the disease affected about 150 in every 100,000 people in the United States alone (Dilokthornsakul et al., 2016). There is currently no cure for MS, though treatments do exist to mitigate symptoms. Thus, identifying the autoimmune targets of MS could help us better understand the mechanisms underlying disease pathology for treatment development.

The Lateral Septum

The lateral septum (LS) is well established to be heavily involved in emotional and mood-related behaviors, including aggression, stress, fear and anxiety, maternal care, and reward (Sheehan et al., 2004). Classical studies investigating LS relevance in behavior demonstrate that LS lesions lead to exaggerated displays of aggressive and defensive behaviors (Spiegel et al., 1940; Brady and Nauta, 1953; Albert and Chew, 1980). However, the heterogeneity of the LS, both in terms of its connectivity (Risold and Swanson, 1997a) and expression of neurotransmitters and neuropeptides (Risold and Swanson, 1997b), have made it challenging to understand the neural circuitry underlying LS-associated behaviors. In this section, we will discuss what is known from the literature concerning LS anatomy, LS function, and its roles in associated behaviors.

Lateral septum connectivity

The LS is located along the midline of the brain, medial to the lateral ventricles, anterior to the hippocampus, posterior to the prefrontal cortex, ventral to the neocortex, and dorsal to the medial septum. The LS maintains connections with many brain regions associated with the limbic system (Figure 1.1). The LS receives major input from the hippocampus, organized topographically in the dorsal to ventral direction (Risold and Swanson, 1997a). The LS maintains reciprocal connections with the hypothalamus, and LS innervation of the hypothalamus also follows a topographical organization.

The LS is divided into three subregions, the caudal LS (LSc), rostral LS (LSr), and ventral LS (LSv) (Risold and Swanson, 1997a). Each subregion has unique inputs and outputs with other brain regions (Sheehan et al., 2004).The LSc receives major input from the CA3

region of the hippocampus and synapses on the medial septum and nucleus of diagonal band (NDB), and these neurons then project back to the hippocampus. Medial septum complex innervation of the hippocampus is important for generating hippocampal theta rhythms (Stewart and Fox, 1990; Vertes, 2005; Bender et al., 2015). LS innervation of the medial septum complex regulates the generation of theta rhythm oscillations (Stewart and Fox, 1990; Gallagher et al., 1995; Chee et al., 2015). The LSc also maintains reciprocal connections with the lateral hypothalamic area (LHA) and the supramammillary nucleus (Risold and Swanson, 1997a), which are involved in aggression (Woodworth, 1971) and arousal (Pedersen et al., 2017).

The LSv receives major input from the subiculum and entorhinal cortex and projects to anteroventral periventricular nucleus, the medial part of the MPO, the ventral premammilary nucleus, and the dorsomedial nucleus (Risold and Swanson, 1997a). These hypothalamic nuclei are all interconnected and part of the sexual dimorphic circuit involved in mediating sexual and parental behaviors (Simerly and Swanson, 1986; Canteras et al., 1994; Simerly, 2002).

The LSr receives major input from the CA1 region and the subiculum and projects to hypothalamic regions including the LHA, lateral preoptic area (LPO), anterior hypothalamus (AHN), and periaqueductal gray (Risold and Swanson, 1997a). These areas are implicated in locomotion and defensive behaviors (Sinnamon, 1992). Of these output regions, the LSr displays the densest projections in the LPO. The ventral part of the LSr also projects to similar regions as the LSv, including the lateral part of the medial preoptic area (MPO), the ventral premammilary nucleus, and the tuberal nucleus. The connections suggest that multiple subregions of the LS are implicated in sexual and parental behaviors.

Finally, LS neurons also innervate each other to form intraseptal connections (Staiger and Nurnberger, 1991; Risold and Swanson, 1997a). Related findings indicate that neurons within

each LS subregion are interconnected. Moreover, interseptal connections also exist. For example, anatomical tracing studies indicate that LSc neurons innervate LSr neurons (Risold and Swanson, 1997a). However, much remains to be learned about the details regarding the LS microcircuits and how these connections affect overall LS function.

Cellular morphology and heterogeneity of the lateral septum

Based on Golgi/electron microscopy (EM) analysis, LS neurons can be characterized based on their LS subregion localization and dendritic morphologies (Alonso and Frotscher, 1989). LSc neurons are grouped into two types. Type I LSc neurons have short, thick dendrites extending from a round or oval-shaped soma. These neurons have a dense covering of thick spines found all along their dendrites. Type II LSc neurons have long, thin dendrites that protrude from an oval- or triangular-shaped soma. Type II dendrites are generally covered with fewer spines compared to Type I dendrites. LSr neurons are also grouped into Types I and II. Type I LSr neurons have a medium-sized soma with a bi-tufted dendritic field while Type II LSr neurons have morphologies similar to those of Type II LSc neurons. All LSr neurons are characterized by dendrites with a sparse spine density. Finally, LSv neurons are primarily smaller in size with shorter dendrites compared to LSc and LSr neurons.

The LS is mostly composed of GABAergic projection neurons (Risold and Swanson, 1996; Zhao et al., 2013). However, a characterization of LS chemoarchitecture suggests that the LS includes multiple subpopulations of neurons that express different types of neurotransmitters, neuropeptides, and steroid hormone receptors (Risold and Swanson, 1997b). Neurons in the LSc subregion are characterized by expression of somatostatin and mineralocorticoid receptors. Subsets of LSc neurons also express Substance P, the androgen receptor, vasopressin, dopamine,

and dynorphin. Neurons in the LSv are best identified by mRNA expression of the estrogen receptor. Finally, the LSr subregion contains the most diverse expression pattern of markers. Most LSr neurons express the neuropeptides enkephalin and neurotensin. Subsets of these neurons also express catecholamines, dopamine, noradrenaline/adrenaline, and calcitonin gene-related peptide (CGRP).

The roles of some of these LS neuronal populations have been studied to understand how they contribute to LS function. Vasopressin has been identified as a facilitator of excitatory synaptic transmission and long-term potentiation (van den Hooff et al., 1989; Excitatory and Septum, 1990; Allaman-Exertier et al., 2007). Vasopressin injection into the LS also promotes intermale aggression revealed with the resident intruder paradigm (Veenema et al., 2010). Activation of the vasopressin receptor, AVPR1b, at CA2 presynaptic terminals at the CA2-LS synapse promotes social aggression (Leroy et al., 2018). In addition, LSr neurons expressing type 2 corticotropin-releasing factor receptor (Crfr2), function to regulate anxious behaviors (Anthony et al., 2014). Activation of LS Crfr2+ neurons promotes stress-induced behaviors, while inhibition of LS Crfr2+ neurons dampens these behaviors. Finally, injection of Substance P into the rat lateral septum induced stressful responses during elevated plus maze testing (Gavioli et al., 1999).

The characterization of LS neurons in terms of their morphology and protein expression patterns demonstrates the breadth of cellular heterogeneity found in the LS. These findings can be used to better understand how specific subpopulations of LS neurons contribute to overall LS neuronal function and relevant behaviors.

The lateral septum and its role in aggression

An early exploratory study investigating brain function in cats discovered that broad lesions of the LS and adjacent brain regions leads to an exaggerated response in aggressive and defensive behaviors (Spiegel, Miller, and Oppenheimer 1940). Similar results are seen in rats when lesions were performed to the septal region, including the lateral and medial septum (Brady and Nauta, 1953, 1955). Increases in "emotional reactivity" and "startle responses" were observed in rats following the surgery, especially when researchers were attempting to handle the rats. Lesions of the cingulate cortex served as control experiments, demonstrating the specificity of the septal region in regulating the "septal rage" phenotype.

Subsequent studies demonstrate that inhibiting the LS with an intracranial infusion of lidocaine reproduced the septal rage phenotype, while lidocaine infusions to the medial septum lead to no detectable changes in behavior (Albert and Richmond, 1976; Albert and Wong, 1978). When these rats are introduced to a mouse, the rats are 50-100% more likely to kill the mouse (Albert and Brayley, 1979). Moreover, they are also more likely to attack another male or female rat (Albert and Wong, 1978). In a separate study, rats with lesions to the ventromedial hypothalamus (VMH) show suppression of aggressiveness and reactivity following electrical stimulation of the LS, while electrical stimulation of the medial septum or cingulate cortex does not affect the animal's aggressive state (Brayley and Albert, 1977). Moreover, a recent study demonstrates that optogenetic activation of the LS in mice engaged in attack will stop the attack, while inhibiting the LS with muscimol, a $GABA_A$ agonist, will increase attacks when mice are engaged in the resident intruder paradigm (Wong et al., 2016). In conclusion, these studies support the notion that activation of the LS functions suppresses aggression while inhibition of the LS promotes aggression.

Recently, the classic role of LS function in suppressing aggression has been challenged by the discovery of a neural circuit from hippocampal CA2 region to dorsal regions of the LS that promotes aggressive behaviors (Leroy et al., 2018). Leroy and colleagues demonstrate that the activation of dorsal LS (dLS) neurons by CA2 pyramidal neurons leads to the inhibition of ventral LS (vLS) neurons and subsequent disinhibition of the VMH. With channelrhodopsin activation of CA2 pyramidal neurons, dLS neurons show an excitatory post-synaptic response, while vLS neurons show an inhibitory post-synaptic response. The authors also demonstrate that loss of CA2 input leads to a decrease in aggressive attacks during the resident intruder paradigm. Overall, these findings begin to shed light on the wiring of neurons in the LS and how the complex structure contributes to aggression behaviors. Most studies investigating LS contribution to aggression have carried out broad manipulations to the LS, thereby limiting the conclusions that can be made about the functional implications of this brain region.

Lateral septum contribution to anxiety-related behaviors

Our understanding of how LS function contributes to fear and anxiety-related behaviors is based on the classical lesion studies previously discussed (Sheehan et al., 2004). The exaggerated aggressive and defensive behaviors displayed following LS lesions have also been interpreted to represent a disinhibition of fear, since rats post-surgery exhibit these exaggerated responses to non-threatening stimuli (Albert and Chew, 1980). Moreover, lesioned rats that undergo contextual fear conditioning also show increased freezing response during testing (Sparks and LeDoux, 1995; Vouimba et al., 1998).

Corticotropin-releasing hormone receptor 2 (Crfr2) has been identified as an important contributor to stress and anxiety (Bale and Vale, 2004). In the LS, a fraction of neurons express

Crfr2, and the injection of Crfr2 agonists causes increased anxiety (Radulovic et al., 2000). Similarly, optogenetic activation of LS Crfr2+ neurons projecting to the anterior hypothalamus promotes anxiety (Anthony et al., 2014). Mice subjected to anxiety-related behavior assays, including open field, elevated plus maze, and light-dark box, show increased anxiety when LS Crfr2+ neurons are activated compared to when LS Crfr2+ neurons are silent.

The role of LS function in anxiety-related behaviors has also been studied under the context of maternal care, stress, and aggression (protecting pups from threats). Female mother mice subjected to a stressful situation during lactation show decreased maternal aggression (Gammie and Stevenson, 2006). Increased c-fos expression is also seen in the LS following the stressful situation. To determine the molecular mechanisms at play in the LS, $GABA_A$ receptors have been identified as playing a role (Lee and Gammie, 2009). Injection of bicuculline, a $GABA_A$ receptor antagonist, reduced the number of attacks exhibited by lactating female mice during displays of maternal aggression. In addition, expression of the oxytocin receptor in the LS is negatively correlated with total movement during open field testing and positive correlated with the amount of nursing done (Curley et al., 2012).

Lateral septum function in feeding behaviors

LS function has also been implicated in feeding behaviors, an innate behavior that is often dictated by mood and emotion. The ventral hippocampus (vHC), which maintains connections with the LS, is also involved in regulating emotional behavior and memory (Moser and Moser, 1998; Fanselow and Dong, 2010). Input from the vHC to the LS regulates feeding (Sweeney and Yang, 2015); chemogenetic activation of vHC glutamatergic neurons in CA3 region and dentate gyrus leads to reduced feeding, while inhibition of LS neurons eliminates

vHC-induced reduction of feeding. These results suggest that vHC innervation of LS neurons affects LS inputs to downstream brain regions that regulate feeding, including the hypothalamus (Betley et al., 2013) and ventral tegmental area (Luo et al., 2011). In addition, the septum (including both LS and MS) to lateral hypothalamic area (LHA) pathway is also important for food intake regulation (Sweeney and Yang, 2016). Activation of vGAT-expressing septal neurons projecting to the LHA caused a reduction in food intake. In summary, these studies provide a better understanding of LS contribution to neural circuits underlying feeding and could lay the foundation for determining therapeutic targets for eating disorders.

Lateral septum regulation of hippocampal theta oscillations

The generation of hippocampal theta oscillations in the brain is implicated in learning and memory (Buzsáki, 2002; Vertes, 2005; Buzsáki and Moser, 2013). Hippocampal theta oscillations are large synchronous EEG signals believed to be important for spatial memory and navigation (Winson, 1978; Buzsáki and Moser, 2013), defensive behaviors (Chee et al., 2015), and locomotion (Sławińska and Kasicki, 1998; Bender et al., 2015). The hippocampus-septum pathway is a critical component of the neural circuit underlying theta oscillation generation (Rawlins et al., 1979). The hippocampus projects to the lateral septum (LS) in a topographical manner, with CA3 inputs projecting primarily to the caudal subregion of the LS (LSc) (Risold and Swanson, 1997a). With innervation by CA3, LSc neurons project to the medial septum (MS) and nucleus of the diagonal band (NDB), which in turn project back to CA3 to mediate the generation of hippocampal theta oscillations (Winson, 1978; Lawson and Bland, 1993; King et al., 1998; Robinson et al., 2016). LS input to the MS is important for the regulation of hippocampal theta and acts as a feedback system for the generation of hippocampal theta (Leung

et al., 1994; Pedemonte et al., 1998; Chee et al., 2015).
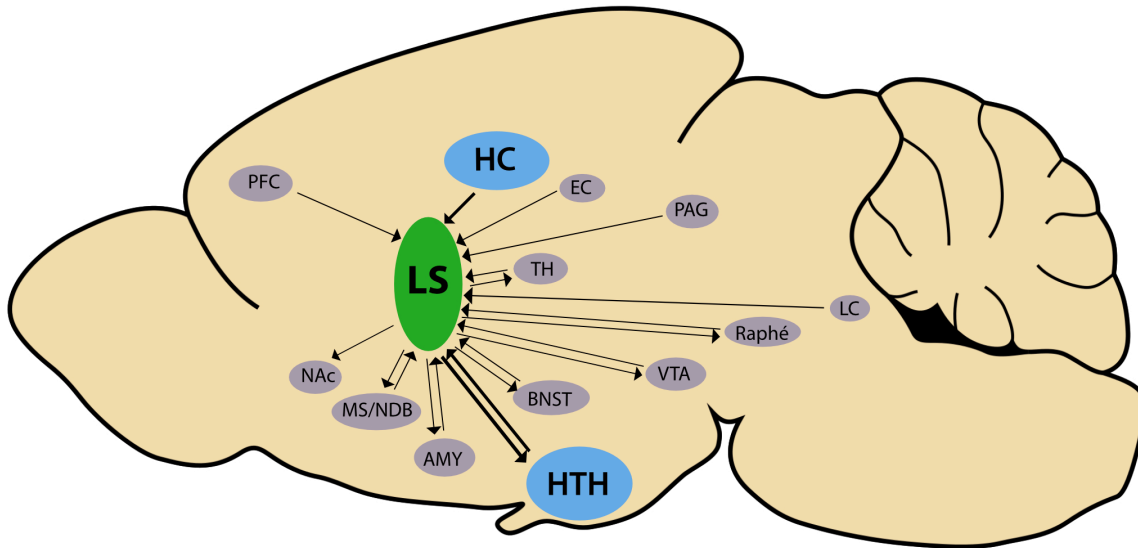
Figure 1.1. Lateral septum neural circuitry.
Schematic of the input and output regions of the LS. Major inputs come from the hippocampus and reciprocal connections are maintained with hypothalamic nuclei. Arrows represent the direction of innervation. Abbreviations: AMY, amygdala; BNST, bed nucleus of the stria terminalis; EC, entorhinal Cortex; HC, hippocampus; HTH, hypothalamus; LS, lateral septum; LC, locus coeruleus; MS/NDB, medial septum/ nucleus of the diagonal band; NAc, nucleus accumbens; PAG, periaqueductal gray; Raphé, Raphé nuclei; TH, thalamus, VTA, ventral tegmental area.

CHAPTER 2: TMEM16B REGULATES ACTION POTENTIAL FIRING IN THE LATERAL SEPTUM AND AGGRESSION IN MALE MICE

INTRODUCTION

TransMEMbrane protein of unknown function 16B (TMEM16B, also known as Anoctamin-2 or Ano2) is a Calcium-activated Chloride Channel (CaCC) important for regulating neuronal signaling throughout the central nervous system, including the hippocampus (Huang et al., 2012), inferior olive (Zhang et al., 2017), thalamus (Ha et al., 2016), retina (Stöhr et al., 2009), and olfactory epithelium (Pietra et al., 2016). Amongst these brain regions, TMEM16B regulates excitatory postsynaptic potential (EPSP) amplitude (Huang et al., 2012), spike duration (Huang et al., 2012), spike frequency (Pietra et al., 2016; Zhang et al., 2017), and/or spike frequency adaptation (Ha et al., 2016). TMEM16B activation, either by calcium influx or release of internally stored calcium, leads to chloride currents that help maintain the membrane potential below threshold for spike firing (Pifferi et al., 2009; Stephan et al., 2009; Stöhr et al., 2009; Sagheddu et al., 2010). Since calcium influx typically accompanies or induces neuronal signaling, TMEM16B provides a powerful means of regulating neuronal activity. Understandably, elimination of TMEM16B can lead to behavioral deficits. TMEM16B knockout mice display impaired motor learning correlated with changes in inferior olivary neuronal spike frequency (Zhang et al., 2017), and behavioral deficits in odor-guided food finding indicative of CaCC mediation of olfactory sensory neuron signal amplification (Pietra et al., 2016). Mice with TMEM16B viral knockdown in the thalamus exhibit increased visceral pain responses and decreased spike firing adaptation of thalamocortical neurons (Ha et al., 2016).

The lateral septum (LS) is a brain region highly implicated in aggression (Spiegel et al., 1940; Brady and Nauta, 1953; Albert and Chew, 1980). LS lesions in mammals lead to dramatic displays of aggression, first coined as "septal rage," and characterized by increased biting, attacks, and defensive behaviors (Spiegel et al., 1940; Brady and Nauta, 1953, 1955). Similar behavioral alterations result from injection of local anesthetics into the LS (Albert and Richmond, 1976; Albert and Wong, 1978). In support of these findings, LS input to the ventromedial hypothalamus (VMH) is responsible for dampening aggression (Brayley and Albert, 1977; Wong et al., 2016). The LS is primarily composed of GABAergic projection neurons (Risold and Swanson, 1996). Of the three subregions that comprise the LS— the caudal LS (LSc), rostral LS (LSr), and ventral LS (LSv)—the VMH receives input primarily from the LSv (Risold and Swanson, 1997; Toth et al., 2010). The hippocampus is a major source of input to the LS (Risold and Swanson, 1997). A recent study identified a neural circuit involving hippocampal CA2 pyramidal neurons in regulating LS input to the VMH, whereby CA2 innervation of neurons in the dorsal regions of the LS (including the LSc and LSr) leads to LSv inhibition and VMH disinhibition so as to trigger aggression (Leroy et al., 2018). This circuit demonstrates the complexity of LS function in regulating aggression.

A survey of TMEM16B mRNA expression patterns using the Allen Brain Atlas ISH Database localizes TMEM16B expression to the LSc and LSr, but not the LSv. We have validated TMEM16B expression in these LS subregions with immunohistochemical staining of mice with farnesylated mCherry inserted into the TMEM16B locus – which is simultaneously knocked out in the process (Zhang et al., 2017)– and these results have led us to speculate that TMEM16B channels may play a functional role in regulating LS neural circuitry and aggressive behaviors.

In this study, we used this TMEM16B mCherry mouse line (Zhang et al., 2017) to determine how CaCC contributes to LS neuronal signaling and aggressive behaviors. We found that TMEM16B KO mice display prolonged aggressive attacks compared to wildtype (WT) control mice. We identified a calcium-activated chloride current in the LS of WT but not KO mice, and showed that TMEM16B regulates spike frequency and spike frequency adaptation in subpopulations of LS neurons. Collectively, these findings suggest that TMEM16B functions to regulate spike firing in LS neurons, and loss of TMEM16B leads to increased spike firing and longer displays of aggression in male mice.

RESULTS

TMEM16B is expressed in the mouse lateral septum

To examine the expression of TMEM16B in the LS, we used a TMEM16B knockout mouse line generated in-house (Zhang et al., 2017), wherein a farnesylated mCherry marker followed by a stop codon is expressed in-frame at Exon 3. This results in expression of mCherry that is associated with the cell membrane in cells normally expressing TMEM16B in heterozygous control mice, as well as homozygous mice with loss (KO) of TMEM16B function. Using this mouse line, we identified mCherry expression in the LS in a series of slices along the anterior-posterior axis (Fig. 2.1*A*), and observed expression in the LSc and LSr, but not the LSv. As revealed by double labeling of TMEM16B KO brain sections with mCherry and the pan-neuronal marker NeuN (Fig. 2.1*B,C*), quantification of NeuN+ cells co-labeled with mCherry indicates that the great majority (93.91% ± 1.326%; mean ± SEM) of LS neurons are TMEM16B-expressing neurons (Fig 2.1*D*). Double-labeling of mCherry with other cell markers,

including GFAP for astrocytes and Iba1 for microglia, showed little overlap, with 5.781% ± 1.239% of LS astrocytes expressing mCherry and 2.172% ± 0.596% of LS microglial cells expressing mCherry, suggesting that TMEM16B expression is restricted to LS neurons (Fig. 2.2). Based on these results, we conclude that TMEM16B is expressed in neurons and not in other cell types in the LS. Furthermore, we were able to determine the output regions of TMEM16B-expressing LS neurons based on the farnesylated mCherry expression. We identified mCherry nerve fibers in certain brain regions, including the lateral preoptic area (LPO) and lateral hypothalamic area (LHA) (Fig. 2.3). Since no TMEM16B mRNA expression was seen in these regions, the mCherry expression we observed could be attributed to LS neuronal projections that express TMEM16B. Neuronal tracing studies have identified both LSc and LSr input to both the LPO and LHA (Risold and Swanson, 1997), consistent with the notion that TMEM16B-expressing LS neurons project to these areas of the hypothalamus. We also found mCherry nerve fibers in LSv (Fig. 2.3*D*), indicating that LSv neurons without TMEM16B expression receive input from TMEM16B expressing LS neurons.

TMEM16B KO mice spend more time engaged in aggressive behavior

Given the robust expression of TMEM16B in LS neurons, we hypothesized that loss of TMEM16B function may lead to LS-related behavioral deficits. Studies examining LS function have identified its role in regulating aggression (Brady and Nauta, 1953; Albert and Chew, 1980; Wong et al., 2016; Leroy et al., 2018). Based on this rationale, we wondered whether TMEM16B expression in the LS is indicative of a potential involvement in aggression. To look into this possibility, we performed a series of behavioral tests designed to examine aggressive behaviors

in TMEM16B knockout mice and compared these mutants with WT littermate controls to look

for behavioral phenotypes (Fig. 2.4).

Because mouse aggression has typically been studied in male mice, we generated a

cohort of adult male TMEM16B WT ($n = 36$) and KO mice ($n = 34$) for behavioral analysis

using a resident intruder paradigm, which would be carried out over three consecutive days (Fig.

2.4A). We found that TMEM16B KO mice spent significantly more time attacking the intruder

than WT mice on Days 2 and 3 (Fig. 2.4B; repeated measures 2-way ANOVA, sources of

variation: Day $F_{(2,136)} = 4.860$, $p = 0.0091$, Genotype $F_{(1,68)} = 8.428$, $p = 0.005$, Interaction $F_{(2,136)}$

$= 2.853$, $p = 0.0611$; Sidak's multiple comparison: Day 1 $p = 0.9347$, Day 2 $p = 0.0081$, and Day

3 $p = 0.0141$). On Day 3, TMEM16B KO mice exhibited attacks of significantly longer duration

when compared to WT mice (Fig. 2.4C; repeated measures 2-way ANOVA, sources of variation:

Day $F_{(2,136)} = 4.860$ ($p = 0.009$), Genotype $F_{(1,68)} = 8.428$ ($p = 0.005$), Interaction $F_{(2,136)} = 2.853$,

$p = 0.0611$; Sidak's multiple comparison: Day 1 $p = 0.8654$, Day 2 $p = 0.1093$, and Day 3 $p =$

0.0015). No significant difference was found in the total number of attacks across all three days

between TMEM16B WT and KO (Fig. 2.4D; repeated measures two-way ANOVA test; sources

of variation: Day $F_{(2,134)} = 6.763$ ($p = 0.0016$), Genotype $F_{(1,67)} = 3.809$ ($p = 0.0552$) Interaction

$F_{(2,134)} = 0.9288$ ($p = 0.3976$); Sidak's multiple comparison: Day 1 ($p = 0.7632$), Day 2 ($p =$

0.3673), and Day 3 ($p = 0.0655$)). These findings revealed that loss of TMEM16B function led

to an increased duration of aggressive displays towards intruders.

In order to determine whether the resident intruder paradigm revealed a phenotype in

aggression rather than a difference in social interaction behavior, we performed additional

behavioral tests (Fig. 2.5). A subset of the behavioral cohort underwent a direct social interaction

test, and TMEM16B KO mice showed no significant alteration in the amount of direct

interaction time with a social stimulus mouse (Student's t-test, $p = 0.3102$, WT $n = 13$, KO $n =$ 13). Subjecting the same subset of mice (WT $n=16$, KO $n=14$) to the two-chamber social approach test also revealed no significant difference between TMEM16B KO mice and WT littermate controls (Fig. 2.5). During the habituation trial, TMEM16B KO mice as well as WT controls showed no preference for either side of the chamber with respect to the number of sniffing or "interaction zone" bouts (Fig. 2.5*B*; repeated measures 2-way ANOVA; sources of variations: Interaction $F_{(1,28)} = 2.288$ [$p = 0.1416$], Genotype $F_{(1,28)} = 2.155$ [$p = 0.1533$], and Chamber side $F_{(1,28)} = 0.4520$ [$p = 0.5069$]; Sidak's multiple comparisons: WT $p = 0.0740$, KO $p = 0.9994$), interaction time (Fig. 2.5*C*; repeated measures 2-way ANOVA; sources of variations: Interaction $F_{(1,28)} = 1.557$ [$p = 0.2224$], Genotype $F_{(1,28)} = 0.1053$ [$p = 0.7480$], and Chamber side $F_{(1,28)} = 2.790$ [$p = 0.1060$]; Sidak's multiple comparisons: WT $p = 0.0814$, KO $p = 0.9492$), and time spent on each side of the chamber (Fig. 2.5*D*; repeated measures 2-way ANOVA; sources of variations: Interaction $F_{(1,28)} = 1.101$ [$p = 0.3030$], Genotype $F_{(1,28)} = 0.01947$ [$p = 0.89$], and Chamber side $F_{(1,28)} = 0.6823$ [$p = 0.4158$]; Sidak's multiple comparisons: WT $p = 0.9834$, KO $p = 0.3754$). During the social trial, both TMEM16B KO mice and WT controls showed a clear preference for the side of the chamber containing the social stimulus mouse with respect to interaction bouts (Fig. 2.5*E*; repeated measures 2-way ANOVA; sources of variations: Interaction $F_{(1,28)} = 0.5851$ [$p = 0.4507$], Genotype $F_{(1,28)} = 2.957$ [$p = 0.0966$], and Chamber side $F_{(1,28)} = 105.3$ [$p < 0.0001$]; Sidak's multiple comparisons: WT $p < 0.0001$, KO $p < 0.0001$), interaction time (Fig. 2-1*F*; repeated measures 2-way ANOVA; sources of variations: Interaction $F_{(1,28)} = 0.1643$ [$p = 0.6883$], Genotype $F_{(1,28)} = 0.4747$ [$p = 0.4965$], and Chamber side $F_{(1,28)} = 152.2$ [$p < 0.0001$]; Sidak's multiple comparisons: WT $p < 0.0001$, KO $p < 0.0001$), and time spent on each side of the chamber (Fig. 2.5*G*; repeated measures 2-way ANOVA; sources of

variations: Interaction $F_{(1,28)} = 0.5545$ [$p = 0.4627$], Genotype $F_{(1,28)} = 1.455$ [$p = 0.2378$], and

Chamber side $F_{(1,28)} = 57.52$ [$p < 0.0001$]; Sidak's multiple comparisons: WT $p < 0.0001$, KO $p <$

0.0001). Taken together, these results suggest that TMEM16B KO mice do not show any deficits

in social approach behavior and thus the phenotype observed in the resident intruder paradigm

cannot be explained by confounding variables due to impaired social behavior.

As an additional control experiment, we determined how the single housing set up during

the resident intruder paradigm affected anxiety levels in TMEM16B WT and KO littermates. We

administered various anxiety-related behavioral tests and found no deficits in anxiety-related

behaviors (Fig. 2.6). A subset of the cohort (WT $n = 16$, KO $n = 14$) underwent the elevated plus

maze test (Fig. 2.6A), which showed no significant difference in the percent of time spent in the

open arms (Student's t-test, $p = 0.7947$, see Table 2.1) or the fraction of distance traveled in the

open arms compared to the total distance traveled (Student's t-test, $p = 0.7103$). These singly

housed TMEM16B KO mice also displayed no anxiety-related behavior phenotypes during the

light-dark box test (Fig. 2.6B). No significant difference was detected in the percent of time spent

on the light side of the box (Student's t-test, $p = 0.4621$) nor the percent of entries into the light

side of the box (Student's t-test, p=0.2200). All mice in the cohort also underwent the open field

test (Figure 2.6C; WT $n = 35$, KO $n = 34$), which revealed no significant difference in the

fraction of movement in the center compared to the total movement (Student's t-test, $p =$

0.8232). In addition, no significant difference in rearing (Student's t-test, $p = 0.6361$) or fine

movement (Student's t-test, $p = 0.0773$) were detected. TMEM16B KO mice did however,

display small but significant increases in ambulatory movement (Student's t-test, $p = 0.0156$). A

minute-by-minute comparison of total movement detected significance during specific time

points of the test (multiple Student's t-test, p values see Table 2.1).

Since TMEM16B is expressed in photoreceptor cells, we decided to test whether the observed aggression phenotype involves alteration of TMEM16B function in the retina. We ran a subset of the cohort (WT $n = 16$, KO $n = 13$) through the Morris Water Maze cued platform training test (MWM) (Fig. 2.7). During MWM, TMEM16B KO mice displayed no deficits in visual function compared to WT littermates with respect to the latency to reach the platform (Fig. 2.7*A*; multiple Student's t-test, see Table 2.2), distance traveled to reach the platform (Fig. 2.7*B*; multiple Student's t-test, see Table 2.2), and swim speed (Fig. 2-2*C*; multiple Student's t-test, see Table 2.2). In addition, all mice underwent the visual placing response, a basic neurological assessment of vision. All mice in the cohort displayed a visual response. Overall, these observations support the notion that TMEM16B KO mice display more aggressive behavior.

Major excitatory synaptic inputs to the lateral septum are maintained in TMEM16B KO mice

Based on the results from the resident intruder paradigm, we reasoned that TMEM16B may contribute to the function of LS neurons involved in regulation of aggression. In the hippocampus, TMEM16B resides within the nanodomains (Augustine et al., 2003) of excitatory glutamate receptors and regulates EPSP amplitude in CA1 neurons (Huang et al., 2012). We therefore tested whether TMEM16B affects excitatory post-synaptic responses in LS neurons.

To determine whether synaptic responses of LS neurons are altered in the TMEM16B KO mice, we utilized optogenetics to stimulate projections from specific input regions (Fig. 2.8*A*). The LS receives inputs from a variety of brain regions associated with the limbic system (Sheehan et al., 2004). We chose to focus on two major input regions: the hippocampus and the

hypothalamus (Swanson and Cowan, 1979; Staiger and Nürnberger, 1991b, a; Risold and Swanson, 1996, 1997). Based on the high mCherry expression we observe in the LSc, we chose hippocampal CA3 region and the lateral hypothalamic area (LHA) as injection sites because these brain regions innervate the LSc (Risold and Swanson, 1997). Using a stereotaxic technique, we gave unilateral injections of the AAV5-CAMKII-hChR2(H134R)-EYFP virus into either CA3 or LHA. This allowed us to express channelrhodopsin (ChR2) specifically in excitatory projection neurons that innervate LS neurons. Following stereotaxic injections, brains were sliced and prepared for whole cell recordings in ACSF solution with 100 μM PTX.

ChR2 at the axon terminals of presynaptic neurons from the input region with viral injection was activated by blue light filtered through 1 mm thick 470/40 nm excitation filters with 1 ms light pulses, and the evoked excitatory post-synaptic potentials (EPSPs) were recorded from LS neurons (Fig. 2.8B). When examining evoked EPSPs due to one input source alone, we found no significant differences in EPSP peak amplitude (Fig. 2.8C; ordinary 2-way ANOVA; sources of variations: Interaction $F_{(1,82)}$ = 1.044 [p = 0.3098], Genotype $F_{(1,82)}$ = 0.0045 [p = 0.9465], brain region $F_{(1,82)}$ = 27.78 [$p < 0.0001$]; Tukey's multiple comparisons: WT LHA vs WT CA3 p = 0.0003, WT LHA vs KO LHA p = 0.8855, WT LHA vs KO CA3 p = 0.0019, WT CA3 vs KO LHA p = 0.0020, WT CA3 vs KO CA3 p = 0.8893, KO LHA vs KO CA3 p = 0.0117), or EPSP halfwidth (Fig. 3D; ordinary 2-way ANOVA; sources of variations: Interaction $F_{(1,100)}$ = 3.874 [p = 0.0518], Genotype $F_{(1,100)}$ = 0.8975 [p = 0.3457], brain region $F_{(1,100)}$ = 21.07 [$p < 0.0001$]; Tukey's multiple comparisons: WT LHA vs WT CA3 p = 0.2797, WT LHA vs KO LHA p = 0.8754, WT LHA vs KO CA3 p = 0.0008, WT CA3 vs KO LHA p = 0.0599, WT CA3 vs KO CA3 p = 0.2009, KO LHA vs KO CA3 $p < 0.0001$) between TMEM16B KO and WT neurons. However, when we compared evoked EPSPs due to CA3 input with evoked

EPSPs due to LHA input, we found that CA3-evoked EPSPs showed a greater peak amplitude compared to that of LHA-evoked EPSPs (Fig. 2.8*C*). This was the case in both WT neurons and TMEM16B KO neurons, suggesting that these excitatory synaptic inputs to the LS are maintained in the TMEM16B KO mice.

We verified the viral injection into hippocampus and lateral hypothalamic area via immunofluorescence (Fig. 2.8*A*); CA3 as well as CA2 neurons express ChR2-EYFP and could correspond to the optogenetically activated neurons that excite LS neurons in the dorsal regions including LSc and LSr (Leroy et al., 2018). Immunofluorescence images of ChR2-EYFP expression in the LS were also characterized (Fig. 2.8*E*), revealing bilateral and dense hippocampal projections in contrast to the unilateral and sparse projection from LHA. Overall, these results suggest that synaptic connections to the LS are maintained and unaffected in TMEM16B KO mice.

Calcium-activated chloride currents are present in LS neurons of WT but not TMEM16B KO mice

To test whether TMEM16B channels are functional in LS cell bodies, we recorded calcium-activated tail currents in voltage clamp mode (Fig. 2.9). To isolate the contribution of calcium-activated chloride currents, we used ACSF where NaCl was replaced with NMDG-Cl, which also contained TEA-Cl and 4-AP to block K^+ channels. The internal solution included CsCl and TEA-Cl in lieu of KCl to eliminate outward currents due to K^+ efflux. Cl^- concentrations were high in both solutions to generate a theoretical E_{Cl} of 0 mV. Cells were held at -70 mV and pulsed to 0 mV for 1 s to allow for activation of voltage-gated calcium channels and Ca^{2+} influx (Fig. 2.9*A*, black traces). Cells were then pulsed down to -90 mV to elicit tail

currents at a potential with a large outward driving force for Cl⁻ to induce efflux. As a same cell

negative control, cells were then pulsed from -70 mV to +100 mV to activate Ca_v channels but

eliminate the inward driving force for Ca^{2+} ions, with the goal of reducing the intracellular

concentration of Ca^{2+} available to activate CaCCs (Fig. 2.9*A*, blue traces). Using this protocol,

we found that WT LS neurons displayed CaCC tail current of 523.9 ± 88.51 pA (mean ± SEM)

with a 0 mV prepulse, which decreased significantly to 76.41 ± 13.8 pA with a +100 mV

prepulse. In contrast, TMEM16B KO LS neurons displayed a mean CaCC tail current of $90.26 \pm$

30.81 pA with a 0 mV prepulse and 59.47 ± 10.09 pA with a +100 mV prepulse (Fig. 2.9*B*;

repeated measures 2-way ANOVA, sources of variation: Interaction $F_{(1,25)} = 24.49$ [$p < 0.0001$],

Genotype $F_{(1,25)} = 25.39$ [$p < 0.0001$], and Membrane potential $F_{(1,25)} = 32.26$ [$p < 0.0001$] ;

Sidak's multiple comparisons: WT $p < 0.0001$, KO $p = 0.8273$). These results suggest that LS

neurons express functional CaCCs that can be eliminated by KO of TMEM16B.

TMEM16B regulates spike frequency in subpopulations of LS neurons

Once we confirmed the presence of a functional CaCC in WT LS neurons but not

TMEM16B KO LS neurons, we investigated the contribution of TMEM16B to neuronal

excitability in these cells. TMEM16B has previously been shown to regulate spike frequency

and/or spike frequency adaptation in various brain regions, including the inferior olivary nucleus

(Zhang et al., 2017), thalamacortical neurons (Ha et al., 2016), and the olfactory bulb (Pietra et

al., 2016). Hence, we compared spike firing properties between LS neurons of TMEM16B KO

mice and WT controls (Fig. 2.10).

LS neurons were recorded in current clamp mode and given 1 s current injections of

increasing amplitude. The ACSF included 100 μM PTX and 1 mM kynurenic acid to block all

synaptic inputs. We found that LS neurons exhibited variability in their spike firing characteristics and we could functionally categorize the neurons into three easily distinguishable types, which we denoted as "tonic cells" (Fig. 2.10*A*; WT *n* = 29, KO *n* = 38), "phasic cells" (Fig. 2.10*B*; WT *n* = 32, KO *n* = 37), and "burst cells" (Fig. 2.10*C*; WT *n* = 17, KO *n* = 22). Our identification of subpopulations of LS neurons is consistent with previously published studies, which describe LS neurons with similar firing patterns (Gallagher et al., 1995; Kodirov et al., 2014). Tonic cells were characterized by regular and repetitive firing throughout the pulse duration. As current injection amplitude was elevated, tonic KO neurons showed increased spike frequency compared to tonic WT neurons (Fig. 2.10*A*; multiple Student's t-test, for *p* values see Table 2.3). Tonic TMEM16B KO cells also displayed a significant increase in instantaneous frequency in the first few spikes fired during the current pulse as compared to WT (Fig. 2.10*D*; multiple Student's t-test, for *p* values see Table 2.4), suggesting that TMEM16B plays a role in regulating the instantaneous frequency of spike firing immediately after depolarization. Phasic cells were characterized by action potential firing exclusively at the beginning of the pulse duration, followed by quiescence, which could only be relieved by removal of the current injection. With elevated current injection amplitude, phasic KO neurons also showed increased spike frequency compared to Phasic WT neurons (Fig. 2.10*B*; multiple Student's t-test, see Table 2.3). A third cell type, which we denoted as "burst cells", demonstrated cyclic spike firing (Fig. 2.10*C*). No significant difference in spike frequency or spike frequency adaptation was detected in burst cells in TMEM16B KO vs WT (Fig. 2.10*C*, multiple Student's t-test, for *p* values see Table 2.3; Fig. 2.8*E*, multiple Student's t-test, for *p* values see Table 2.4). In conclusion, our findings suggest that TMEM16B regulates spike frequency and spike frequency adaptation in subpopulations of LS neurons.

DISCUSSION

In this study, we found that a majority of neurons in the LSc and LSr are marked by mCherry in a TMEM16B mCherry KO mouse line (Zhang et al., 2017), indicative of TMEM16B expression in these dorsal regions of LS. We investigated male aggression in mutant mice with loss of TMEM16B function, and found that TMEM16B regulates the length of time mice are engaged in aggressive behaviors. Furthermore, we found that activation of voltage-gated calcium channels in LS neurons resulted in a calcium-activated chloride tail current, which was eliminated in mutants with loss of TMEM16B function. Consistent with this finding of CaCC activation following calcium influx through calcium channels, we identified TMEM16B function in regulating spike frequency and spike frequency adaptation in LS neurons.

Our results suggest that the loss of the ostensibly inhibitory chloride currents through TMEM16B channels increases the neuronal excitability of subpopulation of LS neurons and increases aggressive behaviors in male mice. Our findings are in agreement with the neural circuit for regulating aggression via hippocampal CA2 innervation of the LS (Leroy et al., 2018). This recent study demonstrates that the dorsal LS, which overlaps with LS regions we refer to as the LSc and LSr (Risold and Swanson, 1997), receives excitatory input from CA2 as well as CA3; activation of dorsal LS inhibits downstream LSv neurons, thus silencing their inhibitory input to the VMH. Consequently, silencing CA2 reduces aggression in male mice during the resident intruder paradigm. Given our finding that loss of TMEM16B function leads to increased spike firing in dorsal LS neurons, TMEM16B KO mice likely have strengthened inhibition of the LSv neuron by other LS neurons that normally express TMEM16B, leading to disinhibition of the VMH and an increase in aggressive behaviors as we observed.

In conclusion, our findings support the notion that activation of dorsal regions of the LS promotes aggression (Leroy et al., 2018). Although the classical understanding attributes LS function to suppressing aggression, many of these studies involved broadly manipulating the LS, either via lesions (Spiegel et al., 1940; Brady and Nauta, 1953; Albert and Richmond, 1976), electrical stimulation (Brayley and Albert, 1977), or optogenetic activation (Wong et al., 2016). Thus, these studies do not take into account the complex LS microcircuitry that has only begun to be elucidated (Leroy et al., 2018). Connections between LS subregions are known to be organized in such a way that LS neurons within an individual subregion maintain connections with one another, while also projecting in dorsoventral and mediolateral directions to neighboring LS subregions (Alonso and Frotscher, 1989; Staiger and Nürnberger, 1991b; Risold and Swanson, 1997). Further investigation of the mechanisms underlying LS microcircuit function is necessary to better understand its regulation of aggression.

Whereas our study supports the notion that TMEM16B expressing LS neurons in dorsal regions are excited by hippocampal neurons to cause disinhibition of VMH leading to aggressive behaviors, it remains possible that additional hypothalamic nuclei are involved in regulating aggression. We identified mCherry expression of LS axon terminals in downstream hypothalamic regions, namely the LHA and LPO (Fig. 1-2). These results are consistent with LS connectivity studies revealing innervation of the LHA and LPO by both the LSc and LSr (Risold and Swanson, 1997). Notably, electrical stimulation of the LHA leads to increased aggressive behavior (Smith et al., 1970; Woodworth, 1971; Koolhaas, 1978; Kruk et al., 1983), and reciprocal connections exist between the VMH and LHA (Canteras et al., 1994). Moreover, the LPO maintains reciprocal connections with the medial preoptic area (MPO), another

hypothalamic nucleus implicated in aggression (Chiba and Murata, 1985; Albert et al., 1986). Therefore, LS input to the LHA and LPO may contribute to regulating aggression as well.

Future study of the brain regions that receive innervation of TMEM16B-expression LS neurons, whether it be the LSv or downstream hypothalamic nuclei, would be instrumental in understanding how LS neurons are integrated within the broader neuronal circuitry underlying aggressive social behaviors. It seems likely that the change in spike frequency and spike frequency adaptation detected in subpopulations of LS neurons lacking TMEM16B would correlate with changes in postsynaptic activity in downstream neurons. Moreover, examination of the specific projections of the TMEM16B expressing LS neurons may provide additional insight regarding the circuits involved in regulating aggressive behaviors.

In summary, our study of TMEM16B in the lateral septum provides the first demonstration of the presence and function of calcium-activated chloride channels in this brain region. Our investigation of the role of TMEM16B at the physiological and behavior levels provides insight into how TMEM16B regulates LS neuronal excitability. Our study raises intriguing questions regarding how LS function and regulation may contribute to aggressive behavior. It also provides an example as to how different subregions of the LS in this complex neural circuit may have different channel compositions for activity modulation and vary in their contributions to the regulation of aggression and related behaviors.

MATERIALS AND METHODS

ANIMALS

All experimental mice used in this study were bred from the TMEM16B mCherry KO mouse line (Zhang et al., 2017). All animal experiments were done in strict accordance with the *Guide for the Care and Use of Laboratory Animals* by the National Institutes of Health. All animal protocols used in this study were approved by the Institutional Animal Use and Care Committee at the University of California San Francisco.

ACUTE BRAIN SLICE PREPARATION

Male and female TMEM16B WT and KO mice ages 16- 32 weeks old were anesthetized using isoflurane and perfused with ice-cold NMDG-based cutting solution (in mM): 93 NMDG, 2.5 KCl, 1.2 NaH_2PO_4, 20 HEPES, 25 glucose, 5 Sodium Ascorbate, 2 Mannitol, 3 Sodium Pyruvate, 10 $MgSO_4$, 0.5 $CaCl_2$, pH ~7.3-7.4, ~300-310 mOsm. Brains were immediately removed and submerged in ice-cold NMDG cutting solution. Brains were sliced into 350 μm sections using a Leica VT 1000S vibratome (Leica Biosystems, Buffalo Grove, IL). Slices were placed in a holding chamber in NMDG-based cutting solution at 33^OC for 15 minutes, then transferred to a second holding chamber at room temperature containing HEPES-based ACSF solution (in mM): 92 NaCl, 2.5 KCl, 1.2 NaH_2PO_4, 30 $NaHCO_3$, 20 HEPES, 25 Glucose, 5 Sodium Ascorbate, 2 Mannitol, 3 Sodium Pyruvate, 2 $MgSO_4$, 2 $CaCl_2$, pH 7.3-7.4, ~300-310 mOsm. All solutions were equilibrated with 5% CO_2 + 95 % O_2. Slices were held at room temperature for at least 45 minutes before being used for recordings.

SLICE ELECTROPHYSIOLOGY AND OPTOGENETIC RECORDINGS

Whole-cell patch clamp recordings were performed on prepared brain slices and continuously perfused with ACSF using a peristaltic pump and equilibrated with 5% CO_2 + 95 % O_2. For EPSP and action potentials recordings, slices were perfused with ACSF using the following recipe (in mM): 127 NaCl, 1.8 KCl, 26 $NaHCO_3$, 12 KH_2PO_4, 1.3 $MgSO_4$, 2.4 $CaCl_2$, 15 glucose. The pH was adjusted to within a range of 7.3-7.4 using HCl. Osmolarity was adjusted to a range of 300-305 mOsm. A K-Methanesulfonate-based internal solution was used (in mM): 135 K-Methanesulfonate, 6.5 KCl, 2 $MgCl_2$, 4 Na-ATP, 0.2 EGTA, 10 HEPES, pH ~7.2 with KOH, ~290-300 mOsm. The slice chamber was kept at 33^OC during recordings.

For tail current recordings, slices were perfused with an NMDG-Cl ACSF solution (in mM): 120 NMDG, 20 HEPES, 1.3 $MgSO_4$, 2.5 $CaCl_2$, 5 TEA-Cl, 15 glucose. A CsCl-based internal solution was used (in mM): 135 CsCl, 10 HEPES, 10 TEA-Cl, 2 $MgCl_2$, 0.1 EGTA, pH ~7.2 with Cs OH, ~290-300 mOsm. The slice chamber was kept at room temperature during recordings.

All recordings were done using the patch clamp amplifier, MultiClamp700B (Molecular Devices, San Jose, CA), the data acquisition system Digidata 1322A (Molecular Devices, San Jose, CA), Axioskop2 FS plus upright microscope (Carl Zeiss Microscopy, Jena, Germany), and Clampex9 (Molecular Devices, San Jose, CA). Neurons were visualized with a CCD Camera (Hamamatsu, Hamamatsu City, Japan). Pipette tips were pulled the day of use with a P-1000 Pipette Puller (Sutter Instruments, Novato, CA) with seal resistances of 4-9 MΩ. Pipette tips were made of thick/standard wall borosilicate glass (ID 0.86 mm, OD 1.50 mm). Optogenetic recordings were done using a Lambda DG4 light source (Sutter Instruments, Novato, CA). Neutral density filters were used to regulate light intensity and determine the threshold amount of

light necessary for EPSP activation. Pharmacological drugs used include 100 μM Picrotoxin (Tocris), 1 mM Kynurenic Acid (Sigma Aldrich), 5 mM 4-Aminopyridine (Sigma Aldrich), and 10 mM TEA-Cl (Sigma Aldrich). All drugs were dissolved in the ACSF solution. All electrophysiology data was analyzed using Clampfit10 and Graphpad Prism 6 (GraphPad Prism, RRID: SCR_002798).. Only cells with access resistance < 40 MΩ were analyzed. Passive leak was subtracted from tail current recordings offline prior to subsequent analysis.

IMMUNOHISTOCHEMISTRY

Male and female TMEM16B KO mice 4-5 weeks old were anesthetized using isoflurane and perfused with 1x phosphate buffered saline (PBS), followed by 4% Paraformaldehyde (PFA) in 1x PBS. After brain dissection, brains were placed in 4% PFA for 4 hours followed by 30% sucrose for two days. Brains were frozen in OCT and sectioned into 30 um thick coronal sections using a Leica CM3050 S cryostat (Leica Microsystems, Buffalo Grove, IL). Brain sections not used immediately were stored in cryoprotectant solution at -20°C (40% 1X PBS, 30% ethylene glycol, 30% glycerol).

Brain sections underwent free-floating immunohistochemistry (IHC) for antibody labeling. Sections were washed in 1x PBS for 5 min, and then placed in boiling citrate buffer solution (0.05% Tween 20, 114 mM sodium citrate, pH 6.0) for 5 min to perform antigen retrieval. Following two 3 min 1x PBS washes for cool-down, sections were incubated in blocking solution (0.3% Triton, 3% Normal Goat Serum in 1x PBS) for one hour at room temperature. Sections were incubated in primary antibodies diluted with blocking solution overnight at 4°C. Primary antibodies used include mouse monoclonal anti-NeuN 1:500 (Millipore Cat# MAB377, RRID: AB_2298772), rabbit polyclonal anti-DsRed-Express

1:2500 (Clontech Laboratories, Inc. Cat# 632496, RRID: AB_10013483), rabbit polyclonal anti-GFAP 1:100 (Sigma-Aldrich Cat# G9269, RRID: AB_477035) Rabbit polyclonal anti-Iba1 1:1500 (Wako Cat# 019-19741, RRID: AB_839504), and chicken polyclonal anti-mCherry 1:4000 (Novus Cat# NBP2-25158, RRID: AB_2636881). Sections underwent three 10 min 1x PBS washes. Secondary antibodies diluted with blocking solution were applied to sections for 1 hour at room temperature. Secondary antibodies include Goat Anti-Mouse IgG (H+L) Alexa 488 1:1000 (Thermo Fisher Scientific Cat# A-11001, RRID: AB_2534069), Goat Anti-Rabbit IgG (H+L) Alexa 568 1:1000 (Molecular Probes Cat# A-11036, RRID: AB_143011), Goat Anti-Rabbit IgG (H+L) Alexa488 1:1000 (Molecular Probes Cat# A-11008, RRID: AB_143165), and Goat Anti-Chicken IgY# (IgG)(H+L) Cy3 1:1000 (Jackson ImmunoResearch Labs Cat# 103-165-155, RRID: AB_2337386). Next, sections underwent three 10 min 1x PBS washes. Sections were mounted onto Superfrost Plus Microscope Slides (Thermo Fisher Scientific, Waltham, MA). Glass coverslips were placed on top of the slides using 150 μl DAPI Fluoromount-G mounting media (SouthernBiotech, Birmingham, AL).

MICROSCOPY AND CELL COUNT ANALYSIS

All fluorescent imaging was done using a Leica SP5 or Leica SP8 confocal microscope (Leica Microsystems, Buffalo Grove, IL). Tile scan images were taken at 20x magnification. LS cell count images were taken at 63x magnification. The LS was divided into 6-7 equal areas based on the location of mCherry expression. Z-stack confocal images with 3 um z-step sizes were taken of each LS area and cells double-labeled for mCherry and the specific cell type marker were manually counted throughout the entire stack using ImageJ (ImageJ, RRID: SCR_003070). The number of double-labeled cells was summed up across all areas of the LS

from both brain hemispheres. The sample size for the cell count analysis was n=5. For each sample, two 30 μm sections were selected for cell count analysis.

BEHAVIORAL ASSAYS

Male TMEM16B WT and KO mice 20-33 weeks of age were transferred to the Gladstone Behavioral Core and acclimated to new housing at least 2 weeks prior to any testing. Researchers conducting all behavioral tests were blinded to the mouse genotype during testing and analysis. Statistical analysis for all behavioral tests was completed using Graphpad Prism 6 (GraphPad Prism, RRID: SCR_002798).

Resident intruder paradigm

Resident mice included male TMEM16B WT and KO mice. C57B6 male mice 16 weeks of age were purchased from Jackson Laboratories (https://www.jax.org/strain/000664) and served as intruder mice. All intruder mice were group housed 5 per cage and identified with ear punch(s). Resident mice were identified with a tattoo on their hindpaw toes.

All mice were brought to the testing room and allowed to acclimate 1 hour prior to testing. For three consecutive days, a novel intruder mouse was placed into the home cage (10" x 7" x 6.5") of the resident mouse for a maximum of 10 minutes. Each intruder mouse was tested only once per day and each resident mouse was introduced to a different intruder mouse each day. The cohort was split in half and tested over the span of two weeks. The resident-intruder social interaction was video recorded for later analysis. Videos were analyzed for the number and duration of "attacks" exhibited by the resident mouse. An "attack" was defined as any moment when a resident mouse was seen biting the intruder mouse. Any attack lasting 30

seconds or longer was immediately terminated and the remainder of the testing session for that resident was also terminated. For statistical analysis, resident mice that exhibited these types of prolonged "attacks" were given a maximum value equal to the 3rd Quartile + 1.5(Interquartile Range) for the calculated measurements of total time and numbers of attacks based on the genotype-specific population values. This equation was based on the assumption that these mice would be considered outliers in a normally distributed sample set.

Open field test

Mice were brought into the testing room to acclimate 1 hour prior to testing in normal light. Mice were placed in the middle of clear acrylic enclosures (41 x 41 x 30 cm) that were housed inside larger sound and light attenuating cubicles (Lafayette Instruments, Lafayette, IN). All mice were allowed to freely explore the enclosure for 15 minutes. The Flex-field/Open Field Photobeam Activity System (San Diego Instruments Inc., San Diego, CA) was used to track ambulatory and fine movements as well as rearing behavior using infrared photobeam arrays placed just outside the enclosure. The box was cleaned with 70% ethanol between mice.

Elevated plus maze test

Mice were brought into the testing room to acclimate in dim light 1 hour prior to testing. Mice were placed in the center of an elevated plus maze (Kinder Scientific Inc., Poway, CA) at the start of testing and allowed to freely explore the maze for 10 minutes. The elevated plus maze was situated 63 cm above the ground and was comprised of two "closed" arms (38 x 5 x 5 cm) with high walls (16.5 cm) and two "open" arms (38 x 5 x 5 cm) without any walls. The software

recorded time and distance traveled as well as the entries into each arm using infrared photobeam breaks. The maze was cleaned with 70% ethanol between mice.

Light-dark box test

Mice were brought into the testing room to acclimate 1 hour prior to testing in normal light. The light-dark box apparatus consisted of a clear acrylic enclosure (41 x 41 x 30 cm) that was divided into two equal halves by inserting a smaller dark box (20.5 x 20.5 x 30 cm) into one end of the enclosure (San Diego Instruments, San Diego, CA). The light-dark box enclosures were housed inside larger sound and light attenuating cubicles (Lafayette Instruments, Lafayette, IN). At the start of testing, mice were placed on the "light" side of the enclosure. Mice were allowed to freely explore both sides of the enclosure for 10 minutes. An archway opening at the bottom and middle of the dark box allowed mice to go between the "light" and "dark" sides of the enclosure. The Flex-Field/Open Field Photobeam Activity System recorded the movement and time spent in each side of the light-dark box with an infrared photobeam array placed just outside the enclosure. The chamber was cleaned with 70% ethanol between mice.

Direct social interaction test

Mice were transferred to the testing room 1 hour prior for acclimation. One experimental mouse and one social stimulus mouse were placed into a novel home cage (10" x 7" x 6.5") absent of any bedding and allowed to directly interact with one another for 10 minutes. C57B6 male mice 16 weeks of age from Jackson Laboratories (https://www.jax.org/strain/000664) were used as social stimulus mice. Stimulus mice were labeled on their back with an odorless marker to differentiate between the stimulus and experimental mice. Each stimulus mouse was used up

to three times per day, each time with a different experimental mouse. Interactions were video

recorded and analyzed by hand for the total amount of time mice spent directly interacting with

one another. Interactions included perioral contact, anogentical contact, rough play, etc... The

novel home cage was cleaned in between mice with 70% ethanol.

Two chamber social approach test

The two-chamber social approach test measures sociability by determining the amount of

time experimental mice spend and interact with a social stimulus mouse on the "social side"

versus the "non-social side" of the chamber. The test was conducted using white acrylic boxes

(24" x 16" x 8.75") that were placed inside larger light and sound attenuating cubicles (Lafayette

Instruments, Lafayette, IN). The boxes were split in half using a clear acrylic divider with an

archway opening in the bottom middle that allowed access between the two sides of the box. The

upper left and right corners of each chamber contained two small enclosures, one of which

housed the social stimulus mouse. C57B6 male mice 16 weeks of age from Jackson Laboratories

(https://www.jax.org/strain/000664) were used as the social stimulus mice.

Mice were transferred to the testing room 1 hour prior to start of testing. Prior to social

approach testing, the social stimulus mice were habituated to the enclosure space for two 15

minute sessions. Between sessions, the stimulus mice were returned to their home cage for an

approximately 20 minute intertribal interval. On the day of social approach testing, the

experimental mice first underwent a 10 minute habituation trial, where they were allowed to

freely explore the chambers and empty enclosures. Next, the experimental mouse was blocked

on the non-social side of the chamber while the social stimulus mouse was placed into the small

enclosure on the "social side". The social approach trial was then immediately conducted with

the experimental mouse again being allowed to freely explore the chambers and enclosures for an additional 10 minutes. Chambers were cleaned with 70% ethanol between each experimental mouse tested. All trials were video recorded with cameras mounted from above. Videos were later analyzed using CleverSys TopScan software (CleverSys Inc., Reston, VA) for the total number of bouts and time spent on the "social" and "non-social" sides of the chamber, and within a 2 cm "interaction" zone around the "social" and "non-social" enclosures.

Morris water maze cued platform training test

Mice underwent testing using the cued platform version of the Morris water maze task. The training was conducted using a pool (122 cm diameter, 50 cm high) filled with opaque water with the addition of white, non-toxic tempra paint in order to test visual procedural learning ability. The testing consisted of two phases: pretraining and cued platform testing. The pretraining phase took place on day 1 in which the mice learned to swim to a hidden platform submerged under the water in the middle of a rectangular training track (15 cm x 122 cm) that spanned the length of the pool. Once mice located the platform, they were allowed to remain there for 10 seconds before being removed by the experimenter. Mice that jumped off the platform were guided back by the experimenter's hand. Mice underwent ten consecutive trials, with each successive trial starting from the opposite end of the track during the pretraining phase.

Next, the cued platform training took place on days 2-4. During each trial, mice were placed into the pool facing the wall and allowed 60 seconds to find the cued platform, which was submerged 1.5 cm underwater but visually "cued" by the black and white striped mast (15 cm tall) placed in its center. Mice were allowed to remain on the cued platform for an additional 10-20 seconds before being removed from the pool. The drop location was consistent for all animals

but varied from trial to trial while the cued platform location was consistent for all mice but varied per session amongst the four different pool quadrants. Each testing session consisted of two trials, with a 15 minutes intertrial interval and two sessions were conducted each day with an approximately 3 hour intersession interval. All sessions were recorded and measurements were with EthoVision video tracking system (Noldus Information Technology, Lessburg, VA).

Visual placing response

The visual placing response of each mouse was determined by suspending them by the tail and lowering them toward a solid surface such as a countertop. If the mouse lifts its head and reached its forelimbs towards the object, it was considered to have a normal visual placing response.

STEREOTAXIC SURGERY

Mice were anesthetized with 2% vaporized isoflurane with O_2 and administered a mixture of ketamine (80-100 mg/kg) and xylazine (5-10 mg/kg) via intraperitoneal (IP) injection and subcutaneous (SC) injections of meloxicam (5-10 mg/kg), buprenorphine (0.05-01 mg/kg), and ampicillin (10-20 mg/kg). Mice were prepped for surgery by shaving and cleaning the head and skull with alcohol wipes and iodine. Surgeries were done using a Robot Stereotax (Neurostar Stereotaxic, Tubingen, Germany), Olympus SZ61 microscope, and a constant flow of 1% vaporized isoflurane with O_2. Mice were injected using a Hamilton syringe with 500 nl of AAV5-CAMKII-hChR2(H134R)-EYFP with titer $\geq 1\times10^{13}$ vg/mL (Penn Vector Core, Deisseroth Lab). Coordinates used for experiments include: CA3 region (-2.18 AP, -2.14 ML, 2.21 DV) and the LHA (-1.46 AP, -0.85 ML, 5.1 DV).

On Post-Surgical Day 1, mice were given SC injections of meloxicam (5-10 mg/kg) and ampicillin (10-20 mg/kg). Mice were also given SC injections of buprenorphine (0.05-01 mg/kg) if pain was observed. Mice were monitored four days post surgery and weight measurements were recorded. 17-21 days after surgery, mice were prepped for whole cell patch clamp physiology experiments according to the "acute slice preparation" section.

EXPERIMENTAL DESIGN AND STATISTICAL ANALYSIS

This study used TMEM16B WT and KO mice bred from the TMEM16B mCherry KO mouse line (Zhang et al., 2017). All data were analyzed using Graphpad Prism 6 and all values reported are Mean ± SEM. For electrophysiology data, a repeated measures two-way ANOVA statistical analysis with multiple comparisons was conducted for statistical analysis of EPSP, tail current, and spike firing data. The EPSP data site used a Tukey's multiple comparison test while the tail current and spike firing data utilized a Sidak's multiple comparison test with an alpha value of $p<0.05$. Multiple Student's t-test analysis was used for Input-Output curves generated from the LS neuron subpopulation dataset with an alpha value of $p<0.05$. For cell count data, the column statistics were calculated to determine the mean ± SEM of the percentage of double-labeled cells. For behavioral data, a repeated measures two-way ANOVA statistical analysis with Sidak's multiple comparisons test was conducted for the resident intruder paradigm and two-chamber social approach test. An alpha value of $p<0.05$ was used for detecting statistical significance. Student's t-test analysis or multiple Student's t-test analysis were conducted for Direct Social Interaction Test and Morris Water Maze cued platform training with an alpha value of $p<0.05$.

ACKNOWLEDGEMENTS

AUTHOR CONTRIBUTIONS

Lynn Wang, Jeffrey Simms, Christian J. Peters, Marena Tynan-La Fontaine, Kexin Li, T. Michael Gill, Yuh Nung Jan, and Lily Yeh Jan contributed to this work. L.W., C.J.P., J.S., T.M.G., and L.Y.J. conceived and designed experiments. L.W., J.S., and M.T.L.F. performed experiments. L.W., C.J.P., and L.Y.J. contributed to writing of this study. All authors reviewed the manuscript.
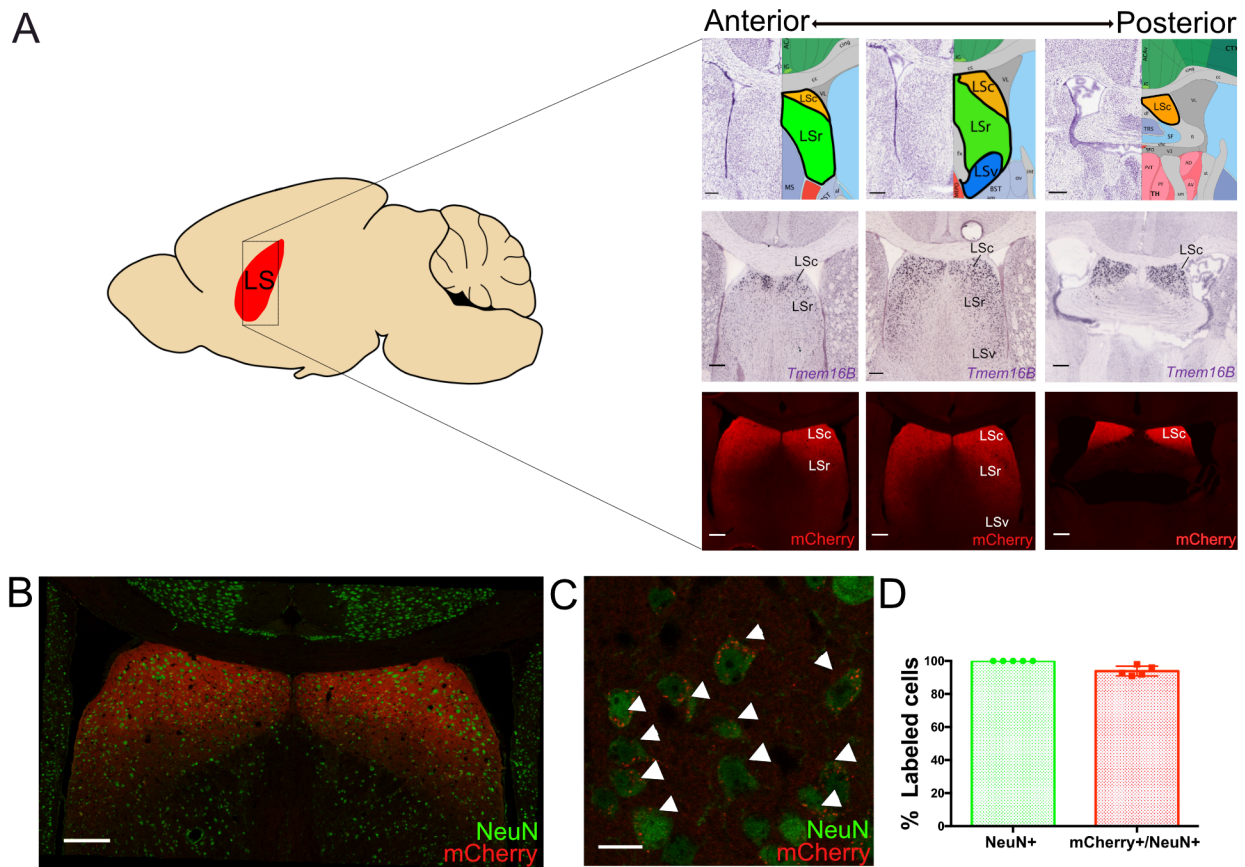
Figure 2.1. TMEM16B is expressed in lateral septum neurons.
A, Schematic of sagittal mouse section with location of LS (left), with depiction of LS subregion locations (top), TMEM16B mRNA (middle), and TMEM16B protein (bottom) expression from the anterior to posterior end of the LS. LS subregion images and *in situ* hybridization images of TMEM16B (gene name: *Ano2*) in WT mice are modified from the Allen Brain Reference Atlas and Allen Brain ISH database (experiment# 71587834) respectively. Fluorescence images are from TMEM16B knockout mice with a simultaneous in-frame knock in of a farnesylated mCherry marker. LS subregions include caudal LS (LSc), rostral LS (LSr), and ventral LS (LSv). Scale bars: 200 μm. Sagittal mouse brain diagram credit: Jonas Töle, Creative Commons License. *B*, Fluorescent double labeling for NeuN and mCherry in TMEM16B KO LS sections shows mCherry expression along the membrane of TMEM16B expressing neurons. Tile scan 20x image with stitching. Scale bar: 200 μm. *C*, 63x IHC image for NeuN and mCherry shows overlapping expression (arrowheads) of mCherry in NeuN+ cells. Scale bar: 15 μm.
D, Quantification of mCherry+/NeuN+ cells indicates most LS neurons express mCherry. Mean ± SEM: 93.91% ± 1.326%, *n* = 5.
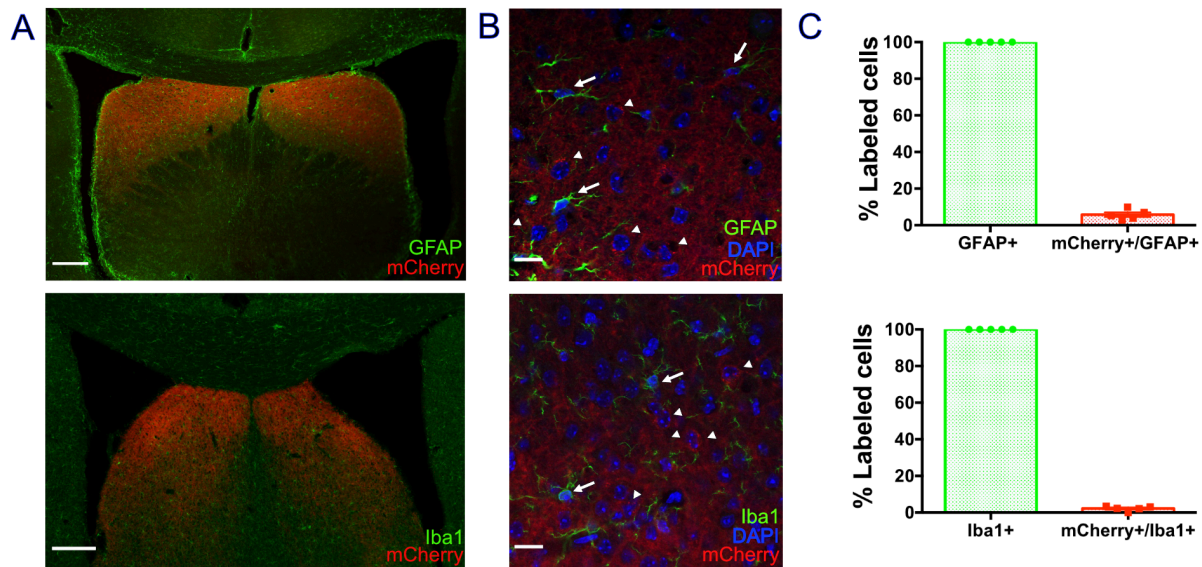
Figure 2.2. No TMEM16B expression in non-neuronal cells of the lateral septum.
A, Representative images of TMEM16B KO coronal sections with fluorescence labeling of (top) astrocyte marker, GFAP, and mCherry and (bottom) microglia marker, Iba1, and mCherry in the LS. Tile scan images 10x with stitching, scale bar 200 μm. *B*, Representative 63x images; arrowheads point to mCherry+, DAPI+, GFAP- cells (top) or mCherry+, DAPI+, Iba1- cells (bottom); arrows point to mCherry-, DAPI+, GFAP+ cells (top) or mCherry-, DAPI+, Iba1+ cells (bottom); scale bar 15 μm. DAPI staining was used to identify cell bodies of GFAP+ and Iba1+ cells. *C*, Quantification of mCherry+/GFAP+ cells (top; Mean ± SEM: 5.781% ± 1.239%; *n*=5) and mCherry+/Iba1+ cells (bottom; Mean ± SEM: 2.172% ± 0.596%; *n*=5) indicates LS astrocytes and microglia do not express mCherry.

Figure 2.3. LS neurons with TMEM16B expression project to the ventral lateral septum and lateral hypothalamic regions. TMEM16B-expressing LS neurons project to lateral preoptic area (LPO) and lateral hypothalamic area (LHA). *A*, Modified Allen Brain Reference

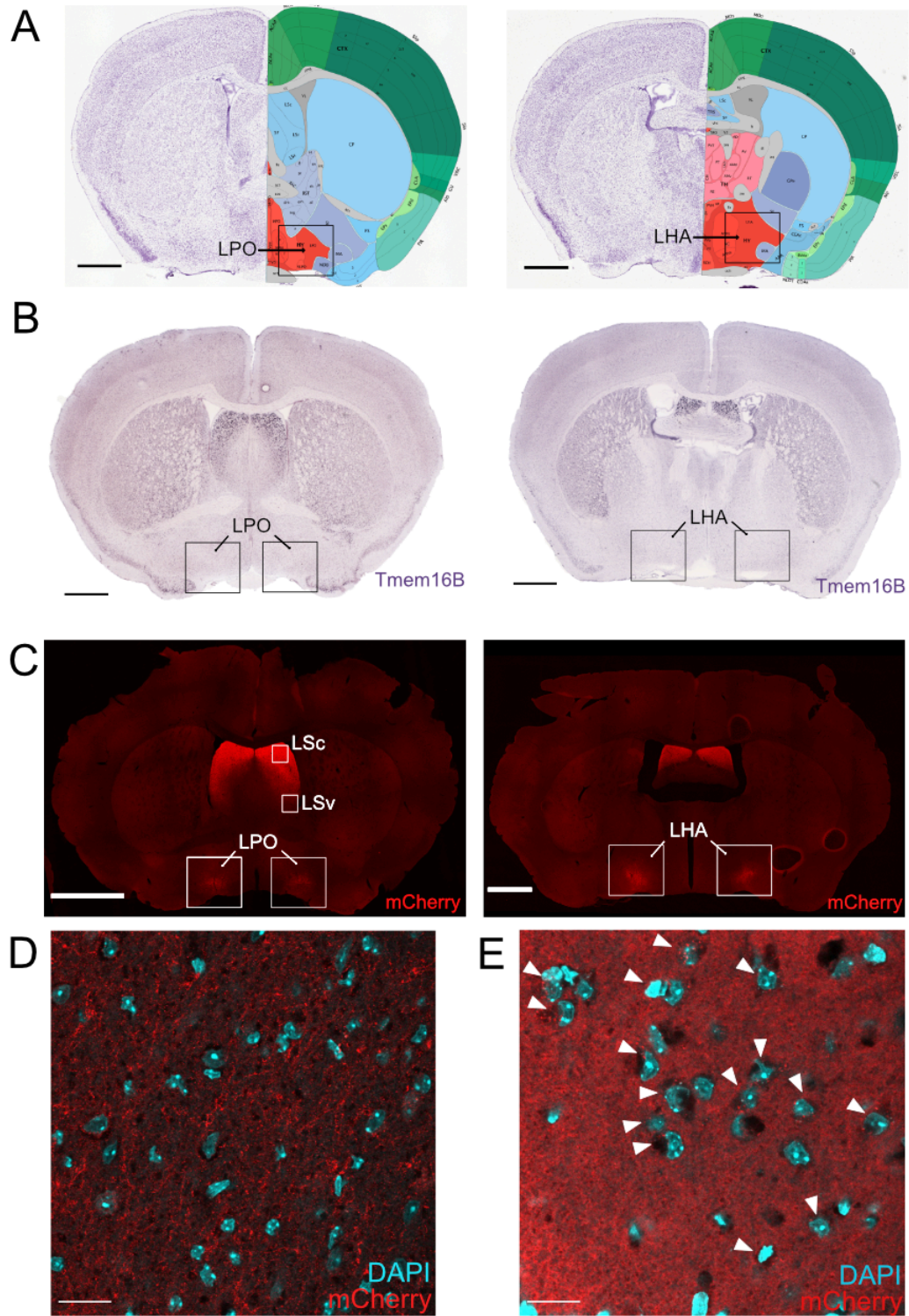Atlas images with locations of LPO (top) and LHA (bottom) delineated by black border. ***B***, Modified Allen Brain ISH images for TMEM16B mRNA (gene name: *Ano2*) (experiment# 71587834) (right). Black border delineates absence of TMEM16B mRNA expression in LPO (top) and LHA (bottom), suggesting that mCherry expression are from LS nerve fibers projecting to these hypothalamic regions. Arrows point to the specific brain region. ***C***, mCherry fluorescence images in coronal section of TMEM16B KO mouse brain, large white border delineates location of mCherry axon fibers in LPO (top) and LHA (bottom). Small white borders delineate the caudal LS (LSc), which is part of the dorsal regions of the LS, and the ventral LS (LSv). Arrows point to the specific brain region. ***D,*** 63x magnification image of the LSv with DAPI and mCherry labeling. mCherry labels the nerve fibers in the LSv but not the cell membranes surrounding DAPI-labeled cell bodies. ***E.*** 63x magnification image of the LSc with DAPI and mCherry labeling. mCherry puncta localized to the cell membranes surrounding DAPI-labeled cell bodies (see arrowheads). Scale bar for 63x images: 20 μm. Scale bars for all coronal section images: 1000 μm.
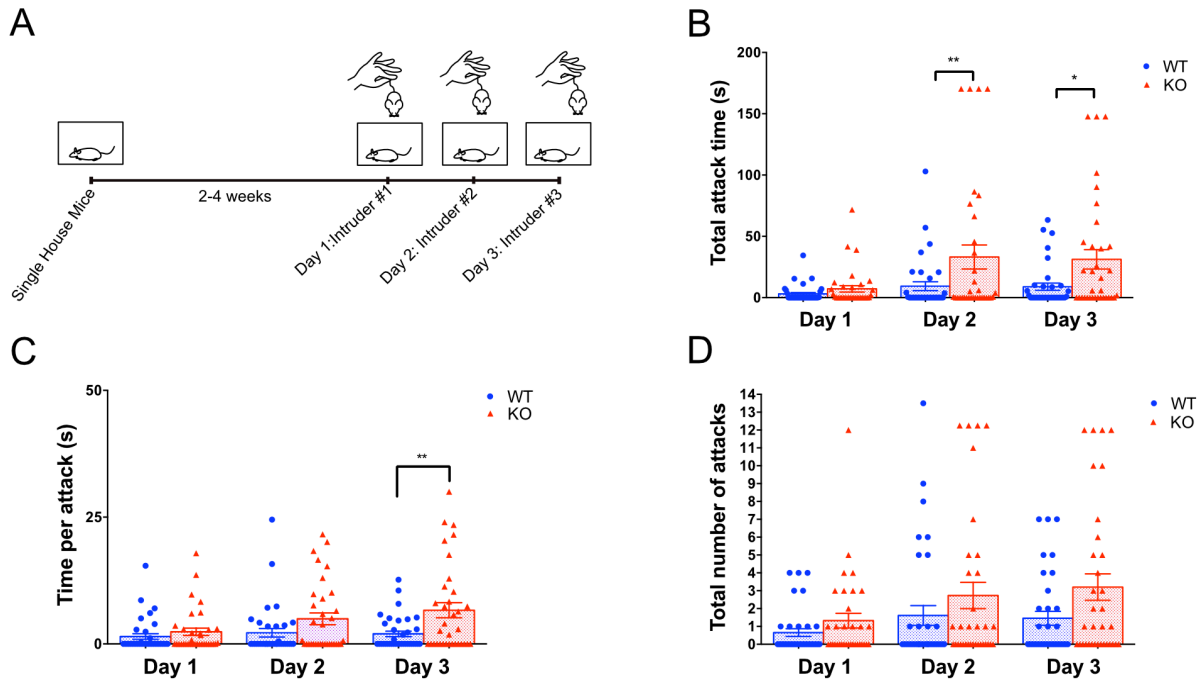
Figure 2.4. TMEM16B KO mice display longer bouts of aggression compared to WT littermates. *A*, Experimental timeline for resident-intruder paradigm. Experimental mice were introduced to a new intruder mouse each day of testing. *B*, TMEM16B KO mice display increased total attack time compared to WT littermates on day 2, ($p = 0.0081$) and day 3 ($p = 0.0141$). 2-way ANOVA with Sidak's multiple comparisons. *C*, TMEM16B KO mice display increased time per attack compared to WT littermates on Day 3 ($p = 0.0015$). 2-way ANOVA with Sidak's multiple comparisons; mean ± SEM. *D*, TMEM16B KO mice do not show significant difference in total number of attacks compared to WT littermates. 2-way ANOVA with Sidak's multiple comparisons. Sample size: WT $n = 35$, KO $n = 34$. Error bars show the SEM.
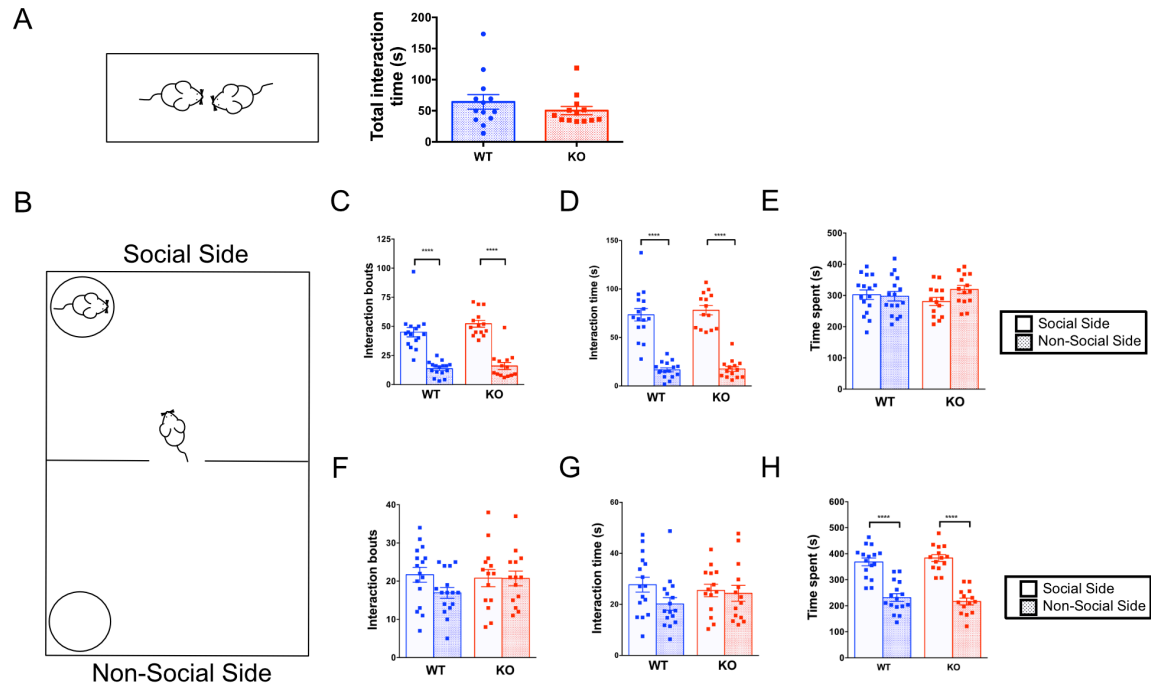
Figure 2.5. TMEM16B KO mice show no difference in sociability compared to WT littermates. *A*, No significant difference detected during Direct social interaction test between TMEM16B KO and WT littermates. Student's t-test conducted, $p = 0.3102$. Sample size: WT $n = 13$, KO $n = 13$. *B*, Schematic of Two chamber social approach test. *C-E*, Habituation Trial: both TMEM16B WT and KO mice show no preference for either side in terms of interaction bouts (*C*), interaction time (*D*), or side time (*E*). 2-way ANOVA with Sidak's multiple comparisons. Sample size: WT $n = 16$, KO $n = 14$. *F-H*, Social Trial: Both TMEM16B WT and KO mice show a significant preference for the social side of the chamber in terms of interaction bouts (*F*; $p < 0.0001$), interaction time (*G*; $p < 0.0001$), and side time (*H*; $p < 0.0001$). 2-way ANOVA analysis with Sidak's multiple comparisons. Sample size: WT $n = 16$, KO $n = 14$. Error bars show the SEM.
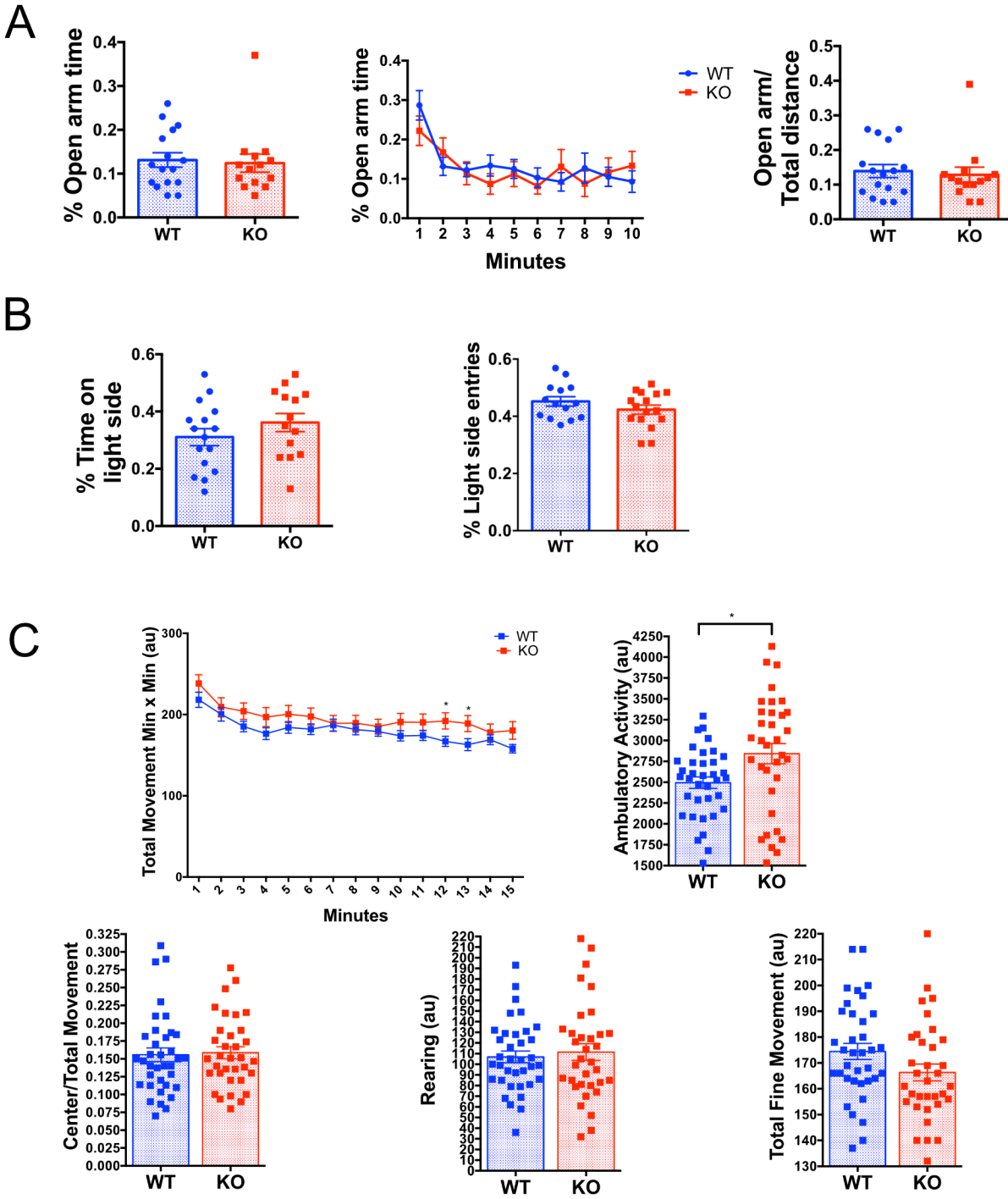
Figure 2.6. Comparison of TMEM16B WT and KO during anxiety-related behavioral tests.
A, All TMEM16B KO mice and WT littermates underwent the Open Field test. TMEM16B KO mice show increased total movement ($p = 0.0166$) and ambulatory activity ($p = 0.0156$) compared to WT. No significant differences detected in total fine movement, center/total movement, and rearing. Student's t-test conducted, sample size WT $n = 36$, KO $n = 34$. Units

are "arbitrary units" (au), determined by the software as number of infrared beam breaks. ***B-C***, Subset of TMEM16B WT and KO mice underwent Elevated Plus Maze (EPM) and Light Dark Box (LD). ***B***, No significant difference detected between TMEM16B KO and WT in % time spent in the EPM open arm and the fraction of distance traversed in the open arm compared to the total distance. Student's t-test, $p > 0.05$. ***C***, No significant difference detected between TMEM16B KO and WT in % time spent on the light side during LD and the proportion of entries into the light side. Student's t-test, $p > 0.05$. Sample size: WT $n = 16$, KO $n = 14$. All error bars show the SEM.
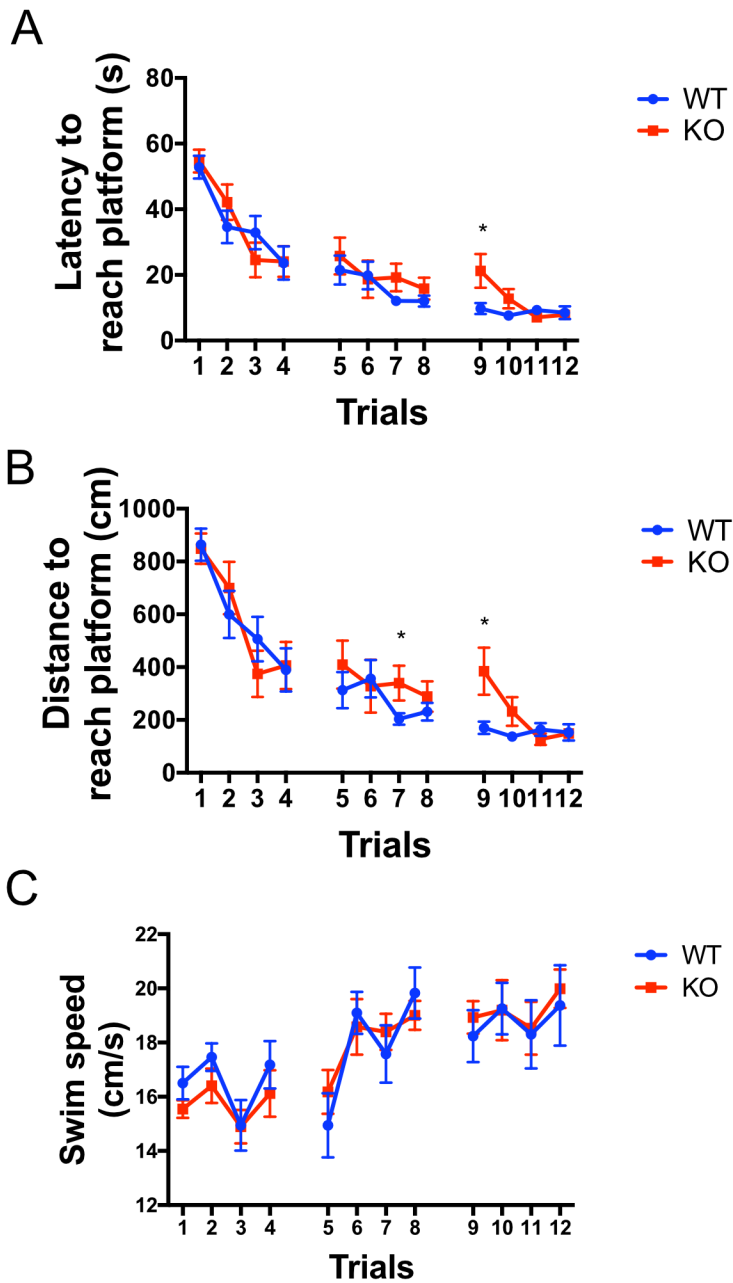
Figure 2.7. TMEM16B KO mice show normal visual function.
TMEM16B WT and KO littermates were assessed for latency to reach platform (*A*), distance traveled to reach platform (*B*), and swim speed (*C*) in the Morris Water Maze (MWM) Visual Cue Learning Test.. *A*, No significant difference in latency to reach platform seen between TMEM16B KO mice and WT controls for most trials, except trial 9 ($p = 0.0286$). *B*, No significant difference in distance traveled to reach platform, except trials 7 ($p = 0.0428$) and 9 ($p = 0.0177$). *C*, No significant difference in swim speed. Multiple Student's t-test analysis. Sample size: WT $n = 16$, KO $n = 13$.
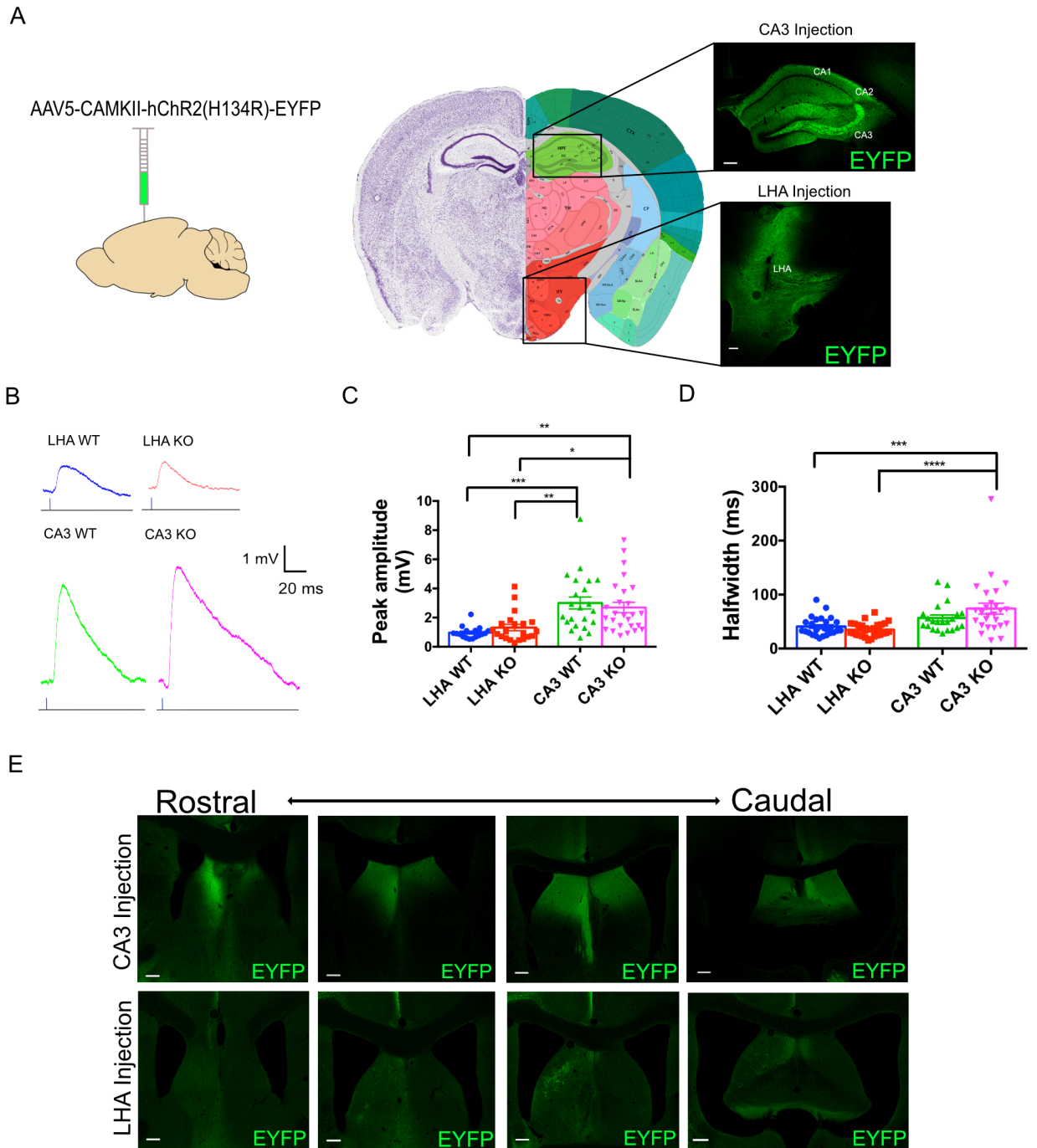
Figure 2.8. Major excitatory synaptic inputs to the lateral septum are maintained in TMEM16B KO mice.

A, AAV5-CamKII-hChR2(H134R)-EYFP was stereotaxically injected into two major excitatory LS input regions: CA3 region of the hippocampus and the lateral hypothalamic area (LHA). Coronal image modified from Allen Brain Reference Atlas. Scale bars: 200 μm. *B*,

Representative traces of evoked EPSP responses from optogenetic stimulation of ChR2 in the LS. 1 ms pulse of blue light was flashed onto LS neurons. *C*, TMEM16B KO mice show no difference in evoked EPSP amplitude compared to WT, regardless of input region. CA3 evoked EPSPS show higher amplitude compared to LHA evoked EPSPs. 2-way ANOVA analysis with Tukey's multiple comparisons. $*p < 0.05$, $**p < 0.01$, $***p < 0.001$. Sample size: LHA WT $n = 27$, LHA KO $n = 29$, CA3 WT $n = 22$, CA3 KO $n = 26$. Error bars show the SEM. *D*, TMEM16B KO mice show no difference in evoked EPSP halfwidth compared to WT, regardless of input region. However, CA3 evoked EPSPs display longer halfwidths in TMEM16B KO compared to LHA evoked EPSPs in TMEM16B WT ($p = 0.0008$) and KO ($p < 0.0001$) mice. 2-way ANOVA analysis with Tukey's multiple comparisons. Sample size: LHA WT $n = 27$, LHA KO $n = 29$, CA3 WT $n = 22$, CA3 KO $n = 26$. Error bars show the SEM. *E*, Histological images of fixed LS coronal sections following unilateral AAV injection show expression of ChR2-EFYP in CA3 and LHA from the rostral to caudal end of the LS. Scale bars: 200 μm.
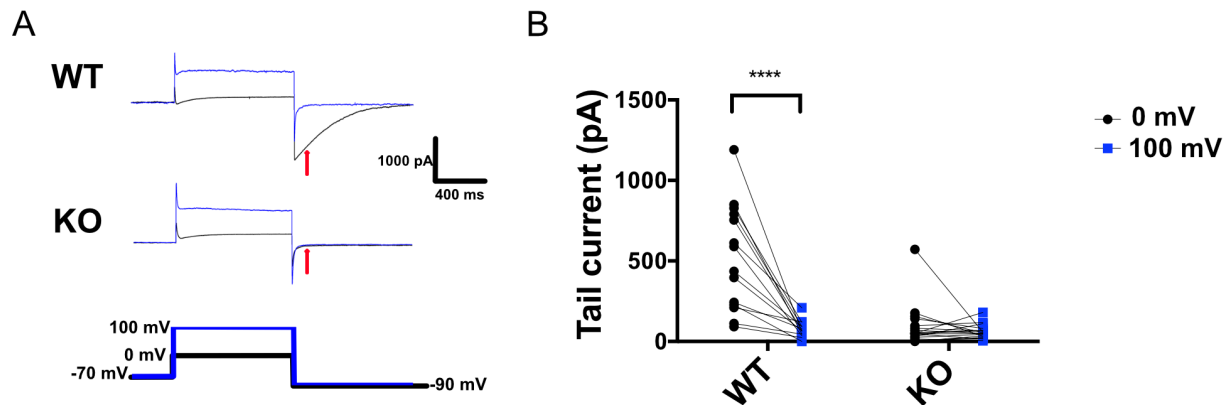
Figure 2.9. TMEM16B KO mice show loss of calcium-activated chloride current.
A, Representative traces of Cl⁻ tail currents in WT and TMEM16B KO LS neurons. Whole cell recordings were performed in voltage clamp mode and tail currents were measured 100 ms following a pulse to -90 mV (red arrow). Black traces represent pulses given from -70 mV to 0 mv, blue traces represent pulses given from -70 to 100 mV. *B*, WT LS neurons display a tail current at -90 mV following an activating pulse to 0 mV that is significantly smaller when the neuron is activated to 100 mV instead ($p < 0.0001$). TMEM16B KO LS neurons exhibit reduced tail current amplitudes following a 0 mV activating pulse that are not significantly affected by pre-activation at 100 mV ($p = 0.8273$). 2-way ANOVA with Sidak's multiple comparisons. Sample size: WT $n = 14$, KO $n = 18$. All error bars show the SEM.
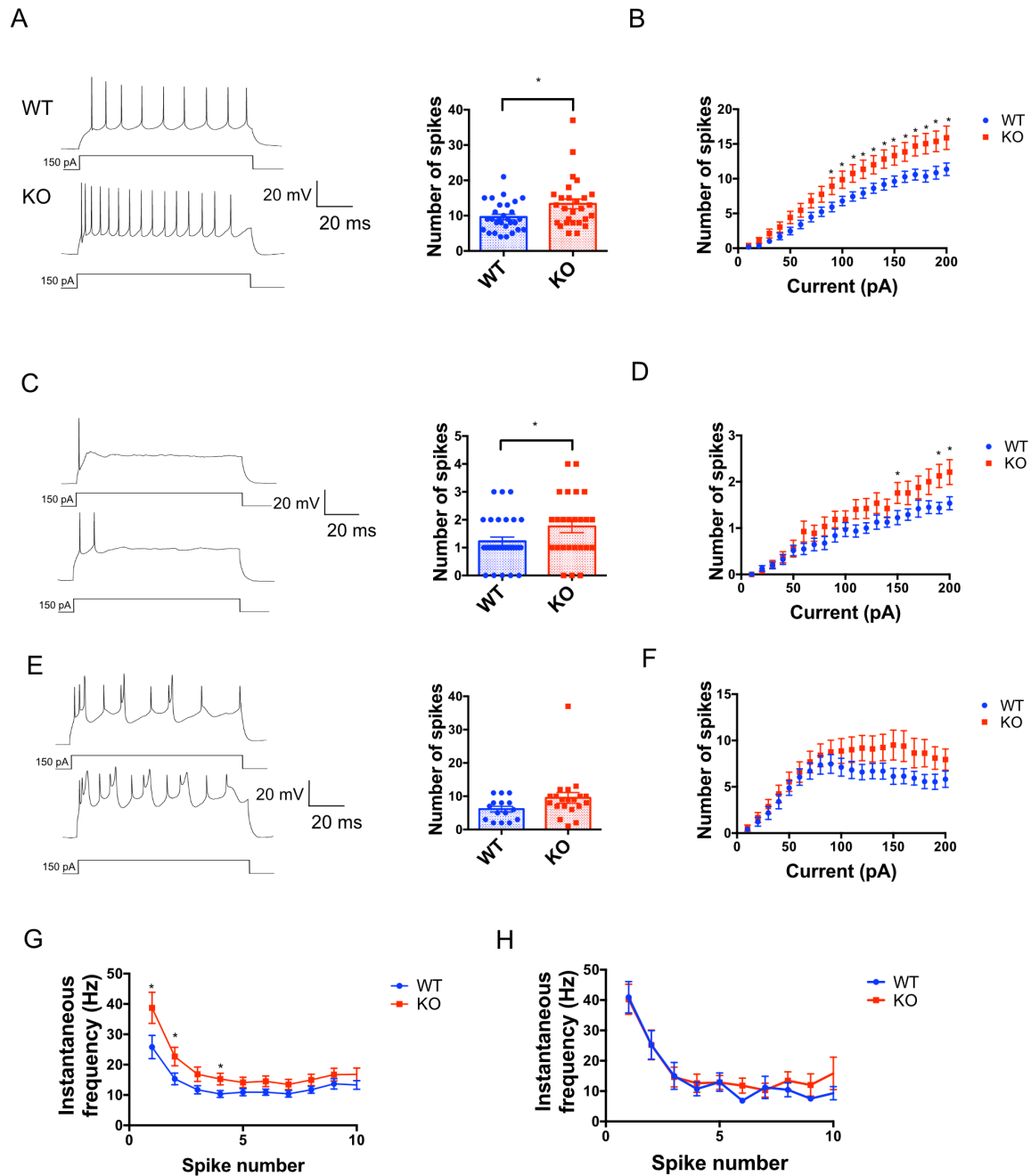
Figure 2.10. TMEM16B regulates action potential firing in LS neurons. Representative traces of three distinct firing behaviors, denoted "tonic cells" (*A*), "phasic cells" (*C*), and "burst cells" (*E*) are shown during 150 pA current injections. *A*, TMEM16B KO tonic cells show

significant increase in spike number compared to WT at 150 pA ($p = 0.0197$). Student's t-test. **B**, Input-output curve of mean spike number in tonic cells with varying amounts of current injection. TMEM16B KO tonic cells show significant increase in spike number compared to WT with current injections ≥90 pA. Multiple Student's t-test, $p < 0.05$ for current injections from 90 pA to 200 pA. **C**, TMEM16B KO phasic cells show significant increase in spike number compared to WT at 150 pA ($p = 0.0478$). Student's t-test. **D**, Input-output curve of mean spike number in phasic cells with varying current injection amounts. TMEM16B KO phasic cells show significant increase in spike number compared to WT with current injections of ≥150 pA. Multiple Student's t-test, $p < 0.05$ for current injections of 150 pA, 190 pA, and 200 pA. **E**, TMEM16B KO burst cells show no significant difference in spike number compared to WT at 150 pA ($p = 0.1037$). Student's t-test. **F**, Input-output curve of mean spike number in burst cells with varying amounts of current injection. TMEM16B KO burst cells show no significant difference in spike number compared to WT. Multiple Student's t-test conducted, $p > 0.05$. **G-H**, Instantaneous frequency for tonic and burst cells calculated at 150 pA current injection. TMEM16B KO tonic cells show increased instantaneous frequency at the first ($p = 0.0468$), second ($p = 0.0408$), and fourth ($p = 0.0307$) spikes fired compared to WT. Multiple Student's t-test. TMEM16B KO burst cells show no significant difference in instantaneous frequency compared to WT. Multiple Student's t-test, $p > 0.05$. Sample size: tonic cells WT $n = 29$, KO $n = 28$; phasic cells WT $n = 32$, KO $n = 37$; burst cells WT $n = 17$ KO $n = 22$. Error bars show the SEM.

Table 2.1. Statistical analysis for anxiety related behavioral tests.
The *p* values for Multiple Student's t-test analysis of total movement during the open field test and elevated plus maze (EPM) % open arm time. Asterisks denote significance.

Open Field Total Movement Analysis		EPM % Open Arm Time Analysis	
Minute	P-value	Minute	P-value
1	0.163655	1	0.232254
2	0.521693	2	0.413838
3	0.116607	3	0.803273
4	0.13791	4	0.225041
5	0.203352	5	0.747015
6	0.199521	6	0.511086
7	0.86201	7	0.431376
8	0.492491	8	0.439873
9	0.551073	9	0.777845
10	0.163465	10	0.375252
11	0.17845		
12*	0.0335608		
13*	0.0366699		
14	0.455168		
15	0.0618719		

Table 2.2. Statistical analysis for Morris Water Maze visual cue test. The *p* values for Multiple Student's t-test analysis of measurements made during the Morris Water Maze visual cue test, including latency, distance, and swim speed. Asterisks denote significance.

Latency		Distance		Swim Speed	
Trial	P-value	Trial	P-value	Trial	P-value
1	0.707858	1	0.866146	1	0.204474
2	0.317528	2	0.460162	2	0.200265
3	0.269249	3	0.293357	3	0.96448
4	0.942984	4	0.89208	4	0.406821
5	0.54492	5	0.392889	5	0.42009
6	0.86965	6	0.817209	6	0.684543
7	0.0940686	7*	0.0428105	7	0.543795
8	0.299984	8	0.370813	8	0.482329
9*	0.028603	9*	0.0177375	9	0.566761
10	0.0812904	10	0.0702795	10	0.966371
11	0.251495	11	0.282269	11	0.893004
12	0.766386	12	0.908166	12	0.730769

Table 2.3. Multiple Student's t-test analysis of spike numbers for LS neurons.

Tonic Cells		Phasic Cells		Burst Cells	
Current (pA)	P-value	Current (pA)	P-value	Current (pA)	P-value
10	0.326316			10	0.753898
20	0.136209	20	0.501596	20	0.551474
30	0.133778	30	0.792451	30	0.5241
40	0.124442	40	0.768352	40	0.524635
50	0.0633547	50	0.84916	50	0.632056
60	0.0823391	60	0.132884	60	0.721776
70	0.0605713	70	0.264344	70	0.527415
80	0.0629321	80	0.144574	80	0.524173
90*	0.0331175	90	0.126257	90	0.448703
100*	0.0313988	100	0.360978	100	0.326154
110*	0.025	110	0.0538242	110	0.226357
120*	0.0265525	120	0.0752733	120	0.138915
130*	0.0275906	130	0.125782	130	0.189543
140*	0.0219545	140	0.187951	140	0.166013
150*	0.0197438	150*	0.0477679	150	0.103679
160*	0.0248827	160	0.0832959	160	0.13429
170*	0.0133304	170	0.133099	170	0.1858
180*	0.0064734	180	0.0656934	180	0.107527
190*	0.0116971	190*	0.0112352	190	0.12456
200*	0.0205249	200*	0.0252302	200	0.198944

Table 2.4. Statistical analysis of instantaneous frequency for LS subpopulations of neurons.
The *p* values for Multiple Student's t-test analysis of instantaneous frequency at specific spikes fired during the current injection for tonic cells and burst cells. Asterisks denote significance.

Tonic cells		Burst cells	
Spike Number	P- value	Spike Number	P- value
1*	0.0467645	1	0.930386
2*	0.0407847	2	0.999246
3	0.0606201	3	0.947354
4*	0.0307293	4	0.681213
5	0.129868	5	0.973329
6	0.0919546	6	0.244878
7	0.138767	7	0.841689
8	0.154045	8	0.602018
9	0.309136	9	0.486127
10	0.232467	10	0.404894

CHAPTER 3: STUDIES CONCERNING TMEM16B FUNCTION IN THE HIPPOCAMPUS-SEPTUM PATHWAY

INTRODUCTION

The calcium-activated chloride channel (CaCC), Transmembrane protein of unknown function 16B (TMEM16B), plays an important role in regulating neuronal signaling throughout the central nervous system (Stöhr et al., 2009; Huang et al., 2012b; Ha et al., 2016; Pietra et al., 2016; Zhang et al., 2017) and behavior (Ha et al., 2016; Pietra et al., 2016; Zhang et al., 2017). In Chapter 2, we discussed the characterization of TMEM16B function in the lateral septum (LS), a brain region implicated in emotional and mood-related behaviors, and how CaCC regulation of LS spike frequency correlates with male mice aggression. In this chapter, we will continue exploring the function of TMEM16B in the dendritic region of LS neurons and the role of CaCC at the synapse of hippocampal axon terminals and septal neurons.

The lateral septum receives major innervation from the hippocampus organized in a topographical manner (Risold and Swanson, 1997a). In particular, the CA3 region of the hippocampus innervates the caudal subregion of the LS (LSc). This pathway is part of the neural circuit responsible for the generation of hippocampal theta oscillations, a brain wave activity implicated in learning and memory (Buzsáki and Moser, 2013). While much work has been done to understand the neural circuitry of theta rhythm generation (Rawlins et al., 1979; King et al., 1998), the contribution of ion channels to theta oscillation remains a work in progress (Buzsáki, 2002). Ion channels regulate both the postsynaptic potentials and membrane potentials of neurons, and thus can contribute to the local field potentials of a brain region. For example, the

activity of voltage-gated sodium channels in entorhinal cortex neurons are known to regulate theta rhythms (Alonso and Llinas, 1989).

TMEM16B is important for regulating neuronal signaling in brain regions involved in the neural circuit of hippocampal theta oscillations, including the hippocampus, where it regulates action potential duration and EPSP amplitude (Huang et al., 2012b), and the lateral septum (see Chapter 2), where it regulates action potential frequency and spike frequency adaptation. A better understanding of TMEM16B function at the synapse between hippocampal and septal neurons can elucidate how CaCCs contribute to the regulation of an important synaptic connection in the theta oscillation circuit and how CaCC function could affect theta generation and associated behaviors.

In this study, we investigated the function of TMEM16B in the dendritic region of LS neurons, and found no detectable role of TMEM16B in the regulation of excitatory post-synaptic potentials (EPSPs) and excitatory post-synaptic currents (EPSCs). We next explored TMEM16B contribution to pre-synaptic hippocampal axon terminals at the synapse onto septal neurons, and found TMEM16B regulation of neurotransmitter release from the CA3 axon terminal. Finally, we showed that the number of synaptic connections formed between CA3 axons and LS dendrites is unaffected by loss of TMEM16B. In conclusion, these results suggest that TMEM16B functions only at the pre-synaptic side of the hippocampal-septal synapse.

RESULTS

Loss of TMEM16B function does not affect spontaneous or evoked excitatory post-synaptic activity

In the hippocampus, TMEM16B functions within close proximity of NMDA receptors to regulate excitatory post-synaptic amplitude of CA1 neurons (Huang et al., 2012b). Given the precedence set for TMEM16B function at the post-synaptic side, we recorded spontaneous EPSC activity in TMEM16B WT and KO LS neurons and looked for differences in EPSC peak amplitude and halfwidth (Fig. 3.1*A-B*). Our results show no significant differences in spontaneous EPSC frequency between TMEM16B KO and WT LS neurons (Fig. 3.1*A*; p=8041, Student's t-test). In addition, we observed no difference in mean EPSC peak amplitude (Fig. 3.1*B*, middle; p=0.2877, Student's t-test) or mean EPSC halfwidth (Fig. 3.1*B*, right; p=0.2796, Student's t-test). We also saw no difference in the frequency distribution for EPSC peak amplitude values between TMEM16B WT and KO LS neurons (Fig 3.1*C*, left). We observed a slight shift in the frequency distribution for EPSC halfwidth values, with significance detected for EPSC halfwidth durations of 18 ms (p=0.0363), and 24-28 ms (p=0.0241, p=0.0212, p=0.0300) (Fig. 3.1*C*, right; multiple Student's t-test). These results suggest that there may be slight increase in duration of EPSCs in TMEM16B KO LS neurons compared to WT. However, the effect does not appear systematic at all higher halfwidth values, and the mean EPSC halfwidths do not provide supporting evidence. Moreover, optogenetic stimulation of LS neurons in TMEM16B WT and KO brain slices do not show any differences in evoked EPSP amplitude or halfwidth (see Chapter 2).

Since TMEM16B is activated by calcium, we performed an additional experiment to maximize the amount of calcium influx through repeated stimulation of the cell. We recorded EPSP temporal summation from TMEM16B WT and KO LS neurons (Fig. 3.1*D*). Neurons were stimulated using optogenetic activation of channelrhodopsin that was introduced via an AAV5-CAMKII-ChR2-EYFP virus injected stereotactically into the CA3 region of TMEM16B WT and KO mice 17-21 days prior to recording. Our results show no significant differences in mean EPSP peak amplitude for each consecutive EPSP recorded during the summation (Fig. 3.1*D*, bottom left, Multiple Student's t-test, $p>0.05$ for all comparisons) and no significant differences in the ratio of EPSPs (Fig. 3.1*D*, bottom right, Multiple Student's t-test, $p>0.05$ for all comparisons). Overall, these results suggest that even with an increase in calcium influx through temporal summation there was no significant differences in excitatory post-synaptic activity in TMEM16B KO LS neurons compared to WT LS neurons. In summary, TMEM16B function does not contribute to regulation of excitatory post-synaptic potentials in the dendritic region of LS neurons.

Loss of TMEM16B function detected at the pre-synaptic hippocampal axon terminal of the synapse on septal neurons

We investigated miniature EPSC (mEPSC) activity at the hippocampal-septal synapse to look for differences in single vesicle release between TMEM16B WT and KO LS neurons (Fig. 3.2). Previous studies suggest that TMEM16B is also expressed in hippocampal neurons (Huang et al., 2012b), however currently no evidence supports a role for TMEM16B function at the axon terminals.

To detect mEPSCs, whole-cell voltage clamp recordings were performed with 100 μM PTX and 1 μM TTX in the ACSF bath solution. Our results indicate that TMEM16B KO LS neurons show significant increases in mEPSC frequency compared to TMEM16B WT LS neurons (Fig. 3.2*A*; *p=0.0245*, Student's t-test). However, we see no significant difference in mEPSC peak amplitude (Fig. 3.2*B; p=0.2377*, Student's t-test) or mEPSC halfwidth (Fig. 3.2*C; p=0.4902*, Student's t-test), with respect to the frequency distributions or mean values. In summary, our results suggest that TMEM16B functions in the axon terminals of presynaptic neurons that innervate the LS to regulate the frequency of spontaneous glutamate release. Since the LS receives major excitatory input from the hippocampus, it is likely that most of the mEPSCs we observed are due to glutamate release from hippocampal pyramidal neurons.

Next, we investigated the paired pulse ratio in TMEM16B KO compared to WT LS neurons since paired pulse ratios are another determinant of pre-synaptic function (Debanne et al., 1996). By optogenetically stimulating two major LS input regions, the LHA and hippocampal CA3 region, we observe no paired pulse facilitation (PPF) or paired pulse depression (PPD) with LHA innervation, but we see an increase in PPF with CA3 innervation in mice lacking TMEM16B (Fig. 3.2*D*; Student's t-test; LHA WT vs KO: *p=0.4405*, WT *n=14*, KO *n=13*; CA3 WT vs KO: *p=0.0029*, WT *n=21*, KO *n=25*). These results suggest that TMEM16B function in CA3 axon terminals may regulate transmitter release.

In summary, the results from these sets of experiments suggest that TMEM16B function in CA3 axon terminals regulates both spontaneous quantal release and evoked neurotransmitter release.

Loss of TMEM16B expression does not affect synapse number at the hippocampal-septal synapse

To determine if differences seen in excitatory post-synaptic activity in TMEM16B KO mice were due to lack of channel function or changes in development due to TMEM16B deletion, we quantified the number of synapses in TMEM16B KO mice and WT littermates (Fig. 3.3). Based on high TMEM16B expression we observed in the LSc (see Chapter 2), we chose to target major LSc afferents, including the CA3 region of the hippocampus and the LHA. We injected the retrograde neuronal tracer, Cholera Toxin Subunit B (CTB) conjugated to Alexafluor 488, into the LSc (Fig. 3.3*A*) and observed no CTB expression in the LHA, but high CTB expression in CA3 (Fig. 3.3*B*). Based on these observations, we chose to continue investigating the synapse quantity at the CA3-LSc synapse. We observed CTB labeling of CA3 neurons along the anterior to posterior axis of the hippocampus (Fig. 3.3*C*). We counted the number of CTB+ cells in CA3 and found no significant difference in CTB+ cells between TMEM16B WT neurons, with a count of 1385±276 (mean ± SEM) CTB+ cells, and KO neurons, with a count of 970±142 (mean ± SEM) CTB+ cells (Fig. 3.3*D;* Student's t test, p=0.1795, WT n=4, KO n=6). Based on these results, we conclude that differences seen in mini EPSC frequency and paired pulse facilitation are due to TMEM16B function rather than altered innervation of LSc neurons by CA3 pyramidal projections.

DISCUSSION

In this study, we investigate the function of TMEM16B in the dendritic region of LS neurons. Unlike TMEM16B function in hippocampal neurons, TMEM16B function in LS neurons does not affect their evoked excitatory postsynaptic potentials. Surprisingly, we identify

TMEM16B function in the axon terminals of CA3 pyramidal neurons; loss of TMEM16B leads to increased paired pulse facilitation and increased miniature EPSC frequency, suggesting that TMEM16B contributes to the regulation of neurotransmitter release at the hippocampal-septal synapse. Finally, we also demonstrate that changes seen in pre-synaptic function at the hippocampal-septal synapse are not due to a change in the number of these synapses in TMEM16B mutants.

The findings from this study provide further insight into TMEM16B function at the axon terminals of CA3 hippocampal neurons. In a previous study, it was reported that TMEM16B function did not contribute to neurotransmitter release of CA3 neurons at the Schaffer collateral, based on a pharmacological approach to inhibit TMEM16B function with niflumic acid in wildtype mice at the Schaffer collateral (Huang et al., 2012b). In our study, we investigated the CA3-LS synapse using the recently generated TMEM16B knockout mouse model (Zhang et al., 2017) and detected alterations of spontaneous and evoked excitatory postsynaptic potentials. The possibility that TMEM16B could selectively affect transmitter release from a specific subset of CA3 axon terminals remains intriguing, and recent evidence investigating the function of CA2 pyramidal neurons at the axon terminal suggest that activation of the arginine vasopressin receptor 1b (AVPR1b) at the CA2-dLS synapse increases postsynaptic potentials, but no effect is seen on postsynaptic potentials at the CA2-CA1 synapse (Leroy et al., 2018). Thus, there appears to be some evidence suggesting that transmitter release might be selectively affected based on the axon terminals destination of innervation. However, in the context of the results concerning TMEM16B function, it is more likely this discrepancy reflects differences in experimental approach and the limitations of using a non-specific pharmacological blocker for TMEM16B.

Future directions include looking for changes in hippocampal theta oscillations in

TMEM16B KO mice compared to WT littermates. It would be interesting to see if the physiological changes we observe in the LS and hippocampus correlate with changes in theta oscillations. Moreover, it would be interesting to see how changes in theta oscillations in TMEM16B KO mice correlate with any phenotypic differences in behaviors associated with hippocampal theta, such as learning and memory and spatial navigation. In conclusion, our work investigating TMEM16B function at the hippocampal-septal synapse provides further insight into CaCC contribution in these brain regions. Our findings pave the way for better understanding how TMEM16B function contributes to physiology at the neuronal, circuit, and behavioral levels.

MATERIALS AND METHODS

ANIMALS

All experimental mice used in this study were bred from the TMEM16B mCherry KO mouse line (Zhang et al., 2017). All animal experiments were done in strict accordance with the *Guide for the Care and Use of Laboratory Animals* by the National Institutes of Health. All animal protocols used in this study were approved by the Institutional Animal Use and Care Committee at the University of California San Francisco.

ACUTE BRAIN SLICE PREPARATION

Male and female TMEM16B WT and KO mice ages 3-4 months old were anesthetized using isoflurane and perfused with ice-cold NMDG-based cutting solution (in mM): 93 NMDG, 2.5 KCl, 1.2 NaH_2PO_4, 20 HEPES, 25 glucose, 5 Sodium Ascorbate, 2 Mannitol, 3 Sodium

Pyruvate, 10 $MgSO_4$, 0.5 $CaCl_2$, pH ~7.3-7.4, ~300-310 mOsm. Brains were immediately

removed and submerged in ice-cold NMDG cutting solution. Brains were sliced into 350 μm

sections using a Leica VT 1000S vibratome. Slices were placed in a holding chamber in NMDG-

based cutting solution at 33^OC for 15 minutes, then transferred to a second holding chamber at

room temperature containing HEPES-based ACSF solution (in mM): 92 NaCl, 2.5 KCl, 1.2

NaH_2PO_4, 30 $NaHCO_3$, 20 HEPES, 25 Glucose, 5 Sodium Ascorbate, 2 Mannitol, 3 Sodium

Pyruvate, 2 $MgSO_4$, 2 $CaCl_2$, pH 7.3-7.4, ~300-310 mOsm. All solutions were equilibrated with

5% CO_2 + 95 % O_2. Slices were held at room temperature for at least 45 minutes before being

used for recordings.

SLICE ELECTROPHYSIOLOGY AND OPTOGENETIC RECORDINGS

Whole-cell patch clamp recordings were performed on prepared brain slices and

continuously perfused with ACSF using a peristaltic pump and equilibrated with 5% CO_2 + 95 %

O_2. For spontaneous EPSP recordings, slices were perfused with ACSF using the following

recipe (in mM): 127 NaCl, 1.8 KCl, 26 $NaHCO_3$, 12 KH_2PO_4, 1.3 $MgSO_4$, 2.4 $CaCl_2$, 15

glucose. The pH was adjusted to within a range of 7.3-7.4 using HCl. Osmolarity was adjusted

to a range of 300-305 mOsm. A K-Methanesulfonate-based internal solution was used (in mM):

135 K-Methanesulfonate, 6.5 KCl, 2 $MgCl_2$, 4 Na-ATP, 0.2 EGTA, 10 HEPES, pH ~7.2 with

KOH, ~290-300 mOsm. The slice chamber was kept at 33^OC during recordings.

All recordings were done using the patch clamp amplifier, MultiClamp700B (Axon

Instruments), the data acquisition system Digidata 1322A (Axon Instruments), Axioskop2 FS

plus upright microscope (Zeiss Microscopy), and Clampex9 (Molecular Devices). Neurons were

visualized with a CCD Camera (Hamamatsu). Pipette tips were pulled the day of use with a P-

1000 Pipette Puller (Sutter Instruments) with seal resistances of 4-9 MΩ. Pipette tips were made of thick/standard wall borosilicate glass (ID 0.86 mm, OD 1.50 mm). Optogenetic recordings were done using a Lambda DG4 light source (Sutter Instruments) and neutral density filters to regulate light intensity. Pharmacological drugs used included 100 μM Picrotoxin (Tocris) and 1 μM Tetrodotoxin (Tocris). All drugs were added to the ACSF solution. All electrophysiology data was analyzed using Clampfit10 and Graphpad Prism 6. Only cells with access resistance < 40 MΩ were analyzed. Passive leak was subtracted from tail current recordings offline prior to subsequent analysis.

STEREOTAXIC SURGERY

Mice were anesthetized with 2% vaporized isofluorane with O_2 and administered a mixture of ketamine (80-100 mg/kg) and xylazine (5-10 mg/kg) via intraperitoneal (IP) injection and subcutaneous (SC) injections of meloxicam (5-10 mg/kg), buprenorphine (0.05-01 mg/kg), and ampicillin (10-20 mg/kg). Mice were prepped for surgery by shaving and cleaning the head and skull with alcohol wipes and iodine. Surgeries were done using a Robot Stereotax (Neurostar, Tubingen, Germany), Olympus SZ61 microscope, and a constant flow of 1% vaporized isofluorane with O_2. For studies using channelrhodopsin, mice were injected using a Hamilton syringe with 500 nl of AAV5-CAMKII-ChR2(H134R)-EYFP with titer $\geq 1 \times 10^{13}$ vg/mL (Penn Vector Core, Deisseroth Lab). Coordinates used for experiments included: CA3 region (-2.18 AP, -2.14 ML, 2.21 DV) and the LHA (-1.46 AP, -0.85 ML, 5.1 DV). For retrograde tracing studies, mice were injected using a Hamilton syringe with 500 nl of Cholera Toxin subunit B (Molecular Probes, Eugene, OR) into the LS (0.14 AP, -0.22 ML, 2.6 DV).

On Post-Surgical Day 1, mice were given SC injections of meloxicam (5-10 mg/kg) and ampicillin (10-20 mg/kg). Mice were also given SC injections of buprenorphine (0.05-01 mg/kg) if pain was observed. Mice were monitored four days post surgery and weight measurements were recorded. 17-21 days after surgery, mice were prepped for whole cell patch clamp physiology experiments according to the "acute slice preparation" section.

MOUSE PERFUSIONS

Male and female TMEM16B KO mice 4-5 months old injected with Cholera Toxin subunit B were anesthetized using isoflurane and perfused with 1x phosphate buffered saline (PBS), followed by 4% Paraformaldehyde (PFA) in 1x PBS. After brain dissection, brains were placed in 4% PFA for 4 hours followed by 30% sucrose for two days. Brains were frozen in OCT and sectioned into 30 um thick coronal sections using a Leica CM3050 S cryostat. Brain sections not used immediately were stored in cryoprotectant solution at -20°C (40% 1X PBS, 30% ethylene glycol, 30% glycerol).

Sections were mounted onto Superfrost Plus Microscope Slides (Fisherbrand). Glass coverslips were placed on top of the slides using 150 μl DAPI Fluoromount-G mounting media (SouthernBiotech).

MICROSCOPY AND CELL COUNT ANALYSIS

All fluorescent imaging was done using a Leica SP8 confocal microscope. Tile scan images were taken at 20x magnification. Cholera Toxin B+ cells in the CA3 region were manually counted using ImageJ (ImageJ, RRID: SCR_003070).

EXPERIMENTAL DESIGN AND STATISTICAL ANALYSIS

This study used TMEM16B WT and KO mice bred from the TMEM16B mCherry KO mouse line (Zhang et al., 2017). All data were analyzed using Graphpad Prism 6 and all values reported are Mean±SEM. Spontaneous EPSCs were collected from recording files using Clampfit10 (Molecular Devices, San Jose, CA), miniature EPSCs were collected from recording files using Mini Analysis Program (Synaptosoft Inc., Fort Lee, NJ). For statistical analysis of data from electrophysiology and CTB+ cell count experiments, Student's t-test or Multiple Student's t-test was conducted with an alpha value of $p<0.05$.

AUTHOR CONTRIBUTIONS

Lynn Wang, Christian J. Peters, Marena Tynan-La Fontaine, Yuh Nung Jan, and Lily Yeh Jan contributed to this work. L.W., C.J.P., and L.Y.J. conceived and designed experiments. L.W. and M.T.L.F. performed experiments. L.W., C.J.P., and L.Y.J. contributed to writing of this study.
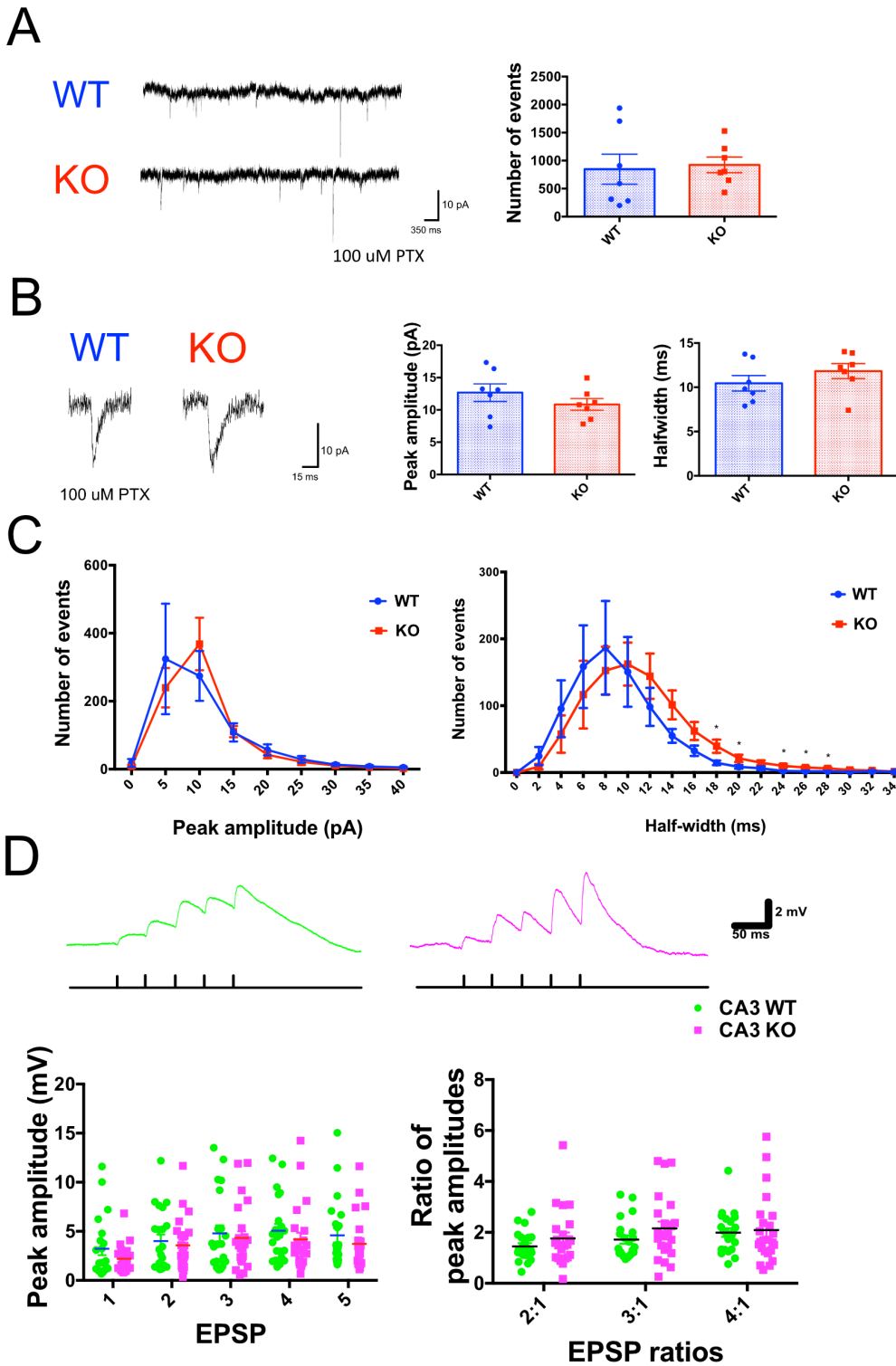
Figure 3.1. TMEM16B function does not regulate spontaneous or excitatory post-synaptic firing in LS neurons. *A,* Representative traces of spontaneous EPSC recordings in TMEM16B WT and KO LS neurons (left). All recordings were done with 100 μM PTX in bath solution. No significant differences in spontaneous EPSC firing frequency are detected (*p*=0.8041, Student's t-test). ***B,*** Representative traces of a single spontaneous EPSC in TMEM16B WT and KO LS

neurons (left). No differences in EPSC peak amplitude (p=0.2877, Student's t-test) or EPSC halfwidth (p=0.2796, Student's t-test) detected. *C,* No significant differences detected in frequency distribution of spontaneous EPSC peak amplitude (left; Multiple Student's t-test, p>0.05 for all peak amplitude values). TMEM16B KO LS neurons show increased frequency of spontaneous EPSCs with halfwidths of 18 ms (p=0.0363), and 24-28 ms (p=0.0241, p=0.0212, p=0.0300) (right; Multiple Student's t-test). *A-C,* Sample size: WT *n*=7, KO *n*=7. *D,* Representative traces of evoked EPSP temporal summations from TMEM16B WT and KO LS neurons with optogenetic stimulation, five 1 ms pulses with 50 ms intervals (top). No significant differences seen in EPSP amplitudes (left; Multiple Student's t-test, p>0.05 for all comparisons) or EPSP ratios (right; Multiple Student's t-test, p>0.05 for all comparisons). Sample size: WT *n*=22, KO *n*=23. All error bars show SEM.
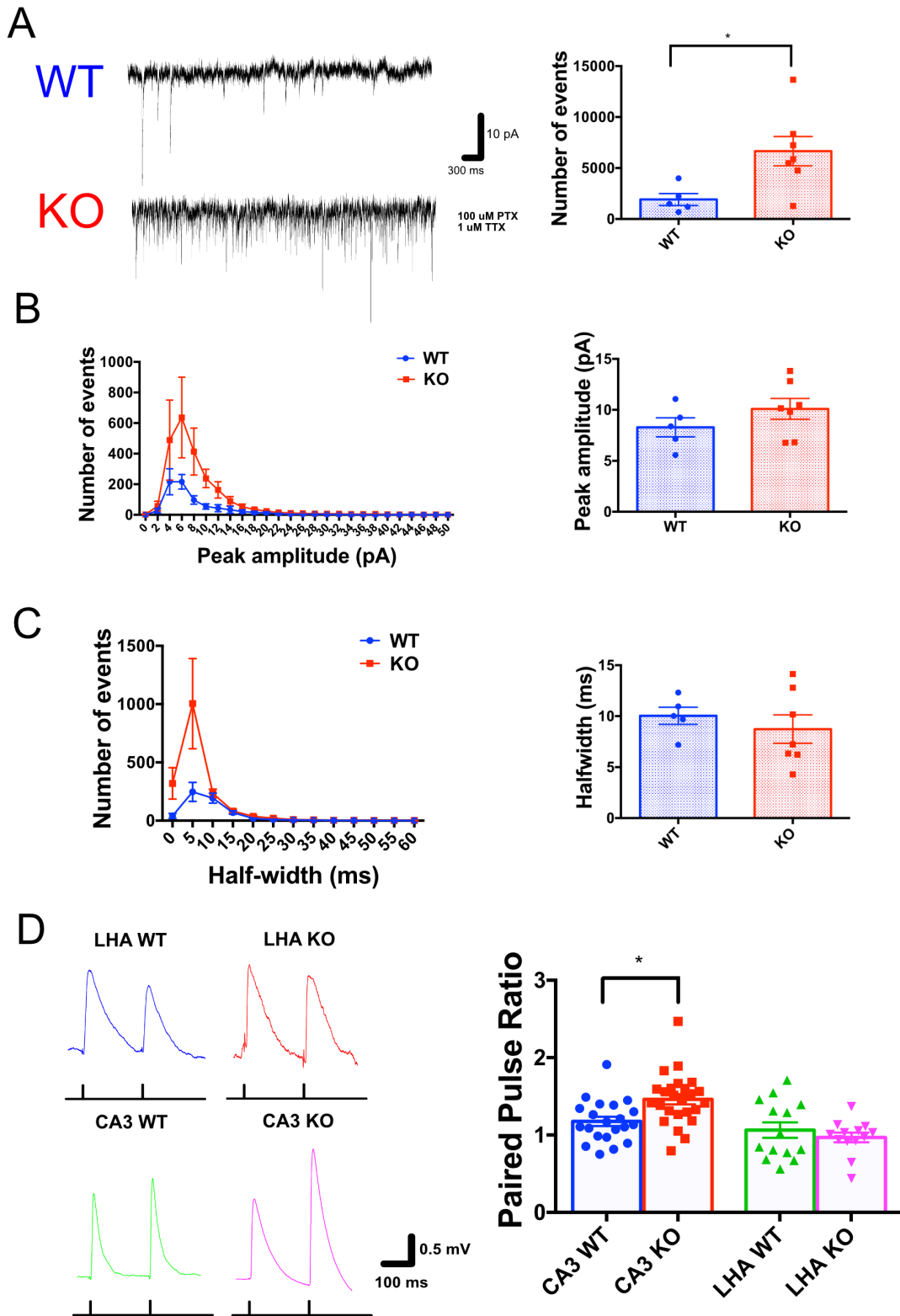
Figure 3.2: TMEM16B function contributes to neurotransmitter release at the hippocampal-septal synapse. *A,* Representative traces of miniature excitatory post-synaptic current (mEPSC) whole cell recordings of LS neurons in TMEM16B WT and KO mice (left).

All recordings were done with 100 µM PTX and 1µM in ACSF bath solution. Quantification of the number of mEPSCs show increased mEPSC frequency in TMEM16B KO LS neurons compared to WT LS neurons (right) (*p*=0.07, Student's t-test). ***B,*** No significant differences seen in the frequency distribution of mEPSC peak amplitude values (left) and mean mEPSC peak amplitude (right) between TMEM16B WT and KO LS neurons (*p*=0.2377), Student's t-test. ***C,*** No significant differences seen in the frequency distribution of mEPSC halfwidth values (left) and mean mEPSC halfwidth (right) between TMEM16B WT and KO LS neurons (*p*=0.4902), Student's t-test. Sample size: WT *n=5*, KO *n*=7. ***D,*** Representative traces of EPSP paired pulse ratio recordings with two 1 ms pulses of light, 120 ms interval, via optogenetic stimulation of LS inputs from the lateral hypothalamic area (LHA) and CA3 region of the hippocampus (left). Paired pulse ratios: WT LHA =1.063, KO LHA = 0.9685, WT CA3 = 1.176, KO CA3= 1.462 (right). 2-WAY ANOVA, Sidak's Multiple Comparisons. Sample sizes: WT LHA *n*=14, KO LHA *n*=13, WT CA3 *n*=21, KO CA3 *n*=25. All error bars show SEM.
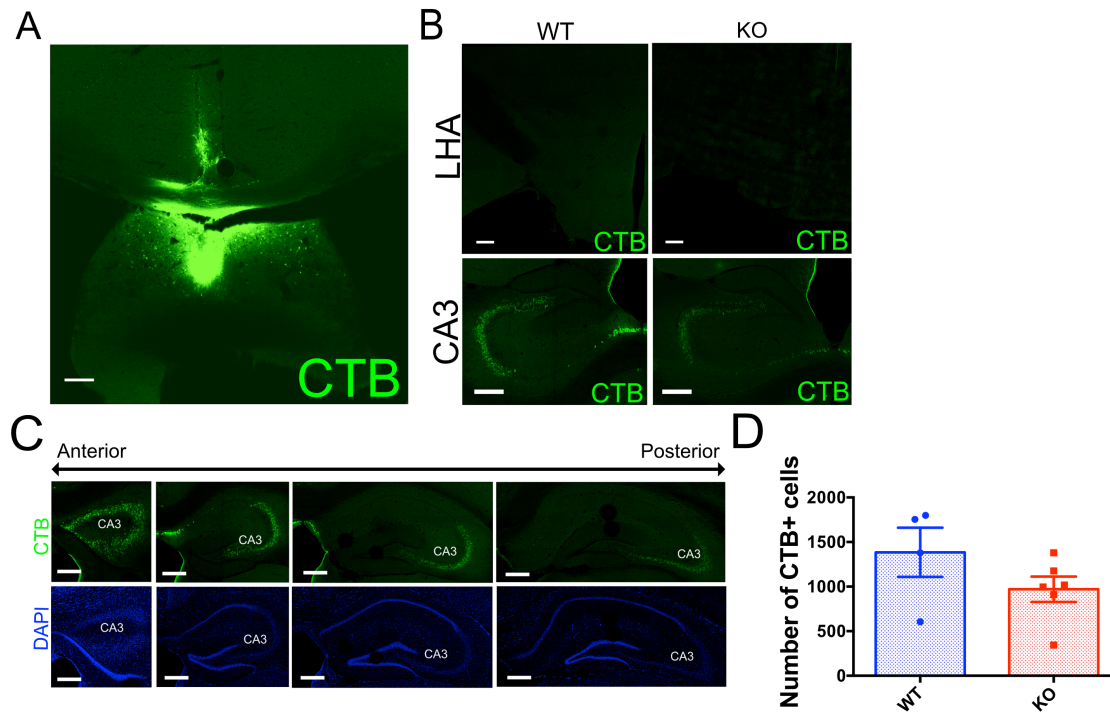
Figure 3.3. TMEM16B KO mice show no difference in the number of CA3 inputs innervating the LSc. Injection of Cholera Toxin B with Alexa Fluor 488 conjugation into the LSc (**A**) shows high CTB expression in the CA3 region of the hippocampus and low CTB expression in the lateral hypothalamic area (**B**). **C,** A comprehensive characterization of CTB expression in CA3 shows broad expression along the anterior to posterior axis. **D,** Quantification of the number of CTB+ cells in CA3 between TMEM16B WT and KO mice show no significant difference ($p= 0.1795$). Student's t test, WT $n=4$, KO $n=6$. Scale bars, 200 μm. All error bars show SEM.

CONCLUSIONS AND FUTURE DIRECTIONS

The work described in the previous chapters provides novel insight into the function of the calcium-activated chloride channel, TMEM16B, and its role in lateral septum (LS) physiology, circuitry, and behavior.

In Chapter 2, we discussed the role of TMEM16B in regulating action potential firing of LS neurons and its modulation of aggressive behaviors in male mice. We identified high TMEM16B expression in neurons of the LS, which led us to investigate its role in regulating behaviors associated with LS function. We found that TMEM16B KO mice engaged in aggressive behaviors spend more time engaged in attack compared to their WT littermates. However, TMEM16B KO mice showed no differences in direct social interaction or anxiety-related behaviors compared to WT littermates. Using whole cell recordings, we identified the presence of calcium-activated chloride currents in LS neurons. We identified three LS neuronal subpopulations based on their firing characteristics, and found that subpopulations of LS neurons show increased spike frequency and spike frequency adaptation in TMEM16B KO LS neurons. We further demonstrated that synaptic connections between the LS and its inputs regions are maintained despite loss of TMEM16B function.

In Chapter 3, we further investigated the function of TMEM16B at the hippocampal-septal synapse, an important connection with implications in the regulation of hippocampal theta oscillation generation. We demonstrated that TMEM16B is not required for the regulation of spontaneous or evoked excitatory post-synaptic activity in the dendritic region of LS neurons. However, we unexpectedly found that TMEM16B function is present in the axon terminals of the hippocampal CA3 region, where it is involved in regulating neurotransmitter release at the

hippocampus-lateral septum synapse.

In summary, these studies shed light on TMEM16B function in a previously unreported region, the mouse lateral septum. Based on our findings, it is evident that TMEM16B regulates LS neuronal excitability and aggressive behaviors. It would be interesting to continue exploring the neural circuitry underlying the aggression phenotype we observed in the TMEM16B KO mouse model. The proposed neural circuit regulating aggression from CA2 to the LS (Leroy et al., 2018) complements our findings regarding LS regulation of aggression, and provides a framework with which to approach future study of TMEM16B function in the LS given that we observe major input from the adjacent hippocampal region, CA3 to areas of the LS that express TMEM16B.

In addition, we also found the brain regions where we observe mCherry fibers in the TMEM16B KO mouse to be very striking. These regions include the medial septum (MS), nucleus of the diagonal band (NDB), lateral preoptic area (LPO), and lateral hypothalamic area (LHA). The MS and NDB are important in generating hippocampal theta oscillations in the brain, while the LPO and LHA are known to be involved in aggressive and defensive behaviors and locomotion. Further evidence from the literature suggest that hippocampal theta oscillations also help to regulate these behaviors (Bender et al., 2015; Chee et al., 2015). Thus, it's possible that TMEM16B functions to regulate the firing of neurons underlying theta oscillation regulation and its corresponding effects on aggressive behaviors. Investigating the candidate output regions of TMEM16B-expressing LS neurons would help elucidate the effect of LS function on these neural circuits. Moreover, a thorough investigation of TMEM16B contribution to hippocampal theta oscillations could help us better understand how these synchronous brain waves affect the circuits associated with emotional and mood-related behaviors.

One potential caveat regarding the implications of our findings is the fact that TMEM16B is expressed in hippocampal pyramidal neurons (Huang et al., 2012b) and LS neurons. Given that our mouse model is a full knockout of TMEM16B, LS contribution to the aggression phenotype we observe may be confounded by TMEM16B contribution to hippocampal function. However, given that we observed a difference in neuronal excitability between TMEM16B KO and WT neurons, it's likely (although speculative) the difference in spike firing would still correlate with a difference in aggression at the behavioral level.

Understanding TMEM16B's role in LS function could also shed light on its role in neural circuits underlying mental illnesses and psychiatric disorders (Sheehan et al., 2004). Many of these illnesses, such as depression, schizophrenia, and anxiety disorders, remain poorly understood. Currently, no cures exist for these illnesses and treatments are limited. People who suffer from these illnesses are often stigmatized and can be, to some extent, marginalized by society. It's imperative that we work to study the neural circuits underlying these diseases. TMEM16B function in the LS provides a means to elucidate some of these mechanisms. This will lead to a better understanding of LS contribution, in both healthy and abnormal settings.

REFERENCES

Albert DJ, Brayley KN (1979) Mouse killing and hyperreactivity following lesions of the medial hypothalamus, the lateral septum, the bed nucleus of the stria terminalis, or the region ventral to the anterior septum. Physiol Behav 23:439–443.

Albert DJ, Chew GL (1980) The septal forebrain and the inhibitory modulation of attack and defense in the rat. A review. Behav Neural Biol 30:357–388.

Albert DJ, Richmond SE (1976) Hyperreactivity and aggressiveness following infusion of local anesthetic into the lateral septum or surrounding structures. Behav Biol 18:211–226.

Albert DJ, Walsh ML, Gorzalka BB, Mendelson S, Zalys C (1986) Intermale social aggression: Suppression by medial preoptic area lesions. Physiol Behav 38:169–173.

Albert DJ, Wong RC (1978) Hyperreactivity, muricide, and intraspecific aggression in the rat produced by infusion of local anesthetic into the lateral septum or surrounding areas. J Comp Physiol Psychol 92:1062–1073.

Allaman-Exertier G, Reymond-Marron I, Tribollet E, Raggenbass M (2007) Vasopressin modulates lateral septal network activity via two distinct electrophysiological mechanisms. Eur J Neurosci 26:2633–2642.

Alonso A, Llinas RR (1989) Subthreshold Na+-dependent theta-like rhythmicity in stellate cells of entorhinal cortex layer II. Nature 342:175–177.

Alonso JR, Frotscher M (1989) Organization of the septal region in the rat brain: a Golgi/EM study of lateral septal neurons. J Comp Neurol 286:472–487.

Amjad A, Hernandez-Clavijo A, Pifferi S, Maurya DK, Boccaccio A, Franzot J, Rock J, Menini A (2015) Conditional knockout of TMEM16A/anoctamin1 abolishes the calcium-activated

chloride current in mouse vomeronasal sensory neurons. J Gen Physiol 145:285–301.

Anthony TE, Dee N, Bernard A, Lerchner W, Heintz N, Anderson DJ (2014) Control of Stress-Induced Persistent Anxiety by an Extra-Amygdala Septohypothalamic Circuit. Cell 156:522–536.

Augustine GJ, Santamaria F, Tanaka K (2003) Local Calcium Signaling in Neurons. Neuron 40:331–346.

Ayoglu B et al. (2016) Anoctamin2 identified as autoimmune target in multiple sclerosis. PNAS Press 113:1–6.

Bader CR, Bertrand D, Schwartz EA (1982) Voltage-activated and calcium-activated currents studied in solitary rod inner segments from the salamander retina. J Physiol 331:253–284.

Bale TL, Vale W (2004) CRF ANDCRF R ECEPTORS: Role in Stress Responsivity and Other Behaviors. Annu Rev Pharmacol Toxicol 44:525–557.

Barish BYME (1983) A transient calcium-dependent chloride current in the immature Xenopus oocyte. J Physiol 342:309–325.

Batti L, Sundukova M, Murana E, Pimpinella S, De Castro Reis F, Pagani F, Wang H, Pellegrino E, Perlas E, Di Angelantonio S, Ragozzino D, Heppenstall PA (2016) TMEM16F Regulates Spinal Microglial Function in Neuropathic Pain States. Cell Rep 15:2608–2615.

Bender F, Gorbati M, Cadavieco MC, Denisova N, Gao X, Holman C, Korotkova T, Ponomarenko A (2015) Theta oscillations regulate the speed of locomotion via a hippocampus to lateral septum pathway. Nat Commun 6:1–11.

Betley JN, Cao ZFH, Ritola KD, Sternson SM (2013) Parallel, redundant circuit organization for homeostatic control of feeding behavior. Cell 155:1337–1350.

Betto G, Cherian OL, Pifferi S, Cenedese V, Boccaccio A, Menini A (2014) Interactions

between permeation and gating in the TMEM16B/anoctamin2 calcium-activated chloride channel. J Gen Physiol 143:703–718.

Billig GM, Pál B, Fidzinski P, Jentsch TJ (2011) Ca2+-activated Cl− currents are dispensable for olfaction. Nat Neurosci 14:763–769.

Brady J V., Nauta WJH (1955) Subcortical mechanisms in emotional behavior: The duration of affective changes following septal and habenular lesions in the albino rat. J Comp Physiol Psychol 48:412–420.

Brady J V, Nauta WJH (1953) Subcortical mechanisms in emotional behavior: affective changes following septal forebrain lesions in the albino rat. J Comp Physiol Psychol 46:339–346.

Brayley KN, Albert DJ (1977) Suppression of VMH-lesion induced reactivity and aggressiveness by electrical stimulation ventral to the anterior septum in the rat. Physiol Behav 18:567–571.

Brunner JD, Lim NK, Schenck S, Duerst A, Dutzler R (2014) X-ray structure of a calcium-activated TMEM16 lipid scramblase. Nature 516:207–212.

Buzsáki G (2002) Theta oscillations in the hippocampus. Neuron 33:325–340.

Buzsáki G, Moser EI (2013) Memory, navigation and theta rhythm in the hippocampal-entorhinal system. Nat Neurosci 16:130–138.

Canteras NS, Simerly RB, Swanson LW (1994) Organization of projections from the ventromedial nucleus of the hypothalamus: A Phaseolus vulgaris–Leucoagglutinin study in the rat. J Comp Neurol 348:41–79.

Caputo A, Caci E, Ferrera L, Pedemonte N, Barsanti C, Sondo E, Pfeffer U, Ravazzolo R, Zegarra-Moran O, Galietta LJ V (2008) TMEM16A, a membrane protein associated with calcium-dependent chloride channel activity. Science 322:590–594.

Cenedese V, Betto G, Celsi F, Cherian OL, Pifferi S, Menini A (2012) The voltage dependence of the TMEM16B/anoctamin2 calcium-activated chloride channel is modified by mutations in the first putative intracellular loop. J Gen Physiol 139:285–294.

Cenedese V, Mezzavilla M, Morgan A, Marino R, Pietro Ettorre C, Margaglione M, Gasparini P, Menini A (2015) Assessment of the olfactory function in italian patients with type 3 von willebrand disease caused by a homozygous 253 Kb deletion involving VWF and TMEM16B/ANO2. PLoS One 10:1–11.

Chamero P, Leinders-Zufall T, Zufall F (2012) From genes to social communication: Molecular sensing by the vomeronasal organ. Trends Neurosci 35:597–606.

Chamova T, Florez L, Guergueltcheva V, Raycheva M, Kaneva R, Lochmü ller H, Kalaydjieva L, Tournev I (2012) ANO10 c.1150-1151del is a founder mutation causing autosomal recessive cerebellar ataxia in Roma/Gypsies. J Neurol 259:906–911.

Chee S-S a, Menard JL, Dringenberg HC (2015) The lateral septum as a regulator of hippocampal theta oscillations and defensive behavior in rats. J Neurophysiol 113:1831–1841.

Chiba T, Murata Y (1985) Afferent and efferent connections of the medial preoptic area in the rat: A WGA-HRP study. Brain Res Bull 14:261–272.

Cho SJ a., Jeon JH yu., Chun DI l., Yeo SW o., Kim IB (2014) Anoctamin 1 expression in the mouse auditory brainstem. Cell Tissue Res 357:563–569.

Cia D, Bordais A, Varela C, Forster V, Sahel JA, Rendon A, Picaud S (2005) Voltage-Gated Channels and Calcium Homeostasis in Mammalian Rod Photoreceptors. J Neurophysiol 93:1468–1475.

Curley JP, Jensen CL, Franks B, Champagne FA (2012) Variation in maternal and anxiety-like

behavior associated with discrete patterns of oxytocin and vasopressin 1a receptor density in the lateral septum. Horm Behav 61:454–461.

Dang S, Feng S, Tien J, Peters CJ, Bulkley D, Lolicato M, Zhao J, Zuberbühler K, Ye W, Qi L, Chen T, Craik CS, Jan YN, Minor DL, Cheng Y, Jan LY (2017) Cryo-EM structures of the TMEM16A calciumactivated chloride channel. Nature 552:426–429.

Debanne D, Guérineau NC, Gähwiler BH, Thompson SM (1996) Paired-pulse facilitation and depression at unitary synapses in rat hippocampus: Quantal fluctuation affects subsequent release. J Physiol 491:163–176.

Dibattista M, Amjad A, Maurya DK, Sagheddu C, Montani G, Tirindelli R, Menini A (2012) Calcium-activated chloride channels in the apical region of mouse vomeronasal sensory neurons. J Gen Physiol 140:3–15.

Dilokthornsakul P, Valuck RJ, Nair K V., Corboy JR, Allen RR, Campbell JD (2016) Multiple sclerosis prevalence in the United States commercially insured population. Neurology 86:1014–1021.

Excitatory VF, Septum D (1990) Vasopressin Facilitates Excitatory Dorso-Lateral Septum. 206.

Falkner AL, Lin D (2014) Recent advances in understanding the role of the hypothalamic circuit during aggression. Front Syst Neurosci 8:1–14.

Falzone ME, Malvezzi M, Lee B-C, Accardi A (2018) Known structures and unknown mechanisms of TMEM16 scramblases and channels. J Gen Physiol 150:933–947.

Fanselow MS, Dong H-W (2010) Are the dorsal and ventral hippocampus functionally distinct structures? Neuron 65:7–19.

Firestein S (2001) How the Olfactory system makes sense of scents. Nature 413:211–218.

Fujii T, Sakata A, Nishimura S, Eto K, Nagata S (2015) TMEM16F is required for

phosphatidylserine exposure and microparticle release in activated mouse platelets. Proc Natl Acad Sci 112:12800–12805.

Gallagher JP, Zheng F, Hasuo H, Shinnick-Gallagher P (1995) Activities of neurons within the rat dorsolateral septal nucleus (DLSN). Prog Neurobiol 45:373–395.

Gammie SC, Stevenson SA (2006) Effects of daily and acute restraint stress during lactation on maternal aggression and behavior in mice. Stress 9:171–180.

Gavioli EC, Canteras NS, De Lima TCM (1999) Anxiogenic-like effect induced by substance P injected into the lateral septal nucleus. Neuroreport 10:3399–3403.

Ha GE, Lee J, Kwak H, Song K, Kwon J, Jung SY, Hong J, Chang GE, Hwang EM, Shin HS, Lee CJ, Cheong E (2016) The Ca2+-activated chloride channel anoctamin-2 mediates spike-frequency adaptation and regulates sensory transmission in thalamocortical neurons. Nat Commun 7:1–13.

Hartzell C, Putzier I, Arreola J, Emala CW (2005) Calcium-activated chloride channels. Calcium-Activated Chloride Channels 67:719–758.

Hille B (2001) Ion Channels of Excitable Membranes, Third. Sunderland, MA: Sinauer Associates, Inc.

Hu H, Shao LR, Chavoshy S, Gu N, Trieb M, Behrens R, Laake P, Pongs O, Knaus HG, Ottersen OP, Storm JF (2001) Presynaptic Ca2+-activated K+ channels in glutamatergic hippocampal terminals and their role in spike repolarization and regulation of transmitter release. J Neurosci 21:9585–9597.

Huang F, Wang X, Ostertag EM, Nuwal T, Huang B, Jan Y-N, Basbaum AI, Jan LY (2013) TMEM16C facilitates Na+-activated K+ currents in rat sensory neurons and regulates pain processing. Nat Neurosci 16:1284–1290.

Huang F, Wong X, Jan LY (2012a) International Union of Basic and Clinical Pharmacology . LXXXV : Calcium-Activated. 64:1–15.

Huang WC, Xiao S, Huang F, Harfe BD, Jan YN, Jan LY (2012b) Calcium-activated chloride channels (CaCCs) regulate action potential and synaptic response in hippocampal neurons. Neuron 74:179–192.

Jan LY, Jan YN (1989) Voltage-sensitive ion channels. Cell 56:13–25.

Jarrard LE (1993) On the role of the hippocampus in learning and memory in the rat. Behav Neural Biol 60:9–26.

Jeng G, Aggarwal M, Yu W-P, Chen T-Y (2016) Independent activation of distinct pores in dimeric TMEM16A channels. J Gen Physiol 148:393–404.

Jeon JH, Paik SS, Chun MH, Oh U, Kim IB (2013) Presynaptic Localization and Possible Function of Calcium-Activated Chloride Channel Anoctamin 1 in the Mammalian Retina. PLoS One 8.

Kanazawa T, Matsumoto S (2014) Expression of transient receptor potential vanilloid 1 and anoctamin 1 in rat trigeminal ganglion neurons innervating the tongue. Brain Res Bull 106:17–20.

Kim U, Chung L -y. (2007) Dual GABAergic Synaptic Response of Fast Excitation and Slow Inhibition in the Medial Habenula of Rat Epithalamus. J Neurophysiol 98:1323–1332.

King C, Recce M, O'Keefe J (1998) The rhythmicity of cells of the medial septum/diagonal band of Broca in the awake freely moving rat: Relationships with behaviour and hippocampal theta. Eur J Neurosci 10:464–477.

Kleene SJ (1993) Origin of the chloride current in olfactory transduction. Neuron 11:123–132.

Kleene SJ, Gesteland RC (1991) Calcium-activated chloride conductance in frog olfactory cilia.

J Neurosci 11:3624–3629.

Kodirov S a., Wehrmeister M, Colom L V. (2014) Modulation of HCN channels in lateral
septum by nicotine. Neuropharmacology 81:274–282.

Koolhaas JM (1978) Hypothalamically induced intraspecific aggressive behaviour in the rat. Exp
Brain Res 32:365–375.

Kramer J, Hawley RS (2003) The spindle-associated transmembrane protein Axs identifies a
membranous structure ensheathing the meiotic spindle. Nat Cell Biol 5:261–263.

Kruk MR, Van Der Poel AM, Meelis W, Hermans J, Mostert PG, Mos J, Lohman AHM (1983)
Discriminant analysis of the localization of aggression-inducing electrode placements in the
hypothalamus of male rats. Brain Res 260:61–79.

Lancaster, B., Nicoll RA (1987) PROPERTIES OF TWO CALCIUM-ACTIVATED
HYPERPOLARIZATIONS IN RAT HIPPOCAMPAL NEURONES. J Physiol 389:187–
203.

Landisman CE, Connors BW (2007) VMP and PoM Nuclei of the Rat Somatosensory Thalamus:
intrinsic Neuronal Properties and Corticothalamic Feedback. Cereb Cortex 17:2853–2865.

Lawson VH, Bland BH (1993) The Role of the Septohippocampal Pathway in the Regulation of
Hippocampal Field Activity and Behavior: Analysis by the Intraseptal Microinfusion of
Carbachol, Atropine, and Procaine. Exp Neurol 120:132–144.

Le Masson G, Renaud-Le Masson S, Debay D, Bal T (2002) Feedback inhibition controls spike
transfer in hybrid thalamic circuits. Nature 417:854–858.

Lee BC, Menon AK, Accardi A (2016) The nhTMEM16 Scramblase Is Also a Nonselective Ion
Channel. Biophys J 111:1919–1924.

Lee G, Gammie SC (2009) GABAA Receptor Signaling in the Lateral Septum Regulates

Maternal Aggression in Mice. Behav Neurosci 123:1169–1177.

Leroy F, Park J, Asok A, Brann DH, Meira T, Boyle LM, Buss EW, Kandel ER, Siegelbaum SA

(2018) A circuit from hippocampal CA2 to lateral septum disinhibits social aggression.

Nature.

Leung LS, Martin L a, Stewart DJ (1994) Hippocampal theta rhythm in behaving rats following

ibotenic acid lesion of the septum. Hippocampus 4:136–147.

Lim NK, Lam AKM, Dutzler R (2016) Independent activation of ion conduction pores in the

double-barreled calcium-activated chloride channel TMEM16A. J Gen Physiol 148:375–

392.

Lin D, Boyle MP, Dollar P, Lee H, Lein ES, Perona P, Anderson DJ (2011) Functional

identification of an aggression locus in the mouse hypothalamus. Nature 470:221–226.

Llinás R, Yarom Y (1981a) Electrophysiology of mammalian inferior olivary neurones *in vitro*.

Different types of voltage-dependent ionic conductances. J Physiol 315:549–567.

Llinás R, Yarom Y (1981b) Properties and distribution of ionic conductances generating

electroresponsiveness of mammalian inferior olivary neurones in vitro. J Physiol 315:569–

584.

Luhmann HJ, Prince DA (1991) Postnatal maturation of the GABAergic system in rat neocortex.

J Neurophysiol 65:247–263.

Luo AH, Tahsili-Fahadan P, Wise R a, Lupica CR, Aston-Jones G (2011) Linking context with

reward: a functional circuit from hippocampal CA3 to ventral tegmental area. Science

333:353–357.

Malvezzi M, Chalat M, Janjusevic R, Picollo A, Terashima H, Menon AK, Accardi A (2013)

Ca2+-dependent phospholipid scrambling by a reconstituted TMEM16 ion channel. Nat

Commun 4:1–9.

Maricq AV, Korenbrot JI (1988) Calcium and calcium-dependent chloride currents generate action potentials in solitary cone photoreceptors. Neuron 1:503–515.

McCormick DA, von Krosigk M (1992) Corticothalamic activation modulates thalamic firing through glutamate "metabotropic" receptors. Proc Natl Acad Sci 89:2774–2778.

Mogenson GJ, Jones DL, Yim CY (1980) From motivation to action: Functional interface between the limbic system and the motor system. Prog Neurobiol 14:69–97.

Moser M, Moser EI (1998) Functional differentiation in the hippocampus. Hippocampus 8:608–619.

Münch J, Billig G, Hübner CA, Leinders-Zufall T, Zufall F, Jentsch TJ (2018a) Ca2+-activated Cl-currents in the murine vomeronasal organ enhance neuronal spiking but are dispensable for male-male aggression. J Biol Chem 293:10392–10403.

Münch J, Billig G, Huebner CA, Leinders-Zufall T, Zufall F, Jentsch TJ (2018b) Ca2+-activated Cl− currents in the murine vomeronasal organ enhance neuronal spiking but are dispensable for male-male aggression. J Biol Chem:jbc.RA118.003153.

Nachman-Clewner M, Jules RST, Townes-Anderson E (1972) L-Type Calcium Channels in the Photoreceptor Ribbon Synapse: Localization and Role in Plasticity. J Comp Neurol 9:58–59.

Nelson RJ, Trainor BC (2007) Neural mechanisms of aggression. Nat Rev Neurosci 8:536–546.

Ngo-Anh TJ, Bloodgood BL, Lin M, Sabatini BL, Maylie J, Adelman JP (2005) SK channels and NMDA receptors form a Ca2+-mediated feedback loop in dendritic spines. Nat Neurosci 8:642–649.

Otowa T, Kawamura Y, Sugaya N, Yoshida E, Shimada T, Liu X, Tochigi M, Umekage T,

Miyagawa T, Nishida N, Kaiya H, Okazaki Y, Tokunaga K, Sasaki T (2009) Genome-wide association study of panic disorder in the Japanese population. Nat J Hum Genet 54:122–126.

Paulino C, Kalienkova V, Lam AKM, Neldner Y, Dutzler R (2017) Activation mechanism of the calcium-activated chloride channel TMEM16A revealed by cryo-EM. Nature 552:421–425.

Pedemonte M, Barrenechea C, Nuñez A, Gambini JP, García-Austt E (1998) Membrane and circuit properties of lateral septum neurons: Relationships with hippocampal rhythms. Brain Res 800:145–153.

Pedemonte N, Galietta LJ V (2014) Structure and function of TMEM16 proteins (anoctamins). Physiol Rev 94:419–459.

Pedersen NP, Ferrari L, Venner A, Wang JL, Abbott SBG, Vujovic N, Arrigoni E, Saper CB, Fuller PM (2017) Supramammillary glutamate neurons are a key node of the arousal system. Nat Commun 8.

Peters CJ, Gilchrist JM, Tien J, Bethel NP, Qi L, Chen T, Wang L, Jan YN, Grabe M, Jan LY (2018) The Sixth Transmembrane Segment Is a Major Gating Component of the TMEM16A Calcium-Activated Chloride Channel. Neuron 97:1063–1077.e4.

Peters CJ, Yu H, Tien J, Jan YN, Li M, Jan LY (2015) Four basic residues critical for the ion selectivity and pore blocker sensitivity of TMEM16A calcium-activated chloride channels. Proc Natl Acad Sci 112:3547–3552.

Pietra G, Dibattista M, Menini A, Reisert J, Boccaccio A (2016) The Ca^{2+}-activated Cl^- channel TMEM16B regulates action potential firing and axonal targeting in olfactory sensory neurons. J Gen Physiol 148:293–311.

Pifferi S, Dibattista M, Menini A (2009) TMEM16B induces chloride currents activated by

calcium in mammalian cells. Pflugers Arch Eur J Physiol 458:1023–1038.

Radulovic J, Fischer A, Katerkamp U, Spiess J (2000) Role of regional neurotransmitter receptors in corticotropin-releasing factor (CRF)-mediated modulation of fear conditioning. Neuropharmacology 39:707–710.

Rasche S, Toetter B, Adler J, Tschapek A, Doerner JF, Kurtenbach S, Hatt H, Meyer H, Warscheid B, Neuhaus EM (2010) Tmem16b is specifically expressed in the cilia of olfactory sensory neurons. Chem Senses 35:239–245.

Rawlins JNP, Feldon J, Gray JA (1979) Septo-hippocampal connections and the hippocampal theta rhythm. Exp Brain Res 37:49–63.

Reisert J, Bauer PJ, Yau K-W, Frings S (2003) The Ca-activated Cl Channel and its Control in Rat Olfactory Receptor Neurons. J Gen Physiol 122:349–364.

Risold PY, Swanson LW (1996) Structural evidence for functional domains in the rat hippocampus. Science 272:1484–1486.

Risold PY, Swanson LW (1997a) Connections of the rat lateral septal complex. Brain Res Rev 24:115–195.

Risold PY, Swanson LW (1997b) Chemoarchitecture of the rat lateral septal nucleus. Brain Res Rev 24:91–113.

Rivera C, Voipio J, Kaila K (2005) Two developmental switches in GABAergic signalling: The K+-Cl-cotransporter KCC2 and carbonic anhydrase CAVII. J Physiol 562:27–36.

Robinson J, Manseau F, Ducharme G, Amilhon B, Vigneault E, El Mestikawy S, Williams S (2016) Optogenetic Activation of Septal Glutamatergic Neurons Drive Hippocampal Theta Rhythms. J Neurosci 36:3016–3023.

Sackin H (1995) Further 1995. 57:333-53. Annu Rev Physiol 57:333–353.

Sagheddu C, Boccaccio A, Dibattista M, Montani G, Tirindelli R, Menini A (2010) Calcium concentration jumps reveal dynamic ion selectivity of calcium-activated chloride currents in mouse olfactory sensory neurons and TMEM16b-transfected HEK 293T cells. J Physiol 588:4189–4204.

Satoh H, Qu L, Suzuki H, Saitow F (2013) Depolarization-induced depression of inhibitory transmission in cerebellar Purkinje cells. Physiol Rep 1:1–16.

Schneppenheim R, Castaman G, Federici a. B, Kreuz W, Marschalek R, Oldenburg J, Oyen F, Budde U (2007) A common 253-kb deletion involving VWF and TMEM16B in German and Italian patients with severe von Willebrand disease type 3. J Thromb Haemost 5:722–728.

Schroeder BC, Cheng T, Jan YN, Jan LY (2008) Expression Cloning of TMEM16A as a Calcium-Activated Chloride Channel Subunit. Cell 134:1019–1029.

Schweighofer N, Lang EJ, Kawato M (2013) Role of the olivo-cerebellar complex in motor learning and control. Front Neural Circuits 7:1–9.

Sheehan TP, Chambers RA, Russell DS (2004) Regulation of affect by the lateral septum: implications for neuropsychiatry. Brain Res Rev 46:71–117.

Simerly RB (2002) Wired for Reproduction: Organization and Development of Sexually Dimorphic Circuits in the Mammalian Forebrain. Annu Rev Neurosci 25:507–536.

Simerly RB, Swanson LW (1986) The organization of neural inputs to the medial preoptic nucleus of the rat. J Comp Neurol 246:312–342.

Sinnamon H (1992) Mapping of the Basal Forebrain in the Anesthetized Rat : the " Preoptic Locomotor Region ." Neuroscience 50:197–207.

Sławińska U, Kasicki S (1998) The frequency of rat's hippocampal theta rhythm is related to the

speed of locomotion. Brain Res 796:327–331.

Smith DE, King MB, Hoebel BG (1970) Lateral hypothalamic control of killing: evidence for a cholinoceptive mechanism. Science (80-) 167:900–901.

Sparks PD, LeDoux JE (1995) Septal lesions potentiate freezing behavior to contextual but not to phasic conditioned stimuli in rats. Behav Neurosci 109:184–188.

Spiegel EA, Miller HR, Oppenheimer MJ (1940) Forebrain and Rage Reactions. J Neurophysiol 3:538–548.

Stackman RW, Hammond RS, Linardatos E, Gerlach A, Maylie J, Adelman JP, Tzounopoulos T (2002) Small conductance Ca2+-activated K+ channels modulate synaptic plasticity and memory encoding. J Neurosci 22:10163–10171.

Staiger JF, Nurnberger F (1991) The efferent connections of the lateral septal nucleus in the guinea pig: intrinsic connectivity of the septum and projections to other telencephalic areas. Cell Tissue Res 264:415–426.

Staiger JF, Nürnberger F (1991) The efferent connections of the lateral septal nucleus in the guinea pig: projections to the diencephalon and brainstem. Cell Tissue Res 264:391–413.

Stephan AB, Shum EY, Hirsh S, Cygnar KD, Reisert J, Zhao H (2009) ANO2 is the cilial calcium-activated chloride channel that may mediate olfactory amplification. Proc Natl Acad Sci U S A 106:11776–11781.

Stewart M, Fox SE (1990) Do septal neurons pace the hippocampal theta rhythm? Trends Neurosci 13:163–169.

Stöhr H, Heisig JB, Benz PM, Schöberl S, Milenkovic VM, Strauss O, Aartsen WM, Wijnholds J, Weber BHF, Schulz HL (2009) TMEM16B, a novel protein with calcium-dependent chloride channel activity, associates with a presynaptic protein complex in photoreceptor

terminals. J Neurosci 29:6809–6818.

Storm JF (1987a) Action potential repolarization and a fast after-hyperpolarization in rat
hippocampal pyramidal cells. J Physiol 385:733–759.

Storm JF (1987b) Intracellular injection of a Ca2+ chelator inhibits spike repolarization in
hippocampal neurons. Brain Res 435:387–392.

Suzuki J, Fujii T, Imao T, Ishihara K, Kuba H, Nagata S (2013) Calcium-dependent
phospholipid scramblase activity of TMEM 16 protein family members. J Biol Chem
288:13305–13316.

Suzuki J, Umeda M, Sims PJ, Nagata S (2010) Calcium-dependent phospholipid scrambling by
TMEM16F. Nature 468:834–840.

Swanson LW, Cowan WM (1979) The connections of the septal region in the rat. J Comp Neurol
186:621–655.

Sweeney P, Yang Y (2015) An excitatory ventral hippocampus to lateral septum circuit that
suppresses feeding. Nat Commun 6:10188.

Sweeney P, Yang Y (2016) An Inhibitory Septum to Lateral Hypothalamus Circuit That
Suppresses Feeding. J Neurosci 36:11185–11195.

Swerdlow NR, Swanson LW, Koob GF (1984) Electrolytic lesions of the substantia innominata
and lateral preoptic area attenuate the "supersensitive" locomotor response to apomorphine
resulting from denervation of the nucleus accumbens. Brain Res 306:141–148.

Thoreson WB, Bryson EJ, Rabl K (2003) Reciprocal interactions between calcium and chloride
in rod photoreceptors. J Neurophysiol 90:1747–1753.

Tien J, Peters CJ, Wong XM, Cheng T, Jan YN, Jan LY, Yang H (2014) A comprehensive
search for calcium binding sites critical for TMEM16A calcium-activated chloride channel

activity. Elife 3:1–19.

van den Hooff P, Urban IJ, de Wied D (1989) Vasopressin maintains long-term potentiation in rat lateral septum slices. Brain Res 505:181–186.

Veenema AH, Beiderbeck DI, Lukas M, Neumann ID (2010) Distinct correlations of vasopressin release within the lateral septum and the bed nucleus of the stria terminalis with the display of intermale aggression. Horm Behav 58:273–281.

Vertes RP (2005) Hippocampal theta rhythm: A tag for short-term memory. Hippocampus 15:923–935.

Vincis R, Gschwend O, Bhaukaurally K, Beroud J, Carleton A (2012) Dense representation of natural odorants in the mouse olfactory bulb. Nat Neurosci 15:537–539.

Vouimba RM, Garcia R, Jaffard R (1998) Opposite effects of lateral septal LTP and lateral septal lesions on contextual fear conditioning in mice. Behav Neurosci 112:875–884.

Watanabe R, Sakuragi T, Noji H, Nagata S (2018) Single-molecule analysis of phospholipid scrambling by TMEM16F. Proc Natl Acad Sci:201717956.

Winson J (1978) Loss of Hippocampal Theta Rhythm Results in Spatial Memory Deficit in the Rat. Science (80-) 201:160–163.

Wong LC, Wang L, D'Amour JA, Yumita T, Chen G, Yamaguchi T, Chang BC, Bernstein H, You X, Feng JE, Froemke RC, Lin D (2016) Effective Modulation of Male Aggression through Lateral Septum to Medial Hypothalamus Projection. Curr Biol 26:593–604.

Wong XM, Younger S, Peters CJ, Jan YN, Jan LY (2013) Subdued , a TMEM16 family Ca 2 + - activated Cl − channel in Drosophila melanogaster with an unexpected role in host defense. :1–12.

Woodworth CH (1971) Attack elicited in rats by electrical stimulation of the lateral

hypothalamus. Physiol Behav 6:345–353.

Yang C, Delay RJ (2010) Calcium-activated chloride current amplifies the response to urine in mouse vomeronasal sensory neurons. J Gen Physiol 135:3–13.

Yang H, Kim A, David T, Palmer D, Jin T, Tien J, Huang F, Cheng T, Coughlin SR, Jan YN, Jan LY (2012) TMEM16F Forms a Ca2+-Activated Cation Channel Required for Lipid Scrambling in Platelets during Blood Coagulation. Cell 151:111–122.

Yang YD, Cho H, Koo JY, Tak MH, Cho Y, Shim W-S, Park SP, Lee J, Lee B, Kim B-M, Raouf R, Shin YK, Oh U (2008) TMEM16A confers receptor-activated calcium-dependent chloride conductance. Nature 455:1210–1215.

Zhang BYL, Spigelman I, Carlen PL (1991) Development of GABA-mediated, chloride-dependant inhibition in CA1 pyramidal neurones of immature rat hippocampal slices. J Physiol 444:25–49.

Zhang W, Schmelzeisen S, Parthier D, Frings S, Möhrlen F (2015) Anoctamin Calcium-Activated Chloride Channels May Modulate Inhibitory Transmission in the Cerebellar Cortex. PLoS One 10:e0142160.

Zhang Y, Zhang Z, Xiao S, Tien J, Le S, Le T, Jan LY, Yang H (2017) Inferior Olivary TMEM16B Mediates Cerebellar Motor Learning. Neuron 95:1103–1111.e4.

Zhao C, Eisinger B, Gammie SC (2013) Characterization of GABAergic Neurons in the Mouse Lateral Septum: A Double Fluorescence In Situ Hybridization and Immunohistochemical Study Using Tyramide Signal Amplification. PLoS One 8:e73750.

Publishing Agreement

It is the policy of the University to encourage the distribution of all theses, dissertations, and manuscripts. Copies of all UCSF theses, dissertations, and manuscripts will be routed to the library via the Graduate Division. The library will make all theses, dissertations, and manuscripts accessible to the public and will preserve these to the best of their abilities, in perpetuity.

Please sign the following statement:

I hereby grant permission to the Graduate Division of the University of California, San Francisco to release copies of my thesis, dissertation, or manuscript to the Campus Library to provide access and preservation, in whole or in part, in perpetuity.

_____   12/12/18
Author Signature   Date